

A 5902 II

Dr. 6

POLISH ACADEMY OF SCIENCES – WROCLAW BRANCH

WROCLAW UNIVERSITY OF TECHNOLOGY

ISSN 1644-9665

INDEX 375667

Biblioteka Główna i OIINT
Politechniki Wrocławskiej



100100354457



ARCHIVES OF CIVIL AND MECHANICAL ENGINEERING

Quarterly

Vol. VI, No. 1

WROCLAW 2006

ADVISORY COMMITTEE

Chairman – JAN KMITA¹
JAN BILISZCZUK (Poland)
CZESŁAW CEMPEL (Poland)
JERZY GRONOSTAJSKI (Poland)
ANTONI GRONOWICZ (Poland)
M.S.J. HASHMI (Ireland)
HENRYK HAWRYŁAK (Poland)
RYSZARD IZBICKI (Poland)
WAĆLAW KASPRZAK (Poland)
MICHAEL KETTING (Germany)
MICHAŁ KLEIBER (Poland)
VADIM L. KOLMOGOROV (Russia)

ADOLF MACIEJNY (Poland)
ZDZISŁAW MARCINIAK (Poland)
KAZIMIERZ RYKALUK (Poland)
ANDRZEJ RYŻYŃSKI (Poland)
ZDZISŁAW SAMSONOWICZ (Poland)
WOJCIECH SZCZEPIŃSKI (Poland)
PAWEŁ ŚNIADY (Poland)
RYSZARD TADEUSIEWICZ (Poland)
TARRAS WANHEIM (Denmark)
WŁADYSŁAW WŁOSIŃSKI (Poland)
JERZY ZIÓŁKO (Poland)
JÓZEF ZASADZIŃSKI (Poland)

EDITORIAL BOARD

Editor-in-chief – JERZY GRONOSTAJSKI²
ROBERT ARRIEUX (France)
AUGUSTO BARATA DA ROCHA (Portugal)
GHEORGHE BRABIE (Romania)
LEŚLAW BRUNARSKI (Poland)
EDWARD CHLEBUS (Poland)
L. DEMKOWICZ (USA)
KAZIMIERZ FLAGA (Poland)
YOSHINOBI FUJITANI (Japan)
FRANCISZEK GROSMAN (Poland)
MIECZYŚLAW KAMIŃSKI (Poland)
Scientific secretary – SYLWESTER KOBIELAK

ANDRZEJ KOCAŃDA (Poland)
WAĆLAW KOLLEK (Poland)
PIOTR KONDERLA (Poland)
ZBIGNIEW KOWAL (Poland)
TED KRAUTHAMMER (USA)
ERNEST KUBICA (Poland)
CEZARY MADRYAS (Poland)
TADEUSZ MIKULCZYŃSKI (Poland)
HARTMUT PASTERNAK (Germany)
MACIEJ PIETRZYK (Poland)
EUGENIUSZ RUSIŃSKI (Poland)
HANNA SUCHNICKA (Poland)

¹ The Faculty of Civil Engineering, Wrocław University of Technology
Wybrzeże Wyspiańskiego 27, 50-370 Wrocław, Poland
Tel. +48 71 320 41 35, Fax. +48 71 320 41 05, E-mail: jan.kmita@pwr.wroc.pl

² The Faculty of Mechanical Engineering, Wrocław University of Technology
ul. Łukasiewicza 5, 50-371 Wrocław, Poland
Tel. +48 71 320 21 73, Fax. +48 71 320 34 22, E-mail: jerzy.gronostajski@itma.pwr.wroc.pl

POLISH ACADEMY OF SCIENCES – WROCLAW BRANCH
WROCLAW UNIVERSITY OF TECHNOLOGY

DAR



ARCHIVES OF CIVIL AND MECHANICAL ENGINEERING

Quarterly
Vol. VI, No. 1

WROCLAW 2006

EDITOR IN CHIEF

JERZY GRONOSTAJSKI

EDITORIAL LAYOUT AND PROOF-READING

EWA SOBESTO, SEBASTIAN ŁAWRUSEWICZ

SECRETARY

TERESA RYGLOWSKA

Publisher: Committee of Civil and Mechanical Engineering
of Polish Academy of Sciences – Wrocław Branch,
Faculty of Civil Engineering and Faculty of Mechanical Engineering
of Wrocław University of Technology

© Copyright by Oficyna Wydawnicza Politechniki Wrocławskiej, Wrocław 2006

OFICyna WYDAWNICZA POLITECHNIKI WROCLAWSKIEJ
Wybrzeże Wyspiańskiego 27, 50-370 Wrocław

ISSN 1644-9665

Drukarnia Oficyny Wydawniczej Politechniki Wrocławskiej. Zam. nr 517/2006.

Contents

Y. LEDOUX, S. SAMPER, H. FAVRELIÈRE, F. FORMOSA, E. PAIREL, R. ARRIEUX, Optimisation of a stamping process by a design of experiment linked to a modal analysis of geometric defects	5
J. MARCINOWSKI, Optimal orientation of reinforcing fibers in a shell made of fibrous composites	19
Z. GRONOSTAJSKI, P. BANDOŁA, P. KARBOWSKI, The effect of crashworthiness parameters on the behaviour of car-body elements	31
M. SZATA, Description of crack propagation – theoretical approach and fitting accuracy to measurement results	47
Cz.MACHELSKI, R. TOCZKIEWICZ, Effects of connection flexibility in steel-concrete composite beams due to live loads	65
P. SUTOWSKI, S. PLICHTA, An investigation of the grinding wheel wear with the use of root-mean-square value of acoustic emission	87

Spis treści

Y. LEDOUX, S. SAMPER, H. FAVRELIÈRE, F. FORMOSA, E. PAIREL, R. ARRIEUX, Optymalizacja procesu tłoczenia metodą planowania eksperymentu i analizy modalnej	5
J. MARCINOWSKI, Optymalna orientacja włókien w powłoce wykonanej z kompozytów włóknistych	19
Z. GRONOSTAJSKI, P. BANDOŁA, P. KARBOWSKI, Wpływ parametrów uderzeniowych elementów karoserii samochodów na ich zachowanie się podczas kolizji	31
M. SZATA, Opis propagacji szczeliny zmęczeniowej – podejście teoretyczne i dokładność dopasowania do wyników pomiarów	47
Cz.MACHELSKI, R. TOCZKIEWICZ, Efekty podatności zespolenia w belkach stalowych z płytą betonową pod obciążeniem zmiennym.....	65
P. SUTOWSKI, S. PLICHTA, Badanie zużycia ściernicy z wykorzystaniem wartości skutecznej sygnału emisji akustycznej	87

Optimisation of a stamping process by a design of experiment linked to a modal analysis of geometric defects

Y. LEDOUX, S. SAMPER, H. FAVRELIÈRE, F. FORMOSA, E. PAIREL, R. ARRIEUX
Laboratory of Applied Mechanics, University of Savoie, BP 806, 74016 ANNECY Cedex, France

The aim of this work was to present a method that gives an optimized set of values for the process parameters in order to obtain stamped parts with the fewest defects. The springback, influenced by process parameters, is one of the sources of defects. The process is simulated by the finite element method. A design of experiments is used to compute the mathematical model and to minimize the trials number. The defects are characterized by a set of modal shapes. A defect criterion is calculated from this decomposition. Then an optimisation is made by minimizing of this criterion in order to obtain the best process parameters. An example is shown in order to explain the method.

Keywords: *design of experiments, modal shapes, stamping, springback*

1. Introduction

In sheet metal forming, the springback is often the most serious defect observed. This problem encourages engineers to make several prototypes by using a “trial and errors” method. Several tool parameters influence the springback defect. Three different types of process parameters are identified, i.e., the tool dimensions, the process conditions (lubricant, stamping speed, etc.) and the blank initial geometry.

The aim was to build a mathematical model representing the process in order to make an optimisation that will give the values of the process parameters to obtain the part required.

A Design of Experiment (DOE) [1–2] is made in order to obtain the mathematical model and to minimise the number of experiments. This model links the geometrical defects of the part to the process parameters. In a previous work [3], this method has been presented and applied to the other (2D) example without taking into account form defects. A series of experiments is carried out using the finite element method.

The part suffers from geometrical defects which must be characterized and then minimized. These are size defects, position defects and form defects. We propose a new method in which all these defects are intrinsically included and defined in this modal basis. The part defects are projected in this modal basis and allow the calculation of each mode contribution.

By using a mathematical model of the DOE, the process parameters are optimised to obtain the values of the three kinds of process parameters that minimize the geometrical defects of the stamped part. A 3D example is presented in order to show different steps of the method.

2. The part studied and nominal tools

The part studied is obtained from a rectangular strip of 10 millimetre width, strained with cylindrical punch of a spherical head, circular die and blankholder. Figure 1 shows the drawing of the part and its dimensions. This 3D shape is chosen because of its important springback.

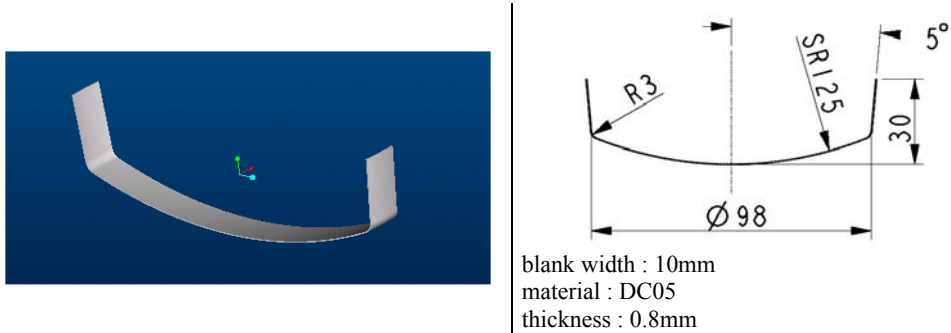


Fig. 1. Part geometry

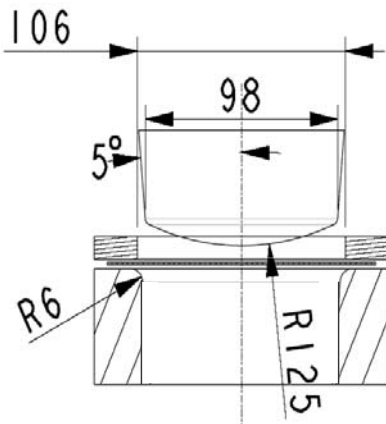


Fig. 2. Tooling for an initial simulation

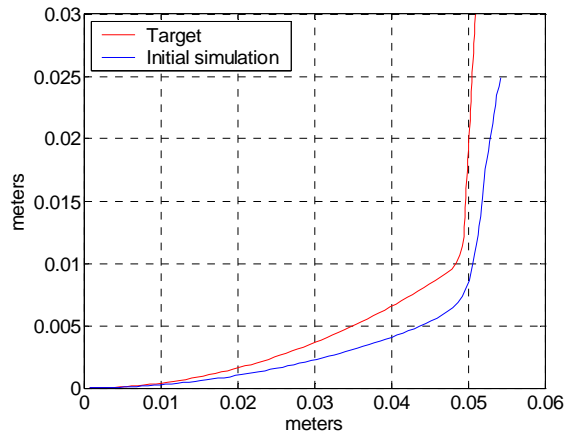


Fig. 3. Comparison between the target profile and the nominal simulated part shape

A first simulation is run with the nominal tooling (Figure 2) close to the expected part shape, in order to check the elastic deflections. The finite element calculation software ABAQUS is used in Explicit version [4]. The material is an DC05 steel sheet, 0.8 mm thick. The behaviour law is determined in tensile tests by using an extensometer and an image analysis system for the high-strain levels [5]. It is introduced point by point into the FEM software. An elastoplastic anisotropic behaviour is as-

sumed according to Hill's 48 criterion with strain-rate dependence [6]. Shell elements with four nodes are used for modelling (called S4R in Abaqus). The contact between the tools and the blank is of the Coulomb type with a friction coefficient $f = 0.15$ determined experimentally. The blankholder force is 3000 N.

Figure 3 allows us to appreciate importance of the effects of elastic deflections on the virtual part shape after tool removing.

The objective is now to reduce the differences between the simulated and the target parts. To that end, we propose to use the DOE method which allows us to study the influence of the forming process conditions on the part geometry. In such a way, it is possible to calculate polynomial equations and then to find an optimal configuration of the tool.

3. The method proposed

In Figure 4, the process is schematized. The inputs are the Process Parameters (PP) and the output, the Part Geometric Parameters (PGP). The DOE makes a series of trials in the PP space in order to model the process (here the stamping process is a FEM simulation). The model is a polynomial equation (linear, then quadratic) linking PP to PGP. As the process has deviations, an optimisation of the PP is carried out in order to obtain an ideal PGP.



Fig. 4. Process parameters to be optimized

3.1. Geometrical parameters of the part

3.1.1. Feature parametrization

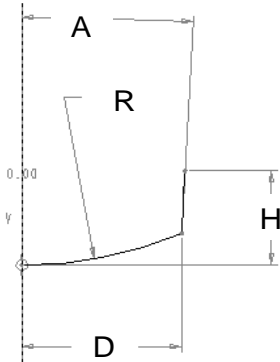
In order to allow the characterization of the geometry and to quantify and qualify the stamped part defects, it is necessary to define a geometrical parameter setting. There are several ways to define the parameterization of a surface. A traditional parameter setting consists in dimensioning the part of particular dimensions. In a CAD software, this way enables us to define a set of parameters associated with the features building as shown in Figure 5. It is possible to define the other set of feature parameters by combination of the previous one (Figure 6).

Assumptions:

The part and its defects are symmetrical.

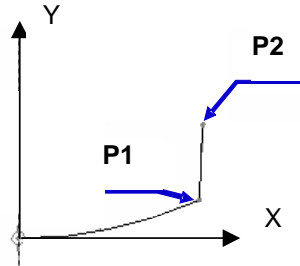
There is **no form defect**.

For the geometry studied, four feature parameters are sufficient. We can propose two possibilities shown in Figures 5 and 6.



$PS_1(A,D,H,R)$ a building CAD parameters

Fig. 5. The first possible set of feature parameter setting



$PS_2(XP_1,YP_1,XP_2,YP_2)$ set of parameters

Fig. 6. The second possible set of feature parameter setting

This part has been analyzed with the PS_2 parametrization in [1]. This method gives good results, but it does not take into account form defects of each feature of the part.

3.1.2. Discrete geometry parametrization

Discrete geometry parametrization allows us to fit the measured geometry with an open basis of derivative geometries. Thus size, position and form defects can be decomposed in the following basis. Several discrete parameterizations are possible. The first one is the Fourier-type transformation [8–9] which is well known by metrologist dealing with the circularity and straightness defects (2D defects for one-parameter geometry). In the case of optic lenses (ISO 10110-5), Zernike polynomials define a set of possible defects for a disk geometry (3D defects for two-parameter geometry). The Discrete Cosinus Transformation [10] that makes it possible to define a set of defects for a rectangular geometry (3D defects for two-parameter geometry) is used for image processing.

Those solutions are interesting because they allow the description of all the defects according to the parameterization. Otherwise the geometry studied is simple (segment, circle, disk, rectangle). We propose a model [11–12] which can be used for each geometry. This model is based on modal analysis of the target part geometry.

Assumptions:

The part and its defects are symmetrical.

Form defects are taken into account.

The eigendecomposition modes. As we expect, to characterize the part profile, 2D beam elements are chosen for this eigendecomposition mode. The clearance between the target profile and the simulated profile is calculated in a deviation vector (V). The modal analysis is used for computing the modal basis Q_i .

Then, this basis is used for the decomposition of V and to calculate coordinates λ_i . These coordinates represent the deviations projected in the modal basis.

General purpose. In linear dynamics, the discretized equations of movement in the conservative, discrete or continuous systems can be written in the following general form:

$$M\ddot{q} + Kq = 0. \quad (1)$$

In Equation (1), M is the generalized mass matrix; K , the generalized stiffness matrix; q , a dynamic displacement vector.

n is the number of degrees of freedom of the system. The solutions are the modes q_i of a structure which can be decomposed as two functions (space and time):

$$q_i = Q_i \cos(\omega_i t), \quad (2)$$

where Q_i is the vector of amplitudes, and ω_i is the corresponding pulsations in rad.s^{-1} . Taking into account their definition, the modes are solutions of the equation:

$$(K - \omega_i^2 M) Q_i = 0. \quad (3)$$

Equation (3) admits n eigensolutions, which are the structure modes. The modal pulsations ω_i of the various modes are the roots of the characteristic polynomial:

$$\det(K - \omega_i^2 M) = 0. \quad (4)$$

The vectors of modal deformations Q_i are the eigenvectors associated with the pulsations ω_i , which form a basis M and K orthogonal in the vector space of the structure movements. The scalar product is given by:

$$\langle A.B \rangle = A^t.M.B. \quad (5)$$

The norm is then

$$\|A\| = \sqrt{A^t.M.A}. \quad (6)$$

The orthogonality of the eigenmodes means that the inertia and stiffness developed in a mode do not work in the movements of the other modes. There is mechanical independence of the modes.

This method gives all the possible defects of the part (mode shapes) through modal shape decomposition. In fact, the discretization limits the number of possible defects.

Application of the method to the part studied. The stamped part geometry results from numerical simulation. It is discretized with 90 elements of equal length. The clearance vector V is calculated based on the deviation of the target geometry from the simulated stamped one. The *eigenmodes* of the geometry are identified by means of modal analysis (see relation (3)).

A projection of the vector V in this base is done that allows the coordinates λ_i to be calculated.

Its decomposition is carried out using the vectorial projection defined in (5):

$$\lambda_i = \langle V, Q_i \rangle = V^t \cdot M \cdot Q_i, \quad (7)$$

where λ_i is the coordinate associated with the mode Q_i , the so-called modal coordinates. Figure 7 represents three first mode shapes that can be compared to the target geometry.

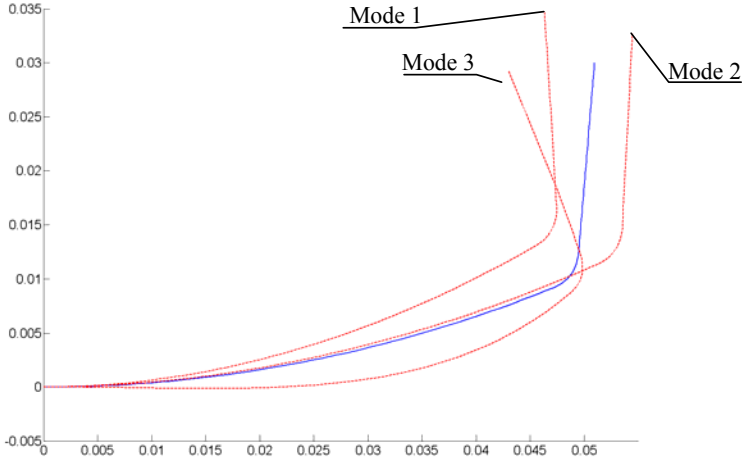


Fig. 7. The shapes of the modes 1, 2 and 3

Definition of defect criterion. The model is composed of 270 degrees of freedom (90 nodes and 3 degrees of freedom) and as many *eigenmodes*. Thus the part defect can be explained in this base by 270 scalars. The objective is to reduce the dimension of the problem by defining a particular criterion. If the geometry resulting from the digital simulation is the same as the target geometry, the vector V (component of the projection distances) is equal to zero. The corresponding modal coordinates are equal to zero. Then, the following criterion is defined:

$$C = \sum_{i=1}^{n \text{ eigenmode}} (\lambda_i)^2. \quad (8)$$

Figure 8 shows the modal decomposition of the nominal geometry. It can be obvious that the first modes are the most contributing to the modal description of the defect parts.

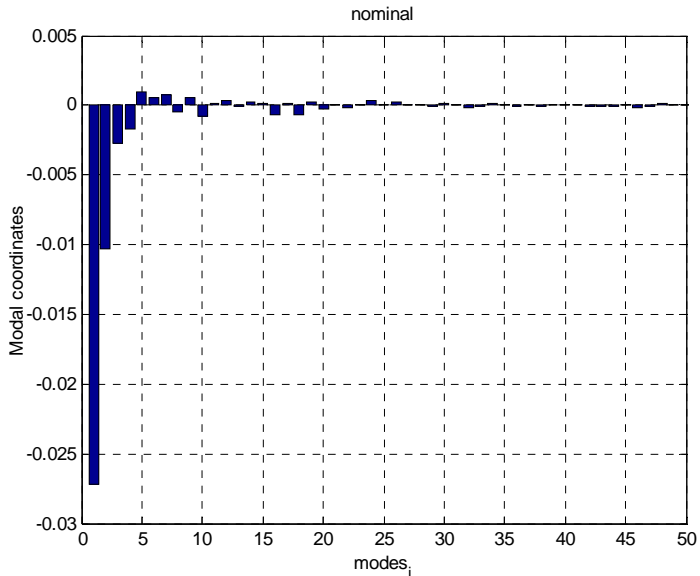


Fig. 8. Nominal modal coordinates

3.2. Process parameters

In our experience, the selected PP usually affect the selected PGP. Moreover, they must be strictly independent. This means that the variation in one of them must occur without modification of the other ones.

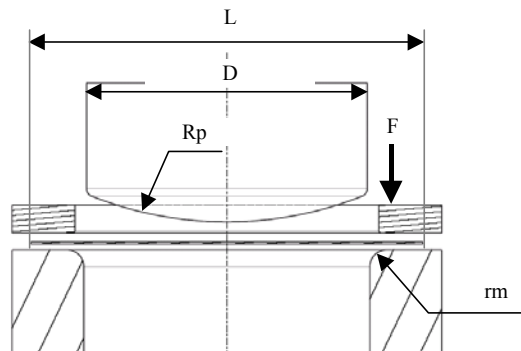


Fig. 9. Selected process parameters

The selected process parameters are as follows:

- R_p : sphere radius,
- rm : die radius,
- D : punch diameter,
- F : blankholder force,
- L : initial blank length.

Their variation ranges are chosen depending on the initial simulation and observations of their supposed influence. These values are given in Table 1.

Table 1. Parameters investigated and associated variation range

Parameters	level - 1.719	level - 1	Mean	level + 1.719	level + 1.719
R_p : sphere radius (mm)	69.2	80	95	110	120.8
rm : die radius (mm)	2.2	4	6.5	9	10.8
D : punch diameter (mm)	95.3	96	97	98	98.7
F : blank holder force (N)	1281	2000	3000	4000	4719
L : initial blank length (mm)	134.2	136	138.5	141	142.8

3.3. Model and DOE

In this paper, we use a fractional factorial design because it allows a sequential study of the process. Indeed, based on these previous experiments, a linear mathematical model will be calculated. Then, in a second time, it will be completed with a composite design that allows the quadratic modelling of the process.

3.3.1. Linear and quadratic models

Here, the first-degree polynomial model is selected, it assumes a linear variation in the output from every input:

$$Y = a_0 + a_1X_1 + a_2X_2 + \dots + a_nX_n + a_{12}X_1X_2 + \dots + a_{ij}X_iX_j.$$

In this model, the terms X_iX_j are the interactions between factors, which means that the effect X_i of one of them depends on the value X_j of the other one.

A fractional factorial experiment design is used in order to decrease the number of numerical simulations. For five factors it is necessary to carry out 16 numerical experiments, as shown in Table 2, whereas for a full factorial experiment design, 32 experiments are necessary. Thus, we tested 2 levels of variable, the maximum and the minimum ones defined in Table 1. In Table 1, the levels -1 and +1 correspond respectively to the minimum value and the maximum value of each parameter.

This first design is completed with a composite design which allows the calculation of a quadratic model:

$$Y = a_0 + a_1X_1 + a_2X_2 + \dots + a_nX_n + a_{12}X_1X_2 + \dots + a_{ij}X_iX_j + a_{ii}X_i^2.$$

Then the parameters vary from -1.719 to +1.719 with 5 levels for each (-1.719, -1, 0, 1, +1.719) [2].

3.3.2. Experimental design

Each experiment corresponds to a numerical simulation carried out with the corresponding process parameters. As a result we obtain a file of points which are the nodes of the simulated mesh of the formed part, after the tools removing. This file is post-treated in order to evaluate the geometric modal parameters and then to calculate the value of the criterion C . The results are shown in Table 2.

Table 2. Experimental trials and modal geometrical results

	No.	Rp	rm	D	F	L	Results	C
Linear experiments	1	-1	-1	-1	-1	-1	profil 1	1.229E-04
	2	-1	-1	-1	1	1	profil 2	3.223E-04
	3	-1	-1	1	-1	1	profil 3	2.334E-04
	4	-1	-1	1	1	-1	profil 4	1.486E-04
	5	-1	1	-1	-1	1	profil 5	1.187E-04
	6	-1	1	-1	1	-1	profil 6	1.022E-04
	7	-1	1	1	-1	-1	profil 7	2.069E-04
	8	-1	1	1	1	1	profil 8	1.501E-04
	9	1	-1	-1	-1	1	profil 9	4.297E-05
	10	1	-1	-1	1	-1	profil 10	1.767E-04
	11	1	-1	1	-1	-1	profil 11	4.089E-04
	12	1	-1	1	1	1	profil 12	6.475E-05
	13	1	1	-1	-1	-1	profil 13	4.569E-04
	14	1	1	-1	1	1	profil 14	1.051E-04
	15	1	1	1	-1	1	profil 15	2.330E-04
	16	1	1	1	1	-1	profil 16	7.036E-04
Center points	17	0	0	0	0	0	profil 17	6.410E-05
	17'	0	0	0	0	0	profil 17	6.410E-05
	17''	0	0	0	0	0	profil 17	6.410E-05
	17'''	0	0	0	0	0	profil 17	6.410E-05
Quadratic experiments	18	-1.719	0	0	0	0	profil 18	3.892E-04
	19	1.719	0	0	0	0	profil 19	3.662E-04
	20	0	-1.719	0	0	0	profil 20	3.187E-05
	21	0	1.719	0	0	0	profil 21	1.272E-04
	22	0	0	-1.719	0	0	profil 22	1.391E-05
	23	0	0	1.719	0	0	profil 23	1.704E-04
	24	0	0	0	-1.719	0	profil 24	7.785E-05
	25	0	0	0	1.719	0	profil 25	4.060E-05
	26	0	0	0	0	-1.719	profil 26	3.811E-04
	27	0	0	0	0	1.719	profil 27	6.410E-05

3.4. Calculation of the coefficients of polynomial models

From the results of the DOE, the coefficients of the polynomial model for the modal criterion are calculated. The following equations are obtained:

From the linear DOE model (C_{lin}):

$$\begin{aligned}
 C_{lin} = & 2.2 \cdot 10^{-4} + 4.9 \cdot 10^{-5} \cdot Rp' + 3.5 \cdot 10^{-5} \cdot rm' + 4.4 \cdot 10^{-5} \cdot D' - 3.2 \cdot 10^{-6} \cdot F' - 6.6 \cdot 10^{-5} \cdot L' \\
 & + 6.6 \cdot 10^{-5} \cdot Rp' \cdot rm' + 3.5 \cdot 10^{-5} \cdot Rp' \cdot D' - 8.3 \cdot 10^{-6} \cdot Rp' \cdot F' - 9.6 \cdot 10^{-5} \cdot Rp' \cdot L' \\
 & + 2 \cdot 10^{-5} \cdot rm' \cdot D' + 8.8 \cdot 10^{-6} \cdot rm' \cdot F' - 4.2 \cdot 10^{-5} \cdot rm' \cdot L' \\
 & + 1.2 \cdot 10^{-6} \cdot D' \cdot F' - 3.2 \cdot 10^{-5} \cdot D' \cdot L' \\
 & + 4.9 \cdot 10^{-6} \cdot F' \cdot L'
 \end{aligned} \quad (9)$$

From the quadratic DOE model (C_{quad}):

$$\begin{aligned}
 C_{quad} = & 6.8 \cdot 10^{-5} + 3.4 \cdot 10^{-5} \cdot Rp' + 3.3 \cdot 10^{-5} \cdot rm' + 4.4 \cdot 10^{-5} \cdot D' - 5.2 \cdot 10^{-6} \cdot F' - 7.3 \cdot 10^{-5} \cdot L' \\
 & + 1.0 \cdot 10^{-4} \cdot Rp'^2 + 6.6 \cdot 10^{-5} \cdot Rp' \cdot rm' + 3.5 \cdot 10^{-5} \cdot Rp' \cdot D' - 8.3 \cdot 10^{-6} \cdot Rp' \cdot F' - 9.6 \cdot 10^{-5} \cdot Rp' \cdot L' \\
 & + 2.2 \cdot 10^{-6} \cdot rm'^2 + 2 \cdot 10^{-5} \cdot rm' \cdot D' + 8.8 \cdot 10^{-6} \cdot rm' \cdot F' - 4.2 \cdot 10^{-5} \cdot rm' \cdot L' \\
 & + 6.5 \cdot 10^{-6} \cdot D'^2 + 1.2 \cdot 10^{-6} \cdot D' \cdot F' - 3.2 \cdot 10^{-5} \cdot D' \cdot L' \\
 & - 4.6 \cdot 10^{-6} \cdot F'^2 + 4.9 \cdot 10^{-6} \cdot F' \cdot L' \\
 & + 5.1 \cdot 10^{-5} \cdot L'^2
 \end{aligned} \quad (10)$$

In Equations (9) and (11), Rp' , rm' , D' , F' , and L' are the standardized variables corresponding to Rp , rm , D , F , and L , respectively. They vary from -1 to $+1$ when the corresponding variables vary from the minimum value to the maximum one. Equations (9) and (10) represent the surfaces in six dimensions which describe the process behaviour in the range variations of the PP. Those results are validated by analysing the deviation near the centre of the solution domain, because in this area the deviation is supposed to be the biggest.

4. Optimization of the process parameters

The previous mathematical relations are used to determine the values of the process parameters which allow us to obtain the best values for the geometrical part parameters.

The goal is to find the process parameters which minimize the criterion C for the linear and the quadratic models.

$$\text{minimized } C = \text{minimized} \left(\sum_{i=1}^n \text{eigenmode} (\lambda_i)^2 \right). \quad (11)$$

Optimum values of the process parameters are obtained and a numerical simulation by finite element method is carried out.

Table 3. Comparison of result

Linear optimum				
Tool parameters				
Rp'	rm'	D'	F'	L'
1	-1	-1	1	1
110	4	96	4000	141

Criterion	
Target	0
DOE model	9.77E-06
Simulation	1.71E-04
Nominal	8.60E-04

Quadratic optimum				
Tool parameters				
Rp'	rm'	D'	F'	L'
0.47	-0.75	-0.99	0.44	0.61
102.1	4.6	96	3441	140

Criterion	
Target	0
DOE model	2.37E-13
Simulation	4.96E-05
Nominal	8.60E-04

In Table 3, the two optimum simulated profiles are compared to the nominal profile (initial simulation). It can be observed that both linear and quadratic optima improve considerably the initial geometry tested as shown in Figure 10.

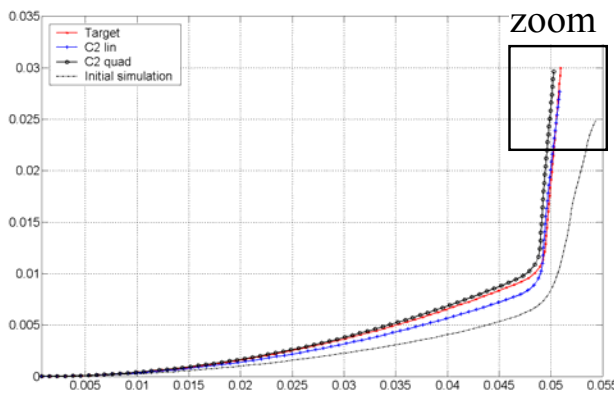


Fig. 10. Comparison of simulated optima, nominal and target profiles

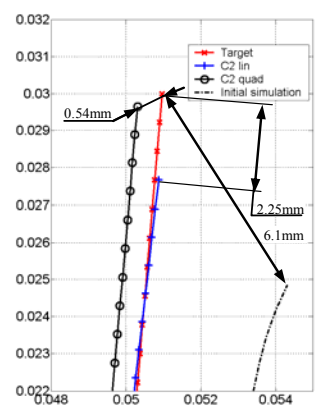


Fig. 11. Zoom of Figure 10

The linear optimum is close to the target geometry compared to the initial one. The linear optimum needs only 16 experiments (with 5 parameters). The accuracy is improved by using a quadratic model which needs to compute 27 trials (11 simulations more than for linear one).

The linear optimum is shown in the modal shape basis in Figure 12 as a set of modal coordinates. We can see that a small number of modal shapes is needed to represent the optimum.

Figure 13 shows the modal coordinates of quadratic optimum. The set of significant coordinates is larger because the solution is closer to the target, and greater mode contributions are needed.

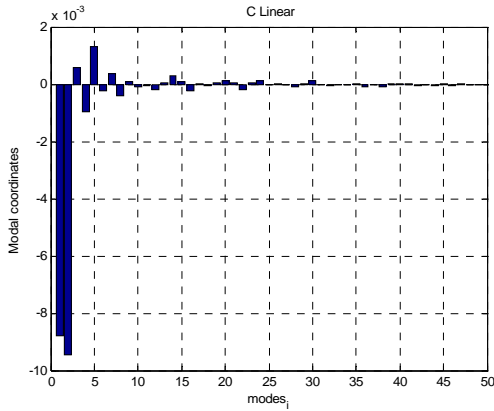


Fig. 12. Modal coordinates of the linear optimum solution

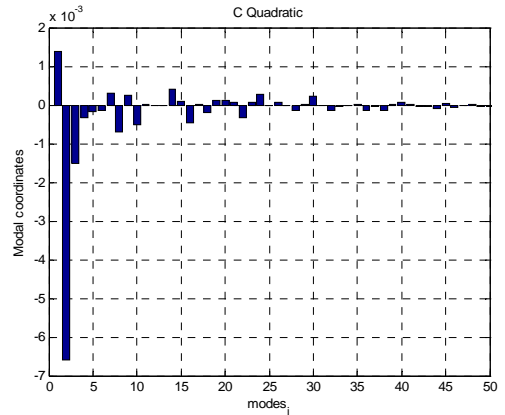


Fig. 4. Modal coordinates of the quadratic optimum solution

5. Conclusion

The problem of the springback is a classic source of deviations in making stamped parts. Most often, engineers use a “trials an errors” method to compensate it. This can give results, but with lots of trials and tools modifications with no guarantee of success.

In order to assist the engineers, we have developed an optimization method of stamping process parameters by combining DOE with modal characterization of defects.

First, a trial is carried out with nominal process parameters (the part would be ideal without springback). The maximum difference between the target part and the nominal part is more than 5 mm. The defects are measured and then characterized in the basis of defects built on modal shapes. The engineer defines the range of variation of each process parameter which could compensate for the defect. With a fractional factorial DOE the minimum series (16 experiments) of trials is defined, therefore the linear mathematical model of the process is calculated. With a composite DOE the quadratic model (11 experiments more) is built. Each model (linear, then quadratic) is used to find two different optima of process parameters by minimizing the geometric criterion based on modal decomposition of deviations. The shape defects are well identified by using the modal decomposition. This method allows us to compute automatically the set of possible defects (of size and shape). The optima found are tested in the process, and the comparison of these parts to the target gives their very good accuracy. As the linear model is first built, the corresponding optimum is first given (maximum deviation approaches 3 mm). The maximum nominal deviation is divided by two with only sixteen trials. Then the quadratic model is calculated with more than eleven trials and the maximum nominal deviation is divided by seven (0.7 mm).

The study of more complex part with several stamping steps is under investigation.

References

- [1] Pillet M.: *Les plans d'expériences par la méthode Taguchi*, Ed les éditions d'organisation, 1997.
- [2] Montgomery D. C.: *Design and analysis of experiments*, fourth edition, 1996.
- [3] Pairel E., Ledoux Y., Arrieux R., Tabourot L., Incandela O.: *Geometrical defects correction of stamping parts by numerical simulation and design of experiment*, Archives of Civil and Mechanical Engineering, 2004, Vol. 4, No. 4, pp. 75–85.
- [4] Hibbit, Karlson, Sorensen: *ABAQUS/Explicit User's Manual version 6.4*, 2003.
- [5] Dumoulin S., Tabourot L., Chappuis C., Vacher P., Arrieux R.: *Determination of the equivalent stress–equivalent strain relation of a sample of copper in tensile loading*, International Journal of Material Processing Technology, 2003, No. 133, pp. 79–83.
- [6] Hill R.: *A theory of the yielding and plastic flow of anisotropic metals*, Proc. R. Soc. Lond. 1948, A193, pp. 281–297.
- [7] Arrieux R., Ledoux Y., Pairel E.: *A method of springback compensation and process parameters optimisation based on finite element method and design experiment*, Proceedings of net-shape sheet metal forming, May 13th, 2005, Poznań (PL), pp. 69–83.
- [8] Capello E., Semeraro: *Harmonic fitting approach for plane geometry measurements*, The International Journal of Advanced Manufacturing Technology, 2000, Vol. 16, pp. 250–258.
- [9] Summerhays: *Optimizing discrete point sample patterns and measurement data analysis on internal cylindrical surfaces with systematic form deviations*, Precision Engineering Journal of the International Societies for Precision Engineering and Nanotechnology, 2002, No. 26, pp. 105–121.
- [10] Huang W., Ceglarec D.: *Mode-based decomposition of part form error by discrete-cosine-transform with implementation to assembly and stamping system with compliant parts*, Annals of the CIRP, 2002, Vol. 51(1), pp. 21–26.
- [11] Formosa F., Samper S.: *Modal expression of form defects*, Proceedings of 2005 CIRP International Seminar on Computer Aided Tolerancing Tempe, Arizona, 2005.
- [12] Adragna P.-A., Samper S., Pillet M., Favreliere H.: *Analysis of shape deviations of measured geometries with modal basis*, XVII Workshop on Supervising and Diagnostics of Machining Systems Manufacturing Accuracy Increasing Problems, Karpacz, Poland, March 2006.

Optymalizacja procesu tłoczenia metodą planowania eksperymentu i analizy modalnej

Celem pracy jest optymalizacja procesu kształtowania wytłoczek ze względu na możliwość eliminacji skutków sprężystych odkształceń powrotnych. Zastosowanie planowania eksperymentu (MES) jako eksperymentu wirtualnego oraz analizy modalnej w celu oceny kształtu wytłoczki umożliwiają wyznaczenie parametrów tłoczenia zapewniających dużą dokładność kształtu wytłoczki.

Optimal orientation of reinforcing fibers in a shell made of fibrous composites

JAKUB MARCINOWSKI

University of Zielona Góra, Institute of Structural Engineering, Faculty of Civil and Environmental Engineering, Z. Szafrana 2, 65-516 Zielona Góra

Maximization of stability resistance of composite shells with respect to fibers orientation is described. Shells are made of fibrous composite and optimum orientation of fibers reinforcing the composite is searched for. The author's computer program is utilized in the analysis. The intensity of one parametric loading corresponding to primary critical point is obtained as a result of fully geometrically nonlinear analysis. Only elastic effects are taken into account, but as far as displacements are concerned they can be arbitrary. As an example the segment of a cylindrical shell loaded laterally to its surface is considered.

Keywords: *fibrous composites, optimization, stability, finite element method*

1. Introduction

Fibrous composites are very extensively utilized in engineering practice. Aerospace, airplane and ship structures, automobile industry, civil, mechanical and biomechanical engineering are just few examples of the domains in which composites are utilized as the whole structural elements or very important structural members.

The typical fibrous composite is a two-phases material. Its main component is the matrix made of epoxy resin, polymer, aluminum alloy or mangan alloy [1]. The second component responsible for the strength of the whole composite is reinforcement in the form of short or long fibers. The diameter of a single fiber is usually smaller than 0.1 mm (thinner than human's hair) and the volume proportion of this phase reaches even 80% of the composite volume. Glass fibers (whiskers), graphite fibers, Cevlar fibers and others are used as reinforcing fibers in fibrous composites. The main advantage of fibrous composites is their large relative strength defined as the tensile strength to the density ratio (R_m/γ expressed in $[\text{MPa}/(\text{kg}/\text{m}^3)]$) and very high relative module of elasticity defined as the Young modulus to the density ratio (E/γ expressed in $[\text{MPa}/(\text{kg}/\text{m}^3)]$). Fibrous composites made of epoxy resin and graphite fibers exhibit the relative strength equal to 1.30 and the relative module of elasticity – 90.0. In the case of aluminum alloy, these parameters are 0.21 and 26, in the case of martensitic steel, 0.25 and 30, and in the case of titanium alloys, 0.27 and 27, respectively. Thus the fibrous composites are very light and very strong materials indeed. A relatively high manufacturing cost is the most important disadvantage of fibrous composites. Due to technological progress this disadvantage will not be so substantial.

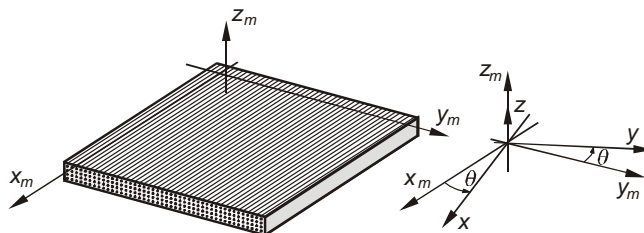


Fig. 1. The fibrous composite as a monotropic material

Fibrous composites reinforced with single-direction oriented fibers (see Figure 1) are particular case of composites considered in this paper. Such a material is anisotropic in microscale, but in macroscale it can be treated as orthotropic in the plane of reinforcing. In this plane, two mutually perpendicular directions can be distinguished: the strong one corresponding to the fibers' direction and the weak one – perpendicular to it. In the third direction, perpendicular to this plane, the material properties can be treated as isotropic. This kind of orthotropy is called *monotropy* or *transverse isotropy* ([2], [3], [4]) and occurs in thin plates and shells made of fibrous composites reinforced in the planes parallel to their middle surfaces.

Structural members made of fibrous composites are designed in two stages. In the first stage, the composite of required physical and mechanical properties is designed. As a result the most advantageous “mixture” of fibers and matrix phases is obtained. There exist many theoretical methods of modelling the composite properties on the basis of known material parameters of fibers and the matrix ([2], [3], [4]). The simplest of them are based on the rule of mixture, more advanced use methods of theory of elasticity and possibilities offered by the finite element method ([4]).

The second stage of the procedure of composite designing refers to optimal utilization of the composite material. The best choice of fibers orientation is most important in this stage. Because fibers are responsible for the strength of the composite, the problem is how to arrange fibers to obtain the strongest structural member, if this mechanical property is chosen as the main objective of optimization.

Maximization of the buckling resistance with respect to the fibers orientation was considered by Hu and Lin [7]. In that paper, more references to this subject can be found.

The present paper deals with thin shells of thin and moderate thickness made of fibrous composite material. The shape and loading manner of shells are such that the structural member is liable to lose its stability earlier than material failure could occur. For this reason the biggest critical load was chosen as the optimization criterion. It will be assumed that all material parameters of fibrous composite are known in advance. The angle determining the orientation of fibers in the whole domain of the structural member or within the selected subdomains will be the only variable parameter. The optimum value of this angle with respect to maximum value of critical loading will be determined in the process of inspection of the set of solutions obtained for the whole range of angle variation. The critical load will be calculated by means of

author's program. It is possible to perform a full geometrically nonlinear analysis of shells with particular emphasis put on elastic stability phenomenon. The orthotropic material properties were taken into account in this program. It was assumed that generally within every finite element, material directions are different from directions of local coordinate system in which stress and strain components are calculated.

2. Constitutive relations for shells made of fibrous composite

The general form of constitutive relation for linearly elastic materials can be written as follows

$$\sigma_{ij} = D_{ijkl} \varepsilon_{kl}, \quad (1)$$

where: σ_{ij} – the components of the stress tensor (the tensor of the second order), ε_{kl} – the components of the strain tensor (the tensor of the second order), D_{ijkl} – the components of the tensor of elasticity constants (the tensor of the fourth order).

It is desirable sometimes to express the components of tensors in the other rotated coordinate system. Rules of transformation adopt the following form:

$$\sigma_{i'j'} = \alpha_{i'k} \alpha_{j'l} \sigma_{kl}, \quad D_{i'j'k'l'} = \alpha_{i'm} \alpha_{j'n} \alpha_{k'o} \alpha_{l'p} D_{mnop}, \quad (2)$$

where $\alpha_{i'k}$ is the cosine of the angle between the i' -axis of the rotated coordinate system and the k -axis of the original coordinate system.

These general formulae simplify in the case of plates and shells due to the fact that the plane stress state is assumed at every surface parallel to the middle surface. One can assume that the plane x - y is locally tangent to the current surface. In this case, $\sigma_x \equiv \sigma_{11}$, $\sigma_y \equiv \sigma_{22}$, $\tau_{xy} \equiv \sigma_{12}$ are the only non-zero components of stress tensor.

In the case of Reissner–Mindlin shell theory, two additional stress components, namely $\tau_{xz} \equiv \sigma_{13}$ and $\tau_{yz} \equiv \sigma_{23}$, are taken into account. Strain components corresponding to these shear stresses are $\gamma_{xz} \equiv 2\varepsilon_{13}$, $\gamma_{yz} \equiv 2\varepsilon_{23}$, respectively. In this particular case and for orthotropic material properties (within this surface), the constitutive relation can be written as follows [7]:

$$\begin{Bmatrix} \sigma_x \\ \sigma_y \\ \tau_{xy} \\ \tau_{xz} \\ \tau_{yz} \end{Bmatrix} = \begin{bmatrix} \frac{E_x}{1-\nu_{xy}\nu_{yx}} & \frac{E_x\nu_{xy}}{1-\nu_{xy}\nu_{yx}} & 0 & 0 & 0 \\ \frac{E_y\nu_{yx}}{1-\nu_{xy}\nu_{yx}} & \frac{E_y}{1-\nu_{xy}\nu_{yx}} & 0 & 0 & 0 \\ 0 & 0 & G_{xy} & 0 & 0 \\ 0 & 0 & 0 & kG_{xz} & 0 \\ 0 & 0 & 0 & 0 & kG_{yz} \end{bmatrix} \begin{Bmatrix} \varepsilon_x \\ \varepsilon_y \\ \gamma_{xy} \\ \gamma_{xz} \\ \gamma_{yz} \end{Bmatrix}, \quad (3)$$

or in matrix notation

$$\{\sigma\} = [D]\{\varepsilon\}, \quad (4)$$

where E_x, E_y – the values of Young's modulus in the directions x and y , respectively, G_{xy}, G_{xz}, G_{yz} – the values of Kirchhoff's modulus in the planes x - y , x - z and y - z , respectively. The shear correction factor $k = 5/6$ was introduced here due to the fact that within a degenerated finite element (see below) used here, transverse strains are constant along its thickness, while actually this distribution is parabolic ([5], [6]).

The coefficient ν_{xy} expresses the ratio of a linear deformation $|\varepsilon_x|$ to the deformation ε_y when the specimen of material is loaded only in the direction y . The coefficient ν_{yx} can be interpreted analogously. Due to the symmetry property the following relations holds true

$$E_x \nu_{xy} = E_y \nu_{yx}. \quad (5)$$

This relation reduces the number of independent material parameters in the matrix $[D]$. In the case of the actual fibrous composite, all material parameters which appear in (3) are known. The direction x is identified with the orientation of fibers and the direction y is perpendicular to it.

The constitutive relation is represented by (3) only in the case where the material directions coincide with the directions x, y of local coordinate system within finite element (see Figure 1). In general case, these directions are different and in this case it is necessary to transform D_{ijkl} components into local directions x, y according to rule (2). In the case of vector-matrix convention used here (compare relation (3)), the transformation rule for the matrix $[D]$ can be written as follows

$$[D^L] = [T]^T [D][T], \quad (6)$$

where: $[D^L]$ – the matrix of elastic constants in local coordinate system, $[D]$ – the matrix of elastic constants in original material coordinate system, $[T]$ – the transformation matrix which is defined as follows [7]

$$[T] = \begin{bmatrix} c^2 & s^2 & cs & 0 & 0 \\ s^2 & c^2 & -cs & 0 & 0 \\ -2cs & 2cs & c^2 - s^2 & 0 & 0 \\ 0 & 0 & 0 & c & s \\ 0 & 0 & 0 & -s & c \end{bmatrix}, \quad (7)$$

$c = \cos \theta$, $s = \sin \theta$, θ – the angle between the material direction x_m and the local direction x (see Figure 1).

A constitutive relation (4) assumes in this case the following form

$$\{\sigma\} = [D^L] \{\varepsilon\} = [T]^T [D] [T] \{\varepsilon\}, \quad (8)$$

where $\{\sigma\}$ and $\{\varepsilon\}$ are expressed in the local coordinate system.

3. Finite element for fibrous composite shells exhibiting big displacements

The finite element used here was obtained based on original Ahmad's element [5]. Description of big displacements and generally geometrical nonlinearities of the very element were proposed by Marcinowski [6].

The finite element used here is a degenerated element of solid type. The degeneration of 3D case into the 2D one is the result of some accepted hypotheses on the distribution of displacements across the shell thickness. It can be shown that the displacement hypotheses accepted [6] lead to the shell conception being equivalent to the Reissner–Mindlin shell theory. Displacements of any point within the finite element are defined by five nodal parameters: three translations u , v , w in global coordinate system and two independent rotations α , β in two mutually perpendicular, properly chosen directions (compare [6] and see Figure 2). The stress state at any point within the element is described by five components σ_x , σ_y , τ_{xy} , τ_{xz} , τ_{yz} expressed in local coordinate system and chosen in such a way that the plane x , y is tangent to the middle surface of the shell. In general case, the stress components change across the shell thickness.

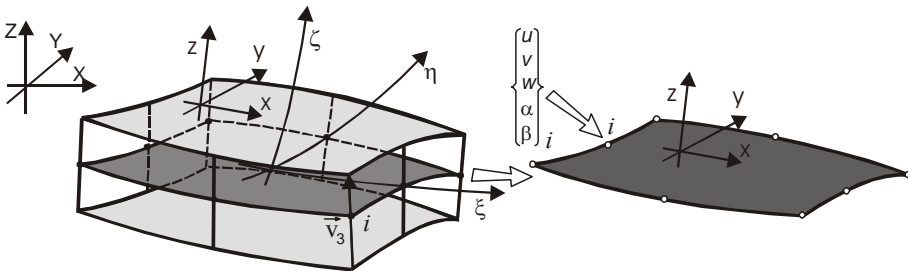


Fig. 2. The finite element

The following strain counterparts: ε_x , ε_y , γ_{xy} , γ_{xz} , γ_{yz} correspond to the stress components specified above. A constitutive relation is adopted as for orthotropic material for the directions x , y , z , the z -axis being always perpendicular to the middle surface. This assumption allows neglecting the component σ_z normal to the middle surface [6].

The constitutive relation is adopted as (8) with the transformation matrix $[T(\theta)]$ (Equation (7)) and matrix $[D]$ defined in material directions according to Equation (3).

As far as numerical procedures are concerned, they were kept in original form used before for the analysis of elastic, isotropic shells [6]. These procedures allow the nonlinear equilibrium paths to be determined within a whole range of load-deflection domain. And particularly, all singularities related to the stability phenomenon can be taken into account. Limit points, primary and secondary bifurcation points can be determined during the calculation process. The state of stability in any considered configuration can be established as well.

4. Numerical example

The segment of cylindrical shell shown in Figure 3 was chosen as an example. Geometrical parameters and orientations of fibers with respect to local coordinate system of all finite elements were shown in this figure as well. The shell is supported only in the corners (see Figure 3) and in these nodes all displacement parameters are equal to zero. One-parameter loading in the form of uniformly distributed pressure defined by the intensity p is considered. For this structural member the optimum orientation of fibers reinforcing the composite, from which the shell is made of, is searched for. The maximum value of the critical pressure was chosen as the objective function. It was assumed that the shell can be fabricated also from four segments and within these segments the orientation of fibers is constant. Both variants of reinforcing of the shell considered are shown in Figure 3 and labelled as the first and the second kinds, respectively.

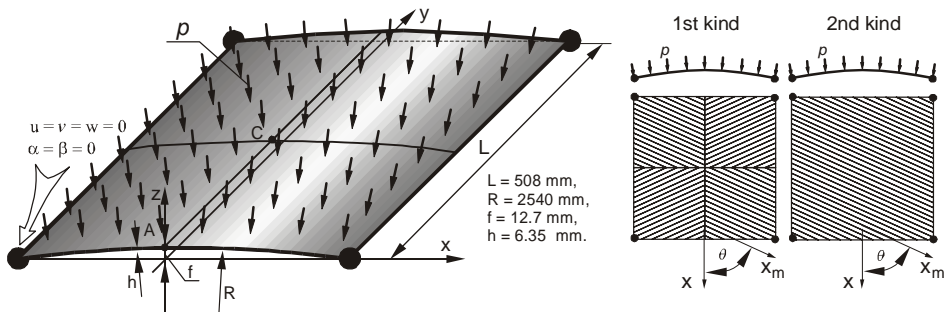


Fig. 3. The segment of cylindrical shell

The angle θ is the only variable parameter in the optimization process. Because of this the optimisation procedure is trivial. It is sufficient to calculate p_{cr} for all admissible θ 's and to choose the particular one, i.e., that corresponding to the p_{cr}^{\max} .

The reinforced composite with epoxy matrix and graphite fibers was chosen and carefully considered. Material parameters in material directions (x – the orientation of fibers, y – the direction perpendicular to it) are as follows: $E_x = 129.1$ GPa, $E_y = 9.43$ GPa, $G_{xy} = 5.39$ GPa, $G_{xz} = 3.15$ GPa, $G_{yz} = 3.15$ GPa, $\nu_{xy} = 0.021$,

$\nu_{yx} = 0.288$. The matrix $[D]$ is defined according to relations (8), (7) and (3). θ is the angle between the fibers of a given orientation and the x -axis of local coordinate system of all finite elements.

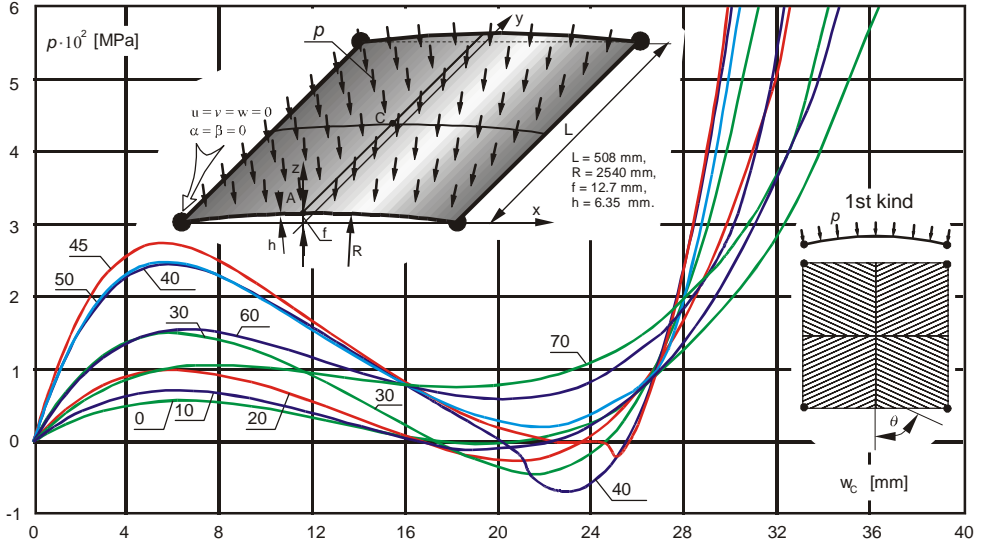


Fig. 4. Equilibrium paths for the shell of the first kind and θ from the interval of 0–70

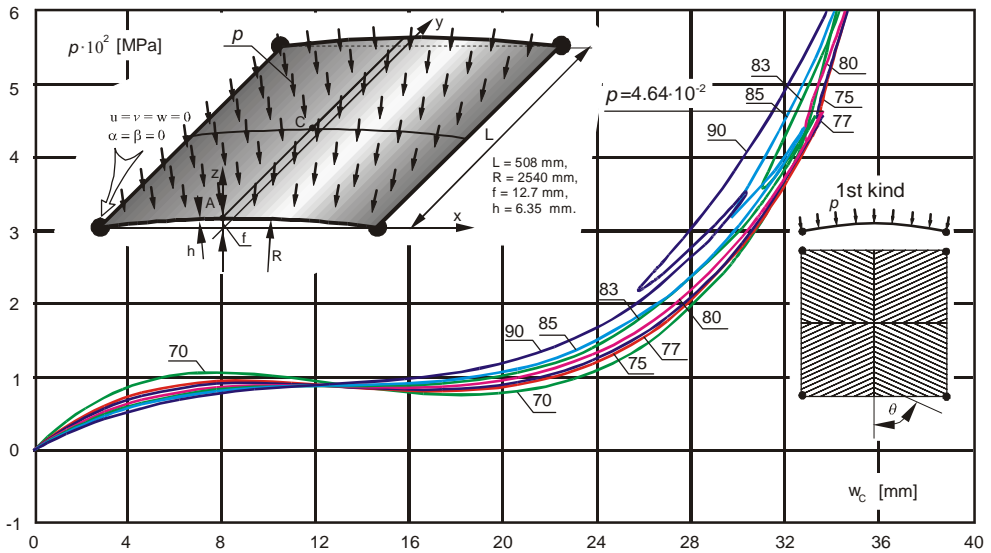


Fig. 5. Equilibrium paths for the shell of the first kind and θ from the interval of 70–90

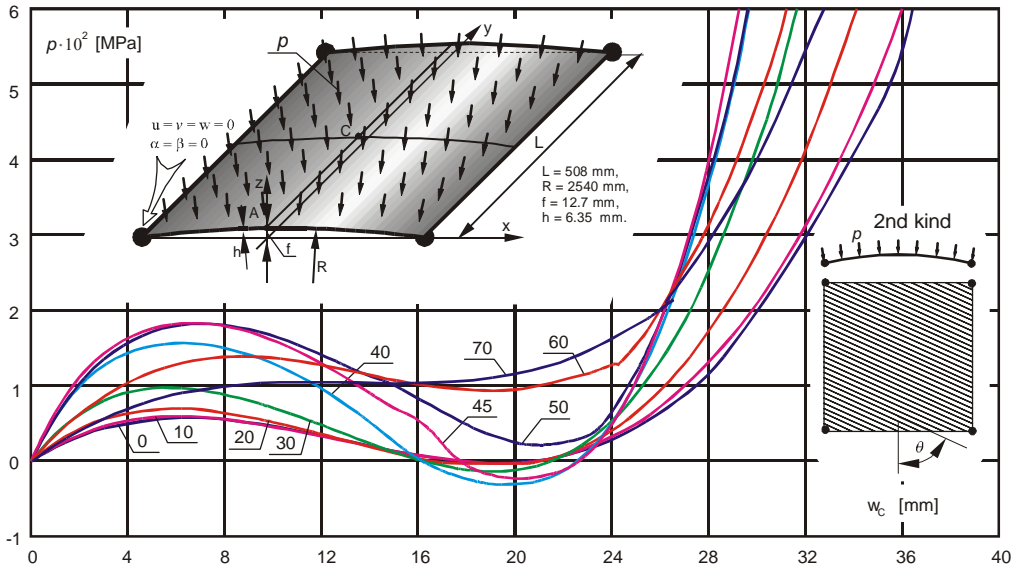


Fig. 6. Equilibrium paths for the shell of the second kind and θ from the interval of 0–70

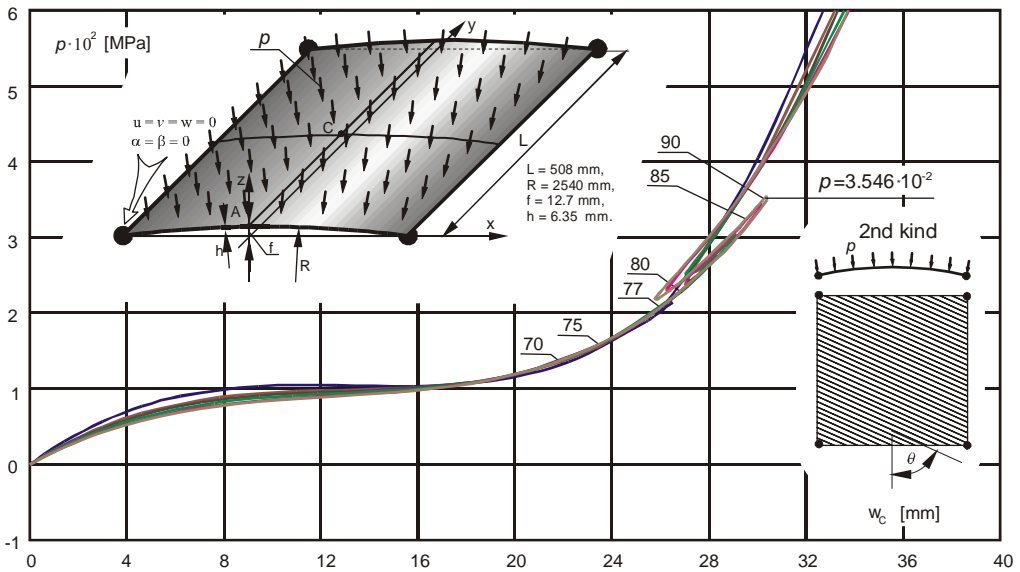


Fig. 7. Equilibrium paths for the shell of the second kind and θ from the interval of 70–90

Calculations were done for two variants of the shell termed above as the first and the second kinds (see Figure 3) and for the angles θ from the interval of $\langle 0, 90^\circ \rangle$. In

every case, a complete geometrically nonlinear equilibrium path was calculated. A primary critical point (no matter what kind of a critical point it was) was determined on the equilibrium path as a result of calculations. The corresponding pressure level has defined the maximized objective function for the particular value of θ .

The complete equilibrium paths for both kinds of shell and for different angles of θ were presented in Figures 4, 5, 6 and 7. It is interesting to note that the character of these curves changes. When θ increases, a critical value of the pressure corresponding to the limit point increases as well. This tendency is true only for θ 's smaller than 45° . For greater θ 's this tendency is reversed. It can be observed that for $\theta \approx 70^\circ$ the limit point which has appeared for comparatively small displacements vanishes and in its place the limit point appears in the remote region of relative strengthening of the shell.

Table. Critical values of pressure for both kinds of shells and different values of θ

θ	p_{cr} [MPa]	
	1st kind	2nd kind
0	5.72E-03	5.72E-03
10	7.10E-03	5.93E-03
20	9.91E-03	6.97E-03
30	1.50E-03	9.64E-03
40	2.44E-03	1.56E-02
45	2.74E-03	1.83E-02
50	2.45E-03	1.82E-02
60	1.55E-03	1.39E-02
70	1.06E-03	2.14E-02
75	9.43E-03	2.58E-02
77	4.58E-02	2.76E-02
80	4.64E-02	3.04E-02
83	4.57E-02	3.31E-02
85	4.42E-02	3.45E-02
90	3.55E-02	3.55E-02

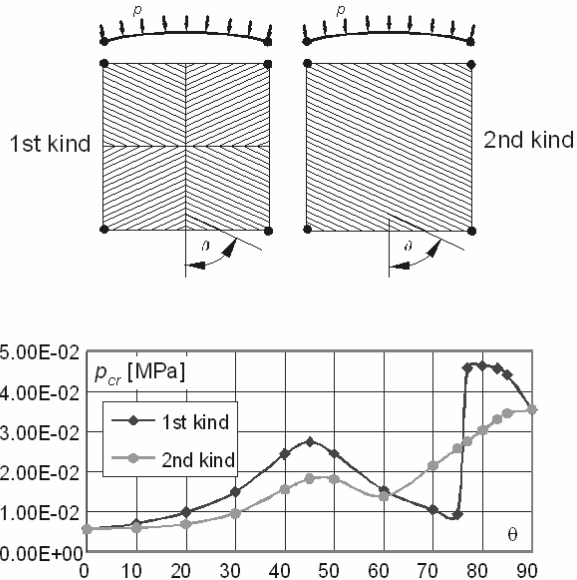


Fig. 8. The plot $p_{cr}(\theta)$

The critical values of the pressure for both kinds of shells and different values of θ were presented in the Table. p_{cr} versus θ was depicted in Figure 8 as well. The shell of the 2nd kind reaches the maximum critical pressure for $\theta = 90^\circ$ which can be felt intuitively. The shell of the first kind reaches the maximum load capacity (in the sense mentioned above) at $\theta = 80^\circ$ and this particular value is by 30.7 % higher than the result for its counterpart at $\theta = 90^\circ$. This interesting observation is a result of the analysis performed.

5. Concluding remarks

Due to high manufacturing costs the structures and structural members made of reinforced composites should be optimized with respect to the best orientation of the most expensive phase – the fibers. It is obvious that the theoretical proposals must be in agreement with technological possibilities.

In the paper, it was shown that there is the possibility of increasing the stability resistance of the shells made of fibrous composites due to properly chosen directions of reinforcing fibers. The stability phenomenon was treated as it deserves for this means that fully geometrically nonlinear analysis was adopted. In some problems (the one inserted is an example) “snap-through” phenomenon will be decisive, in other – bifurcation phenomenon will decide the stability resistance.

It is difficult to predict in advance which of the orientations of fibers should be the best. The optimum distribution of fibers depends on the shell geometry, on boundary conditions and on the external load distribution. Every case should be treated individually and to this end the procedure presented in the paper should be adopted. The presented numerical procedure leading to the best distribution of reinforcing fibers is general, of course in limits of the assumptions adopted.

The segment of cylindrical shell analysed in the paper was chosen as an example. It has confirmed the effectiveness of the procedure adopted and the ability of author’s software.

References

- [1] Śleziona J.: *Podstawy technologii kompozytów (Technological backgrounds of composites, in Polish)*, Gliwice, Wydawnictwa Politechniki Śląskiej, 1998.
- [2] Wilczyński A.P.: *Polimerowe kompozyty włókniste (Polimer fibrous composites, in Polish)*, Warszawa, WNT, 1996.
- [3] Dąbrowski H.: *Wstęp do mechaniki materiałów kompozytowych (Introduction to mechanics of composite materials, in Polish)*, Wrocław, Wydawnictwo Politechniki Wrocławskiej, 1989.
- [4] Klasztorny M., Urbański A.: *Zastosowanie metody elementów skończonych do weryfikacji teorii wzmocnienia kompozytu włóknistego (Analysis of elastic and viscoelastic properties of fibrous polymeric composites, in Polish)*, Materiały z II Sympozjonu: *Kompozyty, Konstrukcje warstwowe*, Wrocław–Karpacz, 7–9 listopada 2002, Dolnośląskie Wydawnictwo Edukacyjne, Wrocław, 2002.
- [5] Ahmad S., Irons B.M., Zienkiewicz O.C.: *Analysis of thick and thin shell structures by curved finite elements*, Int. J. Num. Meth. Engg., 1970, 2, pp. 419–451.
- [6] Marcinowski J.L.: *Nieliniowa stateczność powłok sprężystych (Nonlinear stability of elastic shells, in Polish)*, Wrocław, Oficyna Wydawnicza Politechniki Wrocławskiej, 1999.
- [7] Hsuah-Teh Hu, Bor-Horng Lin: *Buckling optimization of symmetrically laminated plates with various geometries and end conditions*, Composite Science and Technology, 1995, Vol. 55, pp. 277–285.

Optymalna orientacja włókien w powłoce wykonanej z kompozytów włóknistych

Przedmiotem rozważań są powłoki wykonane z kompozytów włóknistych. Można zwiększyć nośność takich powłok przez umiejętne rozmieszczenie włókien wzmacniających strukturę kompozytu. Kształt i obciążenie analizowanych powłok mają taki charakter, że powłoka jest czuła na utratę stateczności i właśnie stateczność decyduje o jej nośności.

Rozważa się powłoki zbrojone jednokierunkowo, a przedmiotem poszukiwań jest taki kierunek zbrojenia, który pozwala otrzymać maksymalną wartość obciążenia krytycznego. Aby rozwiązać tak sformułowany problem, zastosowano podejście numeryczne oparte na autorskim programie do geometrycznie nieliniowej analizy powłok uwzględniającej zjawiska stateczności sprężystej. Powłoki z kompozytów włóknistych można traktować jako powłoki ortotropowe o znanych parametrach materiałowych. Znając kierunki ułożenia włókien oraz kierunki lokalnego układu współrzędnych wewnątrz elementu skończonego, można było sformułować prawa transformacji macierzy stałych sprężystości i w ten sposób poprawnie sformułować związek konstytutywny. Obciążenia krytyczne dla danego ułożenia włókien były znajdowane w rezultacie przeprowadzonej pełnej analizy numerycznej. Otrzymane wyniki dla wszystkich możliwych układów włókien pozwalają ustalić ich optymalny kierunek. Jako przykład zamieszczono rozwiązanie dla mało wyniosłej powłoki walcowej obciążonej poprzecznie.

The effect of crashworthiness parameters on the behaviour of car-body elements

Z. GRONOSTAJSKI, P. BANDOŁA, P. KARBOWSKI

Wrocław University of Technology, Wybrzeże Wyspiańskiego 27, 50-370 Wrocław

In the paper, special emphasis was put on the structural stiffness of car elements described by crashworthiness parameters. We showed how the structure parameters described by crashworthiness indicators can be calculated for various structures. The effect of crashworthiness parameters of different constructions and profiles on the relationship between the energy absorption and the maximum collision force is given. One- and multi-layer, empty and filled with different-density plastic foam elements were described. The behaviour of different elements and the effect of plastic foam density on the crashworthiness parameters were analyzed.

Keywords: *car elements, dynamic loading, crash test*

1. Introduction

The main goal of passive safety is to minimize a threat to life or health of persons involved in a road accident. The biggest danger to the passengers involved in such an accident comes from overloads that result from the energy conservation law. A decrease of overloads is obtained by such a vehicle design that enables an appropriate collision energy absorption and dissipation. This aim is achieved by the use of the so-called deformation zones created from the elements of different characteristics of energy absorption.

Improvements in automotive design are encouraged by the need to decrease the weight of vehicles which allows the fuel consumption and the production costs to be reduced. The reduction in weight decreases the strength of structure, which can be defined by structural stiffness [1, 2]. If deformation takes place in regular and controlled manner, we deal with the most desirable mode of a dynamic collapse of structure. The structural stiffness of structures can be described by crashworthiness factors. The main aim of the paper was to derive the equations for calculating crashworthiness factors of various structures investigated, to determine their values, and to find the relationship between crashworthiness factors of different structures and the ratio of dissipation energy to maximum force.

2. Crashworthiness parameters

Crashworthy car elements should be characterized by efficient and controllable energy absorption and the collapse force below the maximum tolerances allowable for

car user. To assess the performance of different elements during car accident the following indicators should be taken into account [3]:

- The maximum load P_{\max} . It is the force required for initiating deformation and energy absorption process. This load should be within the tolerance limit for user.
- The mean load P_m defined by

$$P_m = \frac{E_a}{\delta_f}, \quad (1)$$

where:

E_a – the energy absorbed during deformation,

δ_f – the plastic axial displacement.

It is an indicator of a car's ability to absorb energy. For a vehicle designer this value is important as the length of energy-absorbing car elements must be practically restricted. However, too high a mean load value of energy-absorbing structure leads to high deceleration and to the death of car users.

Energy absorption E_a represents the stable limit of a structure and allows comparing different structure designs. The stable limit is terminated when the deformation process becomes unstable or fully stable deformation is finished.

- Crash efficiency e_0 is a good indicator of the amount of material used within stable deformation limit, because not all of the energy-absorbing structure is utilized during that limit. The crash efficiency is given by [4]

$$e_0 = \frac{\delta_f}{l}, \quad (2)$$

where l is the specimen length.

If each element is deformed in a stable manner, the crush efficiency is very high. For little energy-absorbing structure the crush efficiency is poor. Plastic displacement used to calculate the crush efficiency is the value at which unstable deformation begins or fully stable deformation is finished.

- Structural effectiveness η . It allows the structures made of different material properties to be compared [5, 6]

$$\eta = \frac{P_m}{A\sigma_p}, \quad (3)$$

where:

A – the cross-section of structure,

σ_p – the flow stress of material used in structure.

The above mentioned parameters describe physical properties which depend on the geometry of the elements investigated. It is possible to assess the effect of different geometry of elements on the crashworthiness, provided that the geometry is precisely defined. Therefore the methods of description of elements geometry shown in Figures 1–4 were considered.

The simple rectangular and round specimens were made from different kinds of steel and in the case of specimens with double walls, their outer walls were made from steel, and inner walls from PA38 aluminium alloy. Besides the space between the walls in some elements was filled up with the plastic foam [7, 8].

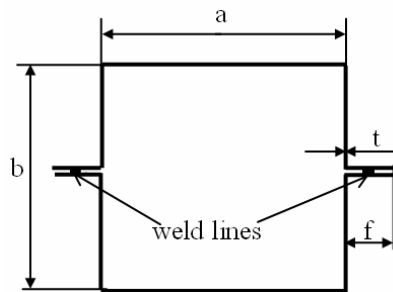


Fig. 1. Cross-section of a rectangular specimen with a single wall

The elements shown in Figure 1 are characterized by the following factors:

- Section ratio β . It can be used to compare the elements of different sections and is defined by

$$\beta = \frac{\text{area of box section}}{\text{area of flange}} = \frac{2(a+b)t}{4ft} = \frac{a+b}{2f}. \quad (4)$$

For specimens filled up with the plastic foam

$$\beta = \frac{2(a+b)t + \psi_1 ab}{4ft}, \quad (5)$$

where:

ψ_1 – the coefficient of the ratio of compression ultimate strength of plastic foam of different density to ultimate strength of steel E275 used for making a box equal to $\sigma_{pf} / \sigma_{pE275}$,

σ_{pf} – the ultimate strength of plastic foam with applied density σ_{pf} ,

σ_{pE275} – the ultimate strength of box material.

If the coefficient of compressibility of foam κ is multiplied by the coefficient of the ratio of compression stress, it is possible to express the plastic foam by the properties of box material.

- Stability ratio α . It is represented by the ratio of cross-sectional area to the length of element l . By using this factor, the influence of specimen length and cross-sectional dimension on the energy-absorbing capacity can be considered. For empty specimens it is given by

$$\alpha = \frac{2(a+b+2f)t}{l}, \quad (6)$$

and for specimens filled up with the plastic foam by

$$\alpha = \frac{2(a+b+2f)t + \psi_1 ab}{l}. \quad (7)$$

- Structural density. It is given by the ratio of the material volume to the element volume. Using this factor, the usage of material can be assessed for different elements absorbing energy. For empty specimens it is given by

$$\phi = \frac{2(a+b+2f)tl}{abl} = \frac{2(a+b+2f)t}{ab}, \quad (8)$$

and for element filled up with the plastic foam by

$$\phi = \frac{2(a+b+f)tl + \psi_1 abl}{abl} = \frac{2(a+b+2f)t + \psi_1 ab}{ab}. \quad (9)$$

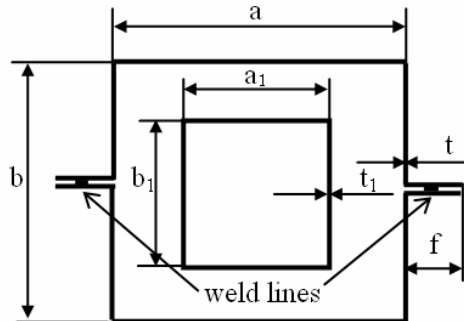


Fig. 2. Cross-section of the rectangular specimen with double walls

In the case of the elements with double walls shown in Figure 2, the following factors were used:

Section ratio of empty element is given by

$$\beta = \frac{2(a+b)t + 2(a_1+b_1)t_1}{4ft} = \frac{(a+b)t + \psi_2(a_1+b_1)t_1}{2ft}, \quad (10)$$

and of the element filled up between outer and inner boxes with the plastic foam by

$$\begin{aligned} \beta &= \frac{2(a+b)t + 2\psi_2(a_1+b_1)t_1 + \psi_1(ab - a_1b_1)}{4ft} \\ &= \frac{2[(a+b)t + \psi_2(a_1+b_1)t_1] + \psi_1(ab - a_1b_1)}{4ft}, \end{aligned} \quad (11)$$

where ψ_2 is the coefficient of the ratio of ultimate strength σ_{pPA38} of inner box from aluminium alloy PA38 to ultimate strength of outer box from steel E275 ($\sigma_{pPA38} / \sigma_{pE275}$).

The stability ratio of empty specimens is given by the reduced cross-sectional area to the length of the element. In reduced cross-sectional area, the effect of position of inner rectangular walls on the stability of element is taken into account. This position is closer to the axis of specimen than the position of outer walls. Therefore the coefficients expressed by b_1/b and a_1/a were introduced:

$$\alpha = \frac{2(a+b+2f)t + 2\psi_2\left(a_1\frac{b_1}{b} + b_1\frac{a_1}{a}\right)t_1}{l}. \quad (12)$$

In the case of the element filled up in the same way as before with the plastic foam, the effect of the position of foam should be taken into account as well. Therefore the reverse coefficients b/b_1 and a/a_1 were applied

$$\alpha = \frac{2(a+b+2f)t + 2\psi_2\left(a_1\frac{b_1}{b} + b_1\frac{a_1}{a}\right)t_1 + \psi_1(ab - a_1b_1)\frac{a}{a_1}\frac{b}{b_1}}{l}. \quad (13)$$

Structural density of an empty element with double walls is given by

$$\phi = \frac{2(a+b+2f)tl}{abl} + \frac{2(a_1+b_1)t_1l}{a_1b_1l} = \frac{2(a+b+2f)t}{ab} + \frac{2\psi_2(a_1+b_1)t_1}{a_1b_1}, \quad (14)$$

and of the element filled up with the plastic foam by

$$\begin{aligned}\phi &= \frac{2(a+b+2f)tl}{abl} + \frac{2\psi_2(a_1+b_1)t_1l}{a_1b_1l} + \frac{\psi_1(ab-a_1b_1)l}{abl} \\ &= \frac{2(a+b+2f)t + \psi_1(ab-a_1b_1)}{ab} + \frac{2\psi_2(a_1+b_1)t_1}{a_1b_1}.\end{aligned}\quad (15)$$

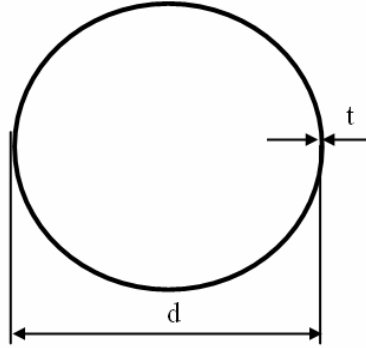


Fig. 3. Cross-section of the round specimen

In the case of the element shown in Figure 3, the above mentioned factors are expressed by the following formulas:

Section ratio

$$\beta = \frac{\pi dt}{0} = \infty, \quad (16)$$

and of specimens filled up with plastic foam by

$$\beta = \frac{\pi dt + \psi_3 \pi d^2 / 4}{0} = \infty, \quad (17)$$

where ψ_3 is the coefficient of the ratio of compression ultimate strength σ_{pR35} of plastic foam of different density to ultimate strength of the box from steel R35 ($\sigma_{pR35}(\sigma_{pf}/\sigma_{pR35})$)

Stability ratio of empty specimens is given by

$$\alpha = \frac{\pi dt}{l}, \quad (18)$$

and of specimens filled up with plastic foam by

$$\alpha = \frac{\pi dt + \psi_3 \pi d^2 / 4}{l}. \quad (19)$$

Structural density of empty specimens

$$\phi = \frac{\pi dtl}{\pi d^2 l / 4} = \frac{4t}{d}, \quad (20)$$

and of the specimens filled up with the plastic foam by

$$\phi = \frac{\pi dtl + \pi d^2 l \psi_3 / 4}{\pi d^2 l / 4} = \frac{4t + \psi_3}{d}. \quad (21)$$

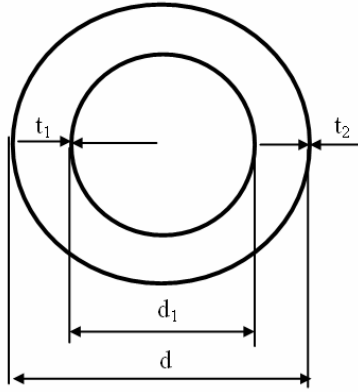


Fig. 4. Cross-section of the round specimen with double walls

Round element with double wall is shown in Figure 4.

Section ratio of empty specimens shown in Figure 4 is given by

$$\beta = \frac{\pi dt + \pi d_1 t_1}{0} = \infty, \quad (22)$$

and of specimens filled up with the plastic foam by

$$\beta = \frac{\pi dt + \pi \psi_4 d_1 t_1 + \psi_3 \pi (d^2 - d_1^2) / 4}{0} = \infty, \quad (23)$$

where ψ_4 is the coefficient of the ratio of ultimate strength σ_{pPA38} of inner box from aluminium alloy PA38 to ultimate strength σ_{pR35} of outer box from steel R35 ($\sigma_{pPA38}/\sigma_{pR35}$).

Stability ratio of empty specimens is given by

$$\alpha = \frac{\pi dt + \pi \pi_4 d_1 t_1 \left(\frac{d_1}{d}\right)^2}{l}, \quad (24)$$

and of specimens filled up with the plastic foam by

$$\alpha = \frac{\pi dt + \pi \psi_4 d_1 t_1 \left(\frac{d_1}{d}\right)^2 + \psi_3 \pi d^2 \left(\frac{d_1}{d}\right)^2 / 4}{l}. \quad (25)$$

Structural density of empty specimens

$$\phi = \frac{\pi dtl}{\pi d^2 l / 4} + \frac{\pi \psi_4 d_1 t_1 l}{\pi d_1^2 l / 4} = \frac{4t}{d} + \frac{4t_1}{d_1}, \quad (26)$$

and of specimens filled up with the plastic foam by

$$\phi = \frac{\pi dtl}{\pi d^2 l / 4} + \frac{\pi \psi_4 d_1 t_1 l}{\pi d_1^2 l / 4} + \frac{\psi_3 \pi (d^2 - d_1^2) l}{\pi d^2 l} = \frac{4t}{d} + \frac{4\psi_4 t_1}{d_1} + \frac{\psi_3 (d^2 - d_1^2)}{d^2}. \quad (27)$$

3. Experimental procedure

The rectangular and round tube elements with single and double walls used in experiments are shown in Figures 5 and 6 [9]. The drop hammer for dynamic deformation of these elements is shown in Figure 7 [10, 11].

Main parts of the test stand (Figure 7) were as follows:

- automated drop hammer with a ram of a weight from 58.5 kg up to 206 kg depending on the number of bobs,
- computerized data recording system connected with appropriate sensors and devices recording signals during sample deformation,
- software visualizing the test results obtained.

The mechanical properties of steel E275D used for rectangular element, steel R35 for tube element and aluminium alloy PA38 used for inner square and round elements are given in Table 1. The density and effect of strain rate on the ultimate compression strength of plastic foam RR3040, named Alfapur, of different densities are shown in Table 2.

In order to establish the crashworthiness factors of the elements shown in Figures 1–6 and given by Equations (4)–(27), first of all the coefficients ψ_1 , ψ_2 , ψ_3 , ψ_4 al-

lowing transformation of the comparative effect of plastic foam with different densities and aluminium alloy PA38 into effect of outer box material should be calculated. To that end the data given in Tables 1 and 2 were used. The values of coefficient are gathered in Table 3.

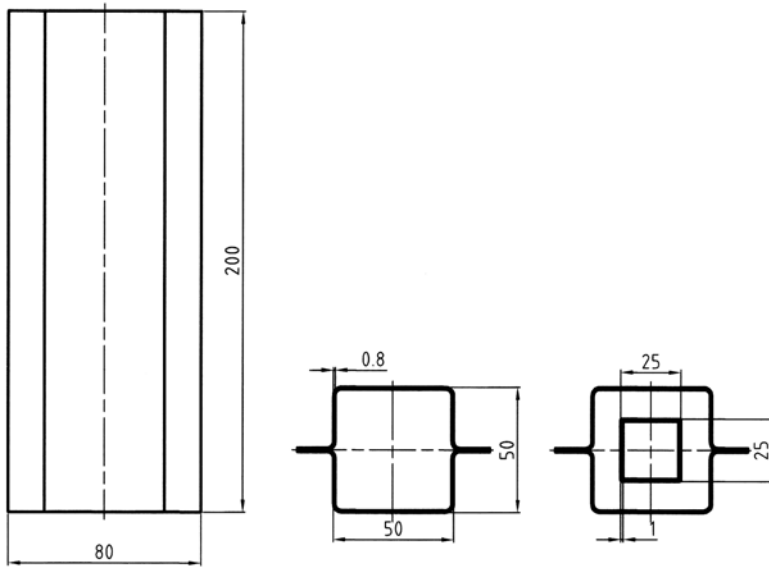


Fig. 5. Symmetrical rectangular elements with single and double walls

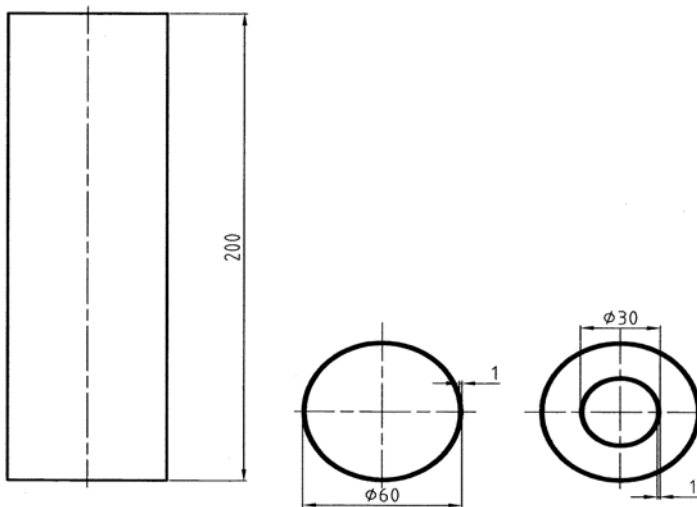


Fig. 6. Round elements with single and double walls

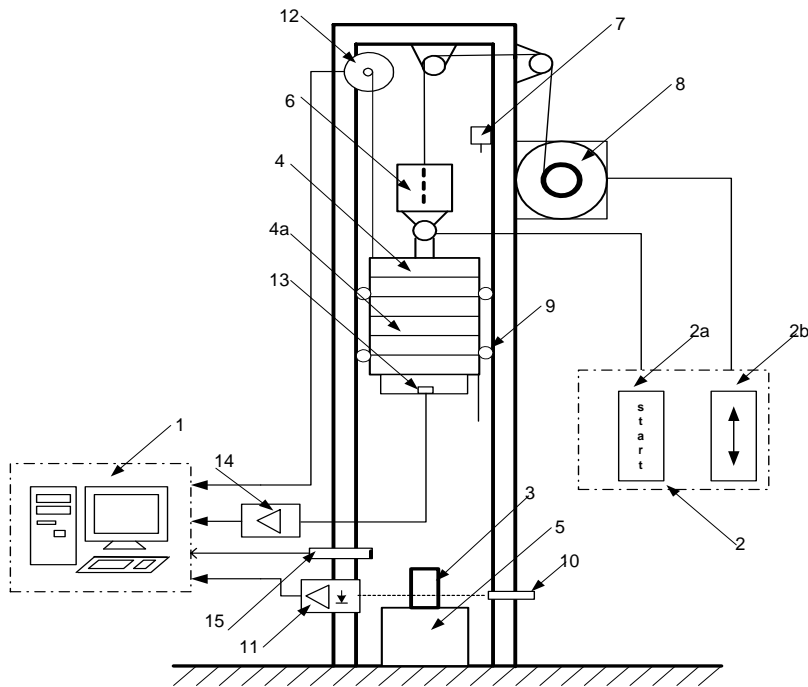


Fig. 7. The test stand scheme: 1 – data acquisition system, 2 – manual control of the ram displacement, 2a – ram release, 2b – ram position setting, 3 – specimen, 4 – ram, 4a – hammer bobs, 5 – anvil, 6 – electromagnet, 7 – limit switch, 8 – electric motor, 9 – rolling bearings, 10 – laser transmitter, 11 – exalted-carried receiver, 12 – rate generator, 13 – piezoelectric sensor, 14 – piezoelectric sensor amplifier, 15 – distance release sensor

Table 1. Mechanical properties of the steel and aluminium alloy used [12]

Kind of materials	Mechanical properties		
	Yield stress [MPa]	Ultimate tensile strength [MPa]	Elongation [%]
E275D	275	390	27
R35	215	360	24
PA38	140	315	21

Table 2. Effect of strain rate on the ultimate compression strength of plastic foam Alfapur [12]

Density, [kg/m ³]	Ultimate compression strength [MPa]		
	Strain rate [s ⁻¹]		
	4×10 ⁻³	1.7×10 ⁻¹	3.3×10 ⁻¹
54.0	0.201	0.239	0.267
82.7	0.419	0.487	0.489
119.7	0.833	0.939	0.975
156.5	1.146	1.585	1.504
203.0	2.040	2.339	2.605

Table 3. Coefficients ψ_i for the densities of plastic foam, steels and aluminium alloy

Density	Coefficient ψ_1	Coefficient ψ_2	Coefficient ψ_3	Coefficient ψ_4
54.0	0.0007	0.80769	0.0007	0.87500
82.7	0.0013		0.0014	
119.7	0.0025		0.0027	
156.5	0.0039		0.0042	
203.0	0.0068		0.0072	

The crashworthiness factors of the elements shown in Figures 1–6 are given in Table 4.

From Figures 8–10 it can be seen that the effect of foam density converted into the properties of outer box materials on the crashworthiness factors β and ϕ is minimal (Figures 8 and 10). The factor α is more sensitive to the foam density, especially in the case of double-walled elements (Figure 9). The factor β cannot be used for elements without flange, as in the case of round elements. In all cases, the values of the crashworthiness factor are much higher for the double-walled elements than for single-walled elements.

Table 4. Crashworthiness factors of elements shown in Figures 1–6

Crashworthiness factors	Density of plastic foam	Rectangular elements		Round elements	
		Single wall	Double walls	Single wall	Double walls
β	0	4.1667	6.2700	∞	∞
	54.0	4.2122	6.3042	∞	∞
	82.7	4.2513	6.3335	∞	∞
	119.7	4.3294	6.3921	∞	∞
	156.5	4.4206	6.4605	∞	∞
	203.0	4.6094	6.6021	∞	∞
α	0	0.992	1.1535	0.94200	1.04503
	54.0	1.00075	1.1798	0.95189	1.04750
	82.7	1.00825	1.2023	0.96178	1.04998
	119.7	1.02325	1.2473	0.98015	1.05457
	156.5	1.04075	1.2998	1.00135	1.05987
	203.0	1.0770	1.4085	1.04374	1.07047
ϕ	0	0.04736	0.208950	0.066667	0.183333
	54.0	0.04806	0.209115	0.066678	0.183858
	82.7	0.04866	0.209565	0.066690	0.184383
	119.7	0.04986	0.210465	0.066712	0.185358
	156.5	0.05126	0.211515	0.066737	0.186483
	203.0	0.05416	0.213690	0.066787	0.188733

The effect of foam density on the crashworthiness factors β , α and ϕ is shown in Figures 8–10, respectively.

If the greatest operational safety of the whole structure and of its elements is taken into account, it can be said that it needs a high value of energy dissipation during collision and low value of maximum force, i.e., low value of maximum acceleration. The energy dissipation and the maximum force of the structures described are given in [13,

14]. The effect of crashworthiness factors β , α and ϕ on the ratio of the dissipation energy to the maximum force was calculated and presented in Figures 11–13. In the case of the crashworthiness factor β , only rectangular elements can be analyzed (Figure 11). From that figure it can be seen that the elements with single walls have a better ratio of dissipation energy to maximum force than the elements with double walls, and the rectangular elements of single walls and the round elements with double walls have almost the same ratio. Also the relationship between the crashworthiness factors (α and ϕ) and the dissipation energy to the maximum force ratio (Figures 12 and 13) proves that the round elements with single walls and the foam density applied are the best.

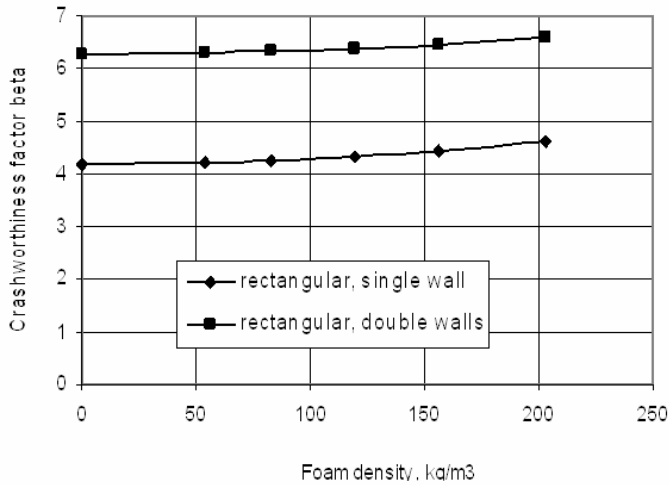


Fig. 8. The effect of foam density on the crashworthiness factor β

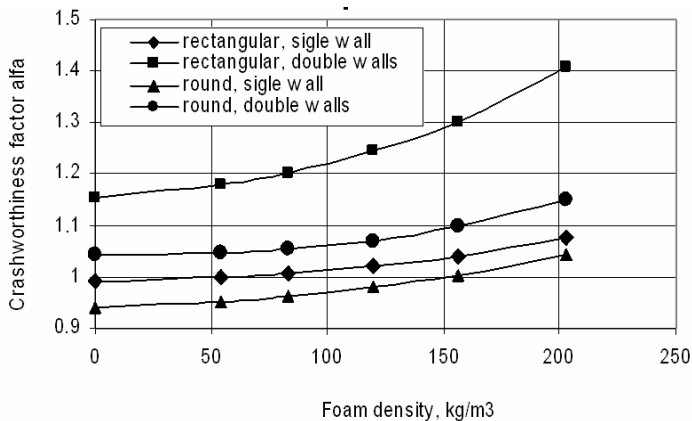


Fig. 9. The effect of foam density on the crashworthiness factor α

During collision the rectangular elements with single walls and different density of plastic foam behave in the same way as round elements with double walls. Rectangular elements with double walls are characterized by the worst energy dissipation.

4. Results and discussion

In order to find the best structure that is characterized by an efficient and controllable energy absorption and the collapse force below the maximum tolerance allowable for car user, the relationship between the crashworthiness factors of the structure designed was established. To obtain a valuable information the crashworthiness factors were altered in the wide range by changing a structure as is shown in Figures 1–4 and by applying plastic foam of the density ranging from 50 to about 200 kg/m³. The effect of plastic foam density on the crashworthiness factors β and ϕ is minimal; only the factor α is more sensitive to the foam density, especially in the case of double-walled elements. In all cases, the crashworthiness factors are much higher for the double-walled elements than for single-walled elements.

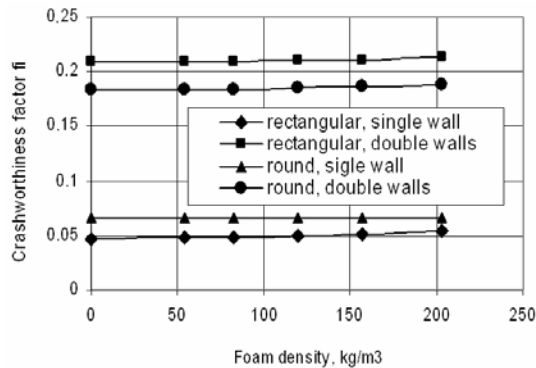


Fig. 10. The effect of foam density on the crashworthiness factor ϕ

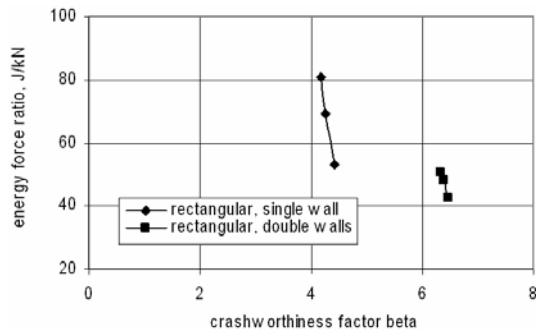


Fig. 11. The effect of the crashworthiness factor β on the energy to force ratio of rectangular elements with single and double walls

The elements with single walls are characterized by better ratio of the dissipation energy to the maximum force than the elements with double walls, and almost the same ratio is typical of the round elements with double walls and the rectangular elements with single wall. The best are round elements with single walls and the foam density applied, because they are deformed in a stable manner (Figures 14a and 14b). Therefore the crush efficiency is very high and due to application of such elements in a vehicle structure, the collision energy can be absorbed and dissipated making a car more safety. The rectangular elements with single walls and different densities of plastic foam behave during collision in the same way as round elements with double walls (Figure 14c). This means that during dynamic deformation of such elements very often highly undesirable mode of collapse takes place and overall buckling of the structure occurs. Rectangular elements with double walls are considered to have the worst properties of energy dissipation.

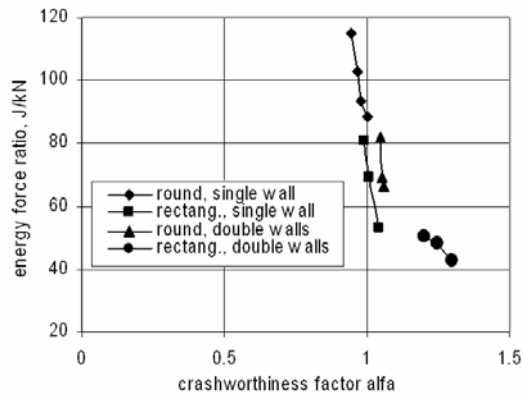


Fig. 12. The effect of the crashworthiness factor α on the energy to force ratio of rectangular and round elements with single and double walls

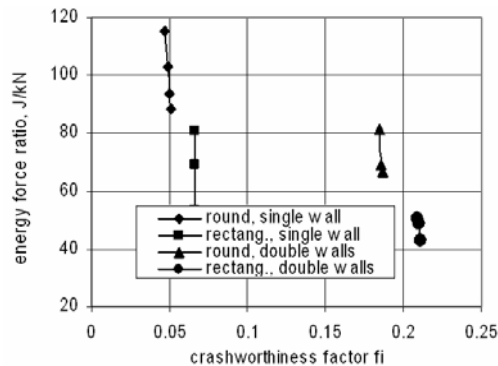


Fig. 13. The effect of the crashworthiness factor ϕ on the energy to force ratio of rectangular and round elements with single and double walls



Fig. 14. Elements after deformation: a) round with single wall, empty, b) round with single wall filled with the foam whose density is 119.7, c) rectangular with single wall filled with the foam whose density is 119.7

The crashworthiness factors of the structures designed should reduce a significant increase in acceleration that is very dangerous for the safety of car users. Therefore, future investigations should be undertaken to find such a structure, density, and kind of foam that allow a low acceleration and stable manner of the structure deformation.

References

- [1] Jones N., Birch R.S.: *Dynamic and static axial crushing of axially stiffened square tubes*, Proc. of the Institution of Mechanical Engineers, 1990, 204 (Part C), 293–310.
- [2] Birch R.S., Jones N.: *Dynamic and static axial crushing of axially stiffened cylindrical shells*, Thin Walled Structures, 1990, 29–60.
- [3] White M.D., Jones N.: *Experimental quasi-static axial crushing of top-hat and double-hat thin-walled sections*, Int. J. of Mechanical Sciences, 1999, 41, 179–208.
- [4] Mage C.L., Thornton P.H.: *Design consideration in energy absorption by structural collapse*, Paper 780434, presented at SAE Annual Meeting, Detroit, 1978.
- [5] Thornton P.H.: *Energy absorption by structural collapse of spot-welded sheet metal section*, SAE Paper 800372, 1980.
- [6] Jones N.: *Structural impact*, Cambridge, Cambridge University Press, 1989, paperback edition, 1997.
- [7] Reid S.R., Reddy T.Y., Gray S.: *Static and dynamic axial crushing of foam filled sheet metal tube*. Int. J. of Mechanical Science, 1986, 28, 295–322.
- [8] Reddy T.Y., Wall R. J.: *Axial compression of foam filled thin walled circular tubes*, Int. J. of Impact Eng., 1988, 7, 151–166.

- [9] Gronostajski J., Gronostajski Z., Niechajowicz A., Polak S., Struś M., Tobota A., Wiewiórski P., Zajac P.: *Measurement system of "crash-test" experiments*, Arch. of Civil and Mechanical Engineering, 2004, 4, 5–23.
- [10] Tobota A., Olchowik W., Domański M., Wiewiórski P.: *System pomiarowy do badania procesu zgniatania próbki w eksperymencie typu „Crash-Test”*, V Konferencja Diagnostyka Techniczna Urządzeń i Systemów, Ustroń, 2003.
- [11] Gronostajski J., Wiewiórski P.: *Computer aided measuring system of "Crash-Test" experiments*, Proc. of Int. Conf. AMME, Zakopane, 2003.
- [12] Gronostajski J., Gronostajski Z., Polak S., Struś M., Tobota A., Wiewiórski P.: *Metoda oceny odporności kolizyjnej tłoczonych elementów podczas dynamicznego odkształcania and Evaluation method of collision resistance of sheet forming elements in dynamic deformation*, XVI Int. Conf. Design and Technology of Plastic Forming Products, Poznań, 2004.
- [13] Gronostajski J., Gronostajski Z., Wiewiórski P., Polak S.: *Properties of composites in dynamical compression test*, Inżynieria Materiałowa, 2004, 25, 717–720.
- [14] Gronostajski Z., Polak S., Tobota A., Wiewiórski P.: *Analiza deformacji wybranego elementu nadwozia pochłaniającego energię zderzenia*, Mat. Międz. Konf. Forming 2005, Lednice, 2005, 69–74.

Wpływ parametrów uderzeniowych elementów karoserii samochodów na ich zachowanie się podczas kolizji

Opracowano równania opisujące parametry uderzeniowe elementów karoserii pojazdów samochodowych czułych na dynamiczne obciążanie oraz wyliczono ich wartości dla elementów prostokątnych i kołowych o pojedynczych i podwójnych ściankach wypełnionych pianką z tworzywa sztucznego o różnej gęstości lub pustych. Ustalono wpływ gęstości tworzywa sztucznego na wartość obliczonych parametrów. Stwierdzono, że większość parametrów jest niemal niezależna od gęstości pianki z tworzywa sztucznego, a jedynie jeden z nich jest bardzo czuły na gęstość pianki. Natomiast wartości parametrów w bardzo dużym stopniu zależą od liczby ścianek: dla elementów o podwójnych ściankach są one znacznie wyższe niż dla elementów o pojedynczych ściankach. Aby uzyskać wartościowe informacje o wpływie zastosowanych parametrów na zachowanie się badanych struktur, zmieniano ich konstrukcje w szerokim zakresie oraz zmieniono w dużym zakresie gęstość pianki z tworzywa sztucznych (od 50 do około 200 kg/m³).

Elementy o pojedynczej ściance charakteryzują się lepszym wskaźnikiem stosunku energii dyssypowanej do maksymalnej siły występującej podczas dynamicznego spęczania niż elementy o podwójnej ściance. Zbliżony wpływ na ten wskaźnik mają elementy kołowe o podwójnej ściance i elementy prostokątne o pojedynczej ściance. Najgorszym wskaźnikiem odznaczają się elementy prostokątne o podwójnej ściance. Najlepszym wskaźnikiem charakteryzują się okrągłe elementy o pojedynczej ściance, ponieważ odkształcają się one w sposób bardzo równomierny.

Poprawny dobór struktury opisany za pomocą parametrów czułych na dynamiczne obciążanie umożliwi istotne zmniejszenie przyspieszeń podczas kolizji pojazdów samochodowych bardzo niebezpiecznych dla ich użytkowników. Dlatego celem przyszłych prac powinno być opracowanie struktur, rodzaju i gęstości tworzyw sztucznych, które zapewniłyby stabilny sposób odkształcania się struktur prowadzący do zmniejszenia przyspieszeń do wartości dopuszczalnych.

Description of crack propagation – theoretical approach and fitting accuracy to measurement results

M. SZATA

Institute of Materials Science and Applied Mechanics, Wrocław University of Technology, ul. Smoluchowskiego 25, 50-370 Wrocław

An energy criterion of fatigue crack propagation in the isotropic body has been formulated. It is based on the first principle of thermodynamics as a balance between energy variation rates (work of external forces, energy of body deformation, fracture energy, heat energy of the body) and the surface change due to fatigue crack under a cyclic loading. Finally, a kinetic equation of fatigue fracture as an analytical relation between the rate of fatigue crack surface propagation and the dissipation energy of plastic deformation in the precracked zone has been obtained. The method of an approximate solution of such an equation and determination of the period of precritical crack growth has been suggested. This method is based on the assumption that kinetics of the surface variation of the crack studied is close to the variation of a round crack with the same surface, but the solution for a round crack is given in a closed form. The validity of this method has been confirmed in the case of an elliptical crack. A new method of constructing kinetic fatigue fracture diagrams (KFFD) has been presented on the basis of measurement results of hysteresis loop area for the isotropic body with an internal flat crack under cyclic loading. For the experimental verification, the results of fatigue crack propagation studies for 18G2A and 40H steels have been utilized. In contradistinction to the force factor K_{\max} , the energetic parameter ΔH describes synonymously the propagation rate of the fatigue crack independently of a cycle asymmetry R . The linear dependence of crack propagation rate da/dN on energy dissipation of plastic deformation before the crack tip for one loading cycle has been discussed with taking into consideration the consequences for fitting models in double logarithmic axes.

Keywords: *kinetic equation, fracture, cyclic fatigue, fracture crack rate*

1. Introduction

This paper is treated as a part of considerations dealing with the determination of a lifetime for construction elements under the cyclic loading by means of fracture mechanics. The lifetime of mechanical construction elements is assumed to be a sum of initiation processes and precritical growth of fatigue cracks until the stability is lost. The constructional materials always contain the defects of a definite (specific) dimension that is a characteristic feature of a given material and given element technology. At present, this defect dimension is introduced as a construction parameter in order to calculate the prognostic lifetime without breakdown for the construction element. Such an approach makes it possible to resolve the problem of calculating the lifetime of construction element conditioned by the time of a precritical defect growth from the dimension of construction parameter to the critical defect value.

The force criterion [2, 3] being a local criterion is frequently applied in the description of a fatigue crack growth. The rate of a crack growth is a function of intensity stress coefficients. This function based on experimental data has the exponential form in relation to K_I , as has been shown in Paris' law.

The deformation criterion [1–3] based on the δ_K -model [2] is used in the case where the plastic zone before a crack tip is of the same order as a body dimension.

The approach presented is effective in the case of a stable loading cycle without taking into account the “history” of material deformation and crack propagation. The intensity stress coefficients or the values of a crack opening become at that time the invariants of a fatigue damage. The energy approach makes it possible to take into consideration the elements mentioned earlier. Cherepanov [2] was the first who proposed such an analysis. The energetic methods have been developed in many research laboratories, for example, in Lviv by Panasiuk and his group [5].

2. Formulation of energy criterion for fatigue crack growth and definition of basic kinetic equation for this process

Let us consider an infinite body with an internal flat crack having the surface S_0 enclosed with a smooth contour L_0 (Figure 1).

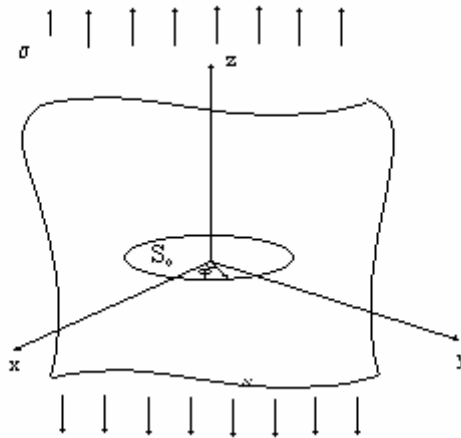


Fig. 1. Scheme of tension of the infinite body with a plane crack

The stress σ is subjected to cyclic variations and is perpendicular to the crack plane. The problem is how to deal with the determination of the period N_g of a precritical crack propagation. Using the first principle of thermodynamics we can write a global balance in the following form [2]

$$A + Q = W + K_e + \Gamma, \quad (1)$$

where:

A – the work of an external loading P (equivalent to the stress σ) after N cycles of loading,

Q – the heat input to the body during the loading,

W – a deformation energy after N cycles of loading,

K_e – a kinetic energy of the body,

Γ – a damage energy during the change of a crack surface from S_0 to S .

Differentiating Equation (1) over the number of cycles we obtain

$$\frac{\partial A}{\partial N} + \frac{\partial Q}{\partial N} = \frac{\partial W}{\partial N} + \frac{\partial \Gamma}{\partial N} + \frac{\partial K_e}{\partial N}. \quad (2)$$

Assuming that a slow growth of a crack length does not occur simultaneously with heat processes and neglecting small changes of a kinetic energy (for low frequencies of a cyclic loading) we arrive at

$$\frac{\partial A}{\partial N} = \frac{\partial W}{\partial N} + \frac{\partial \Gamma}{\partial N}. \quad (3)$$

The amount of a dissipation energy for plastic deformation before the crack tip needed for the appearance of a new fatigue fracture surface can be expressed in the following form

$$\frac{\partial(A - W)}{\partial N} = \frac{\partial(W_c + W_s)}{\partial N}, \quad (4)$$

where:

W_c – the energy of cyclic deformation changes,

W_s – a static component of energy changing with the crack growth.

After transformations

$$\frac{\partial W_c}{\partial N} = \frac{\partial(\Gamma - W_s)}{\partial S} \cdot \frac{\partial S}{\partial N}, \quad (5)$$

where $\partial S / \partial N$ is the rate of crack surface growth (S) that can be determined from (5)

$$\frac{\partial S}{\partial N} = \frac{\partial W_c}{\partial N} / \frac{\partial(\Gamma - W_s)}{\partial S}. \quad (6)$$

Let us consider the quantities of W_c , Γ and W_s . The quantity $\partial W_c / \partial N$ represents a dissipation energy of plastic deformation before a crack tip in one loading cycle (it is the area between ε_{\min} and ε_{\max} in Figure 2).

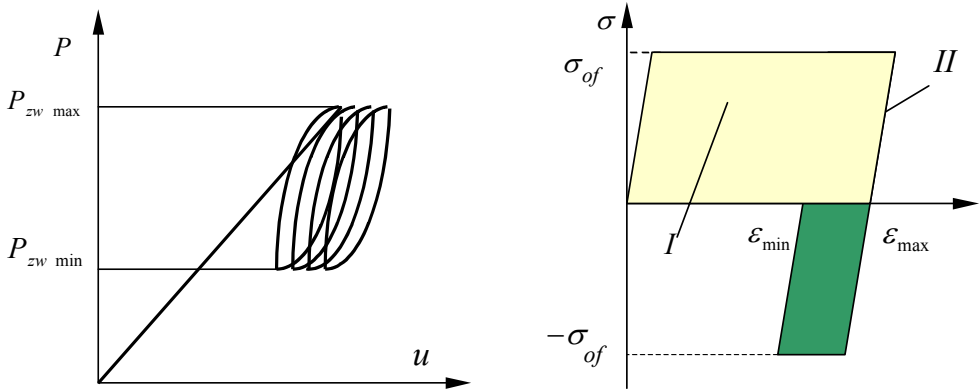


Fig. 2. The diagram of a cyclic tension of an elementary material volume in the precracked zone

As is well known from the literature [2, 3, 7], before a crack tip under a cyclic loading the two areas of prefracture are formed: a static precracked zone of the length l_s (area 1 in Figure 3) and a smaller cyclic precracked zone 2 of a the length l_c .

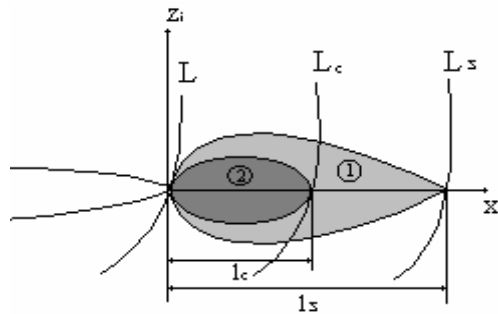


Fig. 3. Static and cyclic precracked zones

The quantities $\partial W_c / \partial N$ and $\partial W_s / \partial S$ define the plastic deformation in the areas 2 and 1, respectively. In order to define these deformations, it is necessary to use the intersection model (Figure 4) in accordance with the known Panasiuk–Dugdale’s δ_K -model [4, 6].

The stresses σ_{0f} are regularly applied along the intersection model. The magnitude of static stresses σ_{0s} can be determined according to [7] by means of the static strength characteristics of a material. The cyclic characteristic can be written as

$$\sigma_{0f} = \eta \sigma_{0s}, \quad (7)$$

(for the materials of cyclic hardening and cyclic weakening $\eta > 1$ and $\eta < 1$, respectively).

The coefficient η for a particular material can be determined experimentally by comparison of diagrams for cyclic and static tensions.

The dimensions L_f and L_s of the areas before a crack tip are considerably smaller than the dimensions of the crack itself and therefore $L_f \ll \rho$, $L_s \ll \rho$ ($\rho = \rho(\varphi)$) is the radius of a crack contour in the polar co-ordinates ρ , φ (Figure 1)).

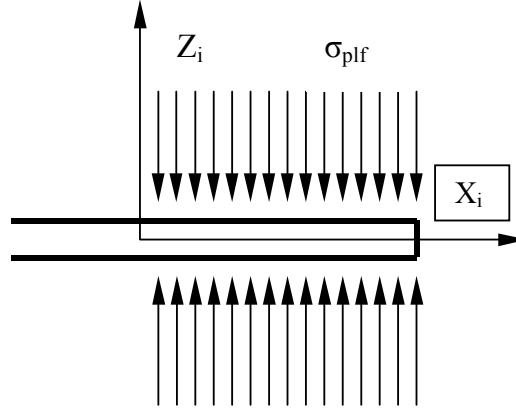


Fig. 4. A modelling of the precracked zone by a cut with stresses applied to its edges

According to [7, 8], a dissipation energy of plastic deformations before a crack tip falling to one loading cycle can be expressed by

$$\frac{\partial W_c}{\partial N} = \frac{\sigma_{0f} \varepsilon_{fc}}{\delta_{fc}} \int_L \int_0^{l_c} [\delta_{\max}^{(f)}(t, x_i) - \delta_{\min}^{(f)}(t, x_i)] dx_i dt, \quad (8)$$

where:

dt – a change of the length co-ordinate along the contour L (Figure 1),

dx – a change of the co-ordinate along the area 2 (Figure 3),

$\delta_{\max}^{(f)}(t, x_i)$ and $\delta_{\min}^{(f)}(t, x_i)$ – maximum and minimum values of the opening for the intersection model along the area before a crack tip [7] (Figure 4),

δ_{fc} – a critical value of the crack opening corresponding to the critical deformation ε_{fc} under the cyclic loading.

The value $\delta_{\min}^{(f)}(t, x_i)$ depends not only on the minimum value of the external loading P_{\min} , but also on a crack surface profile and a contact between upper and lower surfaces

$$\delta_{\min}^{(f)}(t, x_i) = \max \{ \delta_{\min}^{(fP)}(t, x_i); \delta^{(fK)}(t, x_i) \},$$

where:

$\delta^{(fK)}(t, x_i)$ – the crack opening resulting from a contact of rough surfaces and dependent on the history,

$\delta_{\min}^{(fP)}(t, x_i)$ – the minimum crack opening resulting from the external loading $P = P_{\min}$.

According to [7], δ_{\min} has a form

$$\delta_{\min}^{(fP)}(t, x_i) = \delta_{\min}^{(f)}(t, x_i) [1 - (1-R)^2 / 2],$$

where $R = K_{\min} / K_{\max}$ is the asymmetry factor of a cycle.

In the above formulas, generally known relationships $\varepsilon = \varepsilon_{fc} \delta / \delta_{fc}$ [7] between the magnitude of deformation before a crack tip and the opening of the intersection model have been used.

Similarly, we can describe the changes in a static component of a dissipation energy for plastic deformations in the precracked zone ΔS as follows

$$\frac{\partial W_s}{\partial S} = \frac{\sigma_{0f} \varepsilon_{fc}}{\delta_{fc} \Delta S} \int_L \int_0^{l_s} \delta_{\max}^{(S)}(t, x_i) dx_i dt. \quad (9)$$

The critical value of dissipation energy, i.e., the change of damage energy, can be expressed by

$$\frac{\partial \Gamma}{\partial S} = \frac{\sigma_{0f} \varepsilon_{fc}}{\delta_{fc} \Delta S} \int_L \int_0^{l_s^*} \delta_{\max}^{(S)}(t, x_i) dx_i dt, \quad (10)$$

where l_s^* is a critical length of the precracked zone ΔS .

In order to present an evident notation of the criterion equation (6) describing the propagation rate of a fatigue crack zone, the integral expression should be introduced to Equations (8) and (10). It is necessary to use the results presented in [7] expressing $\delta^{(S)}(t, x_i)$ and $\delta^{(f)}(t, x_i)$ as

$$\delta^{(S)}(t, x_i) = \frac{8\sigma_{0f}(1-\nu^2)}{\pi E} l_s^{(t)} \left[\sqrt{1-\xi} - \xi \ln \frac{1 + \sqrt{1-\xi}}{\sqrt{\xi}} \right], \quad (11)$$

$$\delta^{(f)}(t, x_i) = \alpha \delta^{(S)}(t, x_i), \quad l_f(t) = \beta \cdot l_s(t)(1-R)^2,$$

where $\xi = \frac{x_i}{l_s}$, ν , E are material constants.

Inserting (11) into (8)–(10) we obtain

$$\frac{\partial W_c}{\partial N} = \frac{0.33\sigma_{0f}\varepsilon_{fc}}{\delta_{fc}} \int_L [\delta_{\max}^{(f)}(t,0) - \delta_{\min}^{(f)}(t,0)] \cdot l_f(t) dt, \quad (12)$$

$$\frac{\partial W_s}{\partial S} = \frac{0.33\sigma_{0f}\varepsilon_{fc}}{\delta_{fc}\Delta S} \int_L \delta^{(S)}(t,0) \cdot l_S(t) dt, \quad (13)$$

$$\frac{\partial \Gamma}{\partial S} = 0.33\sigma_{0f}\varepsilon_{fc}, \quad (14)$$

$$\Delta S = \int_L l_S(t) dt. \quad (15)$$

Using the results from [7] and expressing $\delta_{\max}^{(f)}(t,0)$, $l_S(t)$ by means of stress intensity factors K_{Imax} allows Equation (12) to be written in the following form (assuming that $\delta_{\min}^{(fP)}(t, x_i) > \delta^{(fK)}(t, x_i)$)

$$\frac{\partial W_c}{\partial N} = 0.0162 \cdot \alpha \cdot \varepsilon_{fc} (1-R)^4 K_{fc}^{-2} \sigma_{plf}^{-1} \int_L K_{\text{Imax}}^4(t) dt, \quad (16)$$

where the asymmetry coefficient of a cycle R is assumed to be constant.

Similarly, Equations (13) and (15) can be expressed as follows:

$$\frac{\partial W_s}{\partial S} = 0.129 \varepsilon_{fc} K_{fc}^{-2} \sigma_{0f}^{-1} (\Delta S)^{-1} \int_L K_{\text{Imax}}^4(t) dt, \quad (17)$$

$$\Delta S = \pi 8^{-1} \sigma_{0f}^{-2} \int_L K_I^2(t) dt. \quad (18)$$

On the basis of expressions (16)–(18), the kinetic equation (6) representing the propagation of surface fatigue crack can be written as

$$\frac{\partial S}{\partial N} = 0.049 \alpha (1-R)^4 K_{fc}^{-2} \sigma_{0f}^{-2} \cdot \int_L K_{\text{Imax}}^4(t) dt \left[1 - 0.9959 K_{fc}^{-2} \left(\int_L K_{\text{Imax}}^2(t) dt \right)^{-1} \int_L K_{\text{Imax}}^4(t) dt \right]^{-1}, \quad (19)$$

$$N = 0, \quad S = S_0, \quad (20)$$

$$N = N_g, \quad S = S_*. \quad (21)$$

S_* is a critical value of a crack surface. After reaching this value the crack propagation lacks its stability and a rapid increase of the crack takes place. This surface can be determined from Irvin's criterion

$$K_{\text{Imax}}(S_*) = K_{fc}. \quad (22)$$

3. Equivalent surface method

It can be a difficult task to arrive at a closed solution to the kinetic equation (19) with conditions (20)–(22) for each shape of a crack contour L . In order to simplify this solution, the equivalent surface method has been proposed.

This method is based on the hypothesis that flat cracks occurring in a homogeneous field of tensile stresses with convex contours L and the identical surface areas S have the magnitudes similar to the areas ΔS before a crack tip and the similar energies $W_s^{(f)}$ and $W_c^{(f)}$.

Thus we can take circle of the radius R and the area $S = \pi R^2$ as the representatives. In this case, the calculations will be considerably simplified. On the grounds of this assumption, the kinetics of surface area changes for each crack with a convex contour L will be analogous to the kinetics of a circular crack with the same surface S .

For a circle we have

$$K_{\text{Imax}}^{(k)} = 2P\pi^{-3/4}S^{1/4}. \quad (23)$$

Hence, Equation (19) can be written as

$$\frac{\partial S}{\partial N} = 0.098\sqrt{\pi S} \cdot \alpha \beta \cdot K_{fc}^{-2} \sigma_{0f}^{-2} (1-R)^4 K_{\text{Imax}}^4(S) \left[1 - K_{fc}^{-2} K_{\text{Imax}}^2(S) - 1.3333\gamma(x, y) \right]^{-1}, \quad (24)$$

$$\frac{\partial S}{\partial N} = 0.0899\alpha\beta \cdot \sigma_{0f}^{-2} S \sqrt{S} P^4 (1-R)^4 \left[K_{fc}^2 - P^2 \sqrt{S} - 1.3333K_{fc}^2\gamma(x, y) \right]^{-1}. \quad (25)$$

Integrating (25), taking into account conditions (26) and putting $\gamma(x, y) = 0$, we obtain equation enabling us to determine the period N_g of the precritical crack propagation:

$$N = 0, \quad S = S_0, \quad (26)$$

$$N = N_g, \quad S = S_* = 0.0625\pi^3 K_{fc}^4 P_{\max}^{-4},$$

$$N_g = 16.051\alpha^{-1}\beta^{-1}\sigma_{0f}^2 P^{-2} \left(S_*^{1/2} S_0^{-1/2} - 1 - \frac{1}{2} \ln \frac{S_*}{S_0} \right) (1-R)^{-4}. \quad (27)$$

According to (27), for known loading parameters: P_{\max} , R , the initial surface area of the crack S_0 and its critical value S_* (formula (26)) as well as for the characteristics $\alpha, \beta, K_{fc}, \sigma_{0f}$ defined by comparing (24) with experimental data, we can obtain in this way the relationship representing the period N_g of the precritical fatigue crack propagation.

For example, let us consider an elliptic crack. The output crack contour is an ellipse described by the equation

$$\rho(\varphi) = ab(b^2 \cos^2 \varphi + a^2 \sin^2 \varphi)^{-1/2}, \quad (28)$$

where a and b are the semi-axes of an ellipse.

It is assumed that after N cycles the contour will be still an ellipse with the semi-axes $a = a(N)$, $b = b(N)$.

According to [7] the stress intensity factor is equal to

$$K_1^{(l)} = P\sqrt{\pi b} E^{-1}(k) (\sin^2 \beta + b^2 a^{-2} \cos^2 \beta)^{1/4}, \quad (29)$$

where:

$$E(k) = \int_0^{\pi/2} \sqrt{1 - k^2 \sin^2 \theta} d\theta, \quad k^2 = 1 - \xi^2, \quad \xi = \frac{b}{a},$$

$$x = a \cos \beta,$$

$$y = b \sin \beta.$$

In accordance with the equivalent surface method

$$K_{\text{Imax}}^{(k)} = 2P\pi^{-1/2} \sqrt[4]{ab}, \quad (30)$$

$$I_{11}(\xi) = \frac{I_1^{(T)}(\xi)}{I_1^{(H)}(\xi)}, \quad I_{22}(\xi) = \frac{\Delta S^{(T)}}{\Delta S^{(H)}},$$

$$I_1^{(T)} = \frac{\partial W_c^{(T)}}{\partial N} = \frac{0.0368\alpha\beta\varepsilon_{fc}(1-R)^4}{\sigma_{0f}K_{fc}^2} \left[P^4 \pi^2 a^3 \xi^2 E^{-4}(k)(2.68 + 3.6\xi^{5/2}) \right], \quad (31)$$

$$I_1^{(H)} = \frac{\partial W_c^{(H)}}{\partial N} = \frac{0.0368\alpha\beta\varepsilon_{fc}(1-R)^4}{\sigma_{0f}K_{fc}^2} \left[32P^4 \pi^{-1} a^3 \xi^{3/2} \right], \quad (32)$$

$$\Delta S^{(T)} = 0.125\pi^3 a^2 \xi \cdot P^2 \sigma_{0f}^{-2} E^{-2}(k)(2-k^2), \quad (33)$$

$$\Delta S^{(H)} = \pi a^2 \xi \cdot P^2 \sigma_{0f}^{-2}. \quad (34)$$

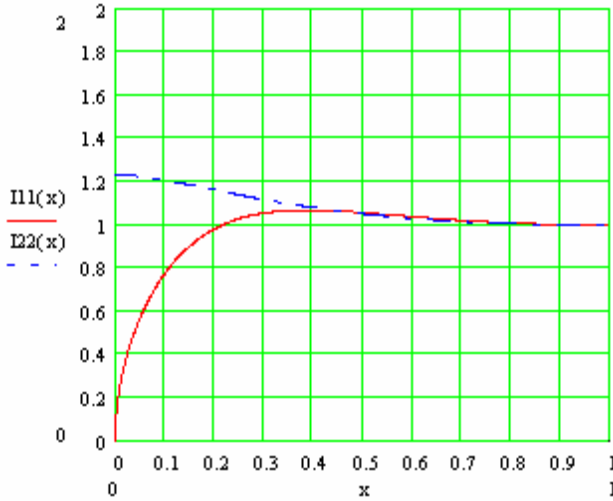


Fig. 5. A comparison of the results obtained for precise and approximate solutions in the case of an elliptical crack

4. The fitting problems

Let us consider the quantities W_c , Γ and W_s . The quantity $\partial W_c / \partial N$ is the energy dissipation of plastic deformation before a crack tip in one loading cycle. In order to obtain the equation that is appropriate for constructing the diagrams of experimental kinetic fatigue fracture, we use its simplified form without taking account of the change of a function of crack-opening displacement δ :

$$\frac{\partial \Gamma}{\partial S} = \sigma_{plf} \varepsilon_{fc} \quad \text{and} \quad \frac{\partial W_s}{\partial S} = \sigma_{plf} \varepsilon_{f \max}, \quad (35)$$

where:

σ_{plf} – a cyclic yield stress,

ε_{fc} – a critical deformation under cyclic loading.

After inserting Equations (35) into (6) we obtain

$$\frac{\partial(\Gamma - W_s)}{\partial S} = \sigma_{plf} \varepsilon_{fc} - \sigma_{plf} \varepsilon_{f \max} = \sigma_{plf} \varepsilon_{fc} \left(1 - \frac{\varepsilon_{f \max}}{\varepsilon_{fc}} \right). \quad (36)$$

The following equations are satisfied for Panasiuk–Dugdale’s δ_K -model and for a plane stress [2, 5]

$$\delta = \frac{K_{I \max}^2}{E \sigma_{plc}}, \quad \delta_c = \frac{K_{fc}^2}{E \sigma_{plc}}, \quad \frac{\varepsilon}{\varepsilon_{fc}} = \frac{\delta}{\delta_c} = \frac{K_{I \max}^2}{K_{fc}^2}. \quad (37)$$

Using Equation (37) we can express Equation (35) as follows:

$$\frac{\partial(\Gamma - W_s)}{\partial S} = \sigma_{plf} \varepsilon_{fc} - \sigma_{plf} \varepsilon_{f \max} = \sigma_{plf} \varepsilon_{fc} \left(1 - \frac{\varepsilon_{f \max}}{\varepsilon_{fc}} \right) = \sigma_{plf} \varepsilon_{fc} \left(1 - \frac{K_{I \max}^2}{K_{fc}^2} \right). \quad (38)$$

Using $W_c^{(1)} = \partial W_c / \partial N$ to denote the energy dissipation of cyclic plastic deformation before a crack tip in one loading cycle, we arrive at

$$\frac{dS}{dN} = \frac{W_c^{(1)}}{\sigma_{plf} \varepsilon_{fc} (1 - K_{I \max}^2 / K_{fc}^2)}. \quad (39)$$

Due to the occurrence of the two crack surfaces, i.e., upper and lower ($S = 2Ba$), the crack propagation formula can be written as

$$\frac{da}{dN} = \frac{\alpha W_c^{(1)}}{B \sigma_{plf} \varepsilon_{fc} (1 - K_{I \max}^2 / K_{fc}^2)}, \quad (40)$$

where:

K_{fc} – a cyclic fracture toughness,

$K_{I \max}$ – a maximum value of stress intensity factor,

$\alpha = 0.5$.

It seems that in order to estimate the influence of a loading cycle asymmetry R , it is proper to construct experimental kinetic fatigue fracture diagrams $da/dN-\Delta H$ in which the energetic parameter ΔH dependent on $W_c^{(1)}$ is equal to

$$\Delta H = \frac{W_c^{(1)}}{B(1 - K_{I\max}^2 / K_{fc}^2)}. \quad (41)$$

It should be noticed that the quantity $W_c^{(1)} = \partial W_c / \partial N$ (energy dissipation of plastic deformation before a crack tip in one loading cycle) in Equations (38)–(40) has a linear influence on output quantities occurring in these equations, i.e., dS/dN , da/dN and ΔH .

5. Comparison of theoretical and fitting results

A classical way of constructing the kinetic fatigue fracture diagrams (KFFD) in which both axes are dimensional, i.e., da/dN [m/cycle] and $K_{\max}(\Delta K)$ [MPa $\cdot\sqrt{m}$], is assumed. The middle part of these diagrams in double logarithmic axes is linear. A tangent m of this line (i.e., a slope of a straight line) has a dimension

$$m \left[\frac{\log m / \text{cycle}}{\log \text{MPa}\sqrt{m}} \right].$$

The verification of line factors values should keep their dimensions. Above all, the tangent a itself seems to be crucial. The values of line factors are shown in the Table.

Table. The values of line coefficients in double logarithmic axes

For ΔH	m	b
12HMF	0.86	– 8.83
18G2A	0.96	– 11.51
40H(200)	1.30	– 13.00
40H(450)	1.37	– 13.11
40H(700)	1.30	– 13.07

The notations in Table concern the rectilinear, middle part of kinetic fatigue fracture diagrams (KFFD) of the shape $y = mx + b$, where $y = \log da/dN$, $x = \log \Delta H$. From the theoretical basis (Equations (39) and (40)) it seems that $m = 1$, i.e.,

$$\frac{da}{dN} = \frac{\alpha}{\sigma_{plf} \varepsilon_{fc}} \Delta H. \quad (42)$$

In this formula $\alpha = 0.5$, then

$$\frac{da}{dN} = \frac{1}{2\sigma_{plf}\epsilon_{fc}} \Delta H^m. \quad (43)$$

Logarithm of Equation (42) has a form

$$\log\left(\frac{da}{dN}\right) = m \log \Delta H - \log(2\sigma_{plf}\epsilon_{fc}), \quad (44)$$

where m ought to be “one” (from the theory) [9]. As in Miner’s law, material does not want to generate “one”; for the materials tested the value of this factor changes in the range of 0.86–1.37 (the Table). It is known from theoretical considerations that a free term in double logarithmic axes is smaller than zero. In the tests performed by the author, all the values of a free term b are smaller than zero (the Table). Consequently, a qualitative agreement between theoretical and fitting models can be observed.

6. Experimental results

The two kinds of kinetic fatigue fracture diagrams have been drawn based on experimental data.

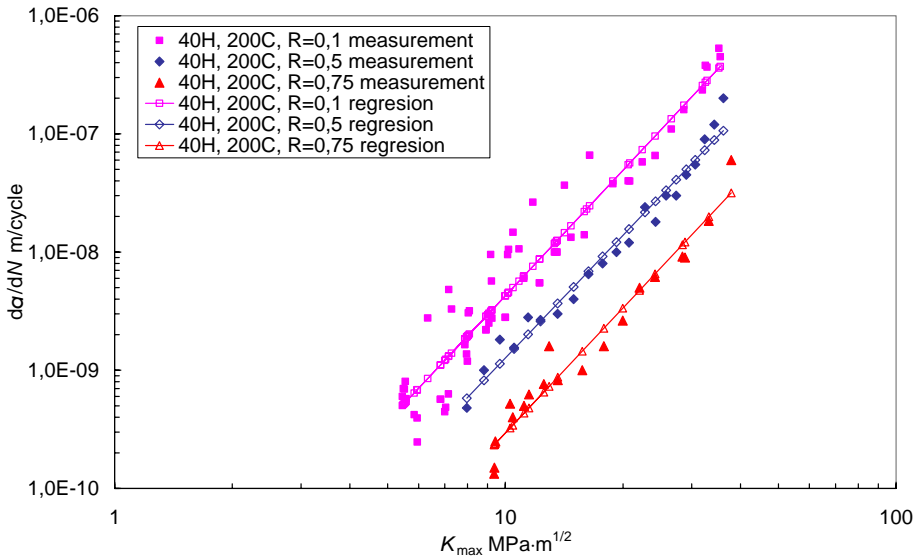


Fig. 6. Crack propagation rate da/dN versus stress intensity factor K_{max} for different asymmetry R ; 40H steel, heat treatment 200 °C

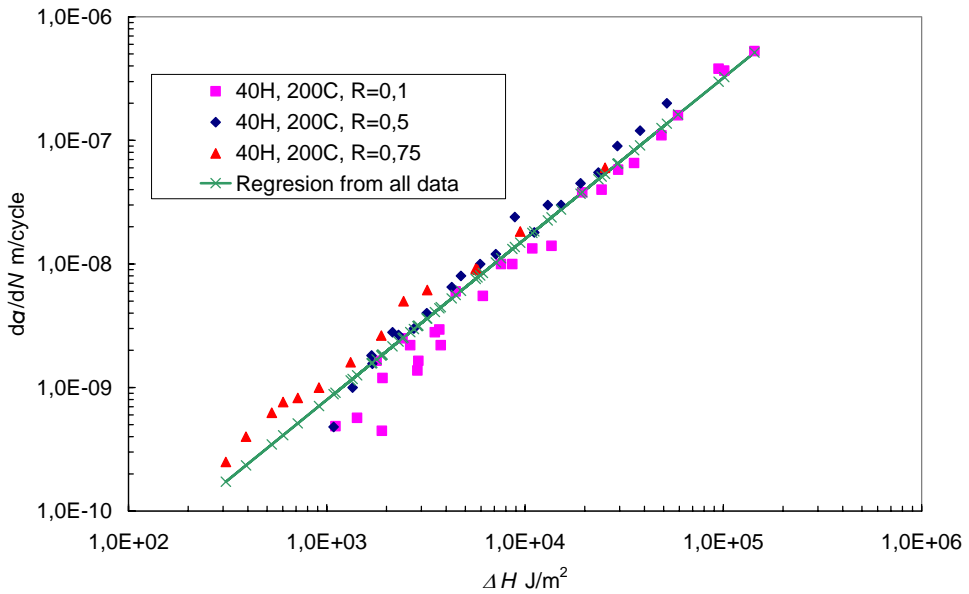


Fig. 7. Crack propagation rate da/dN versus parameter ΔH for different asymmetry R ; 40H steel, heat treatment 200 °C

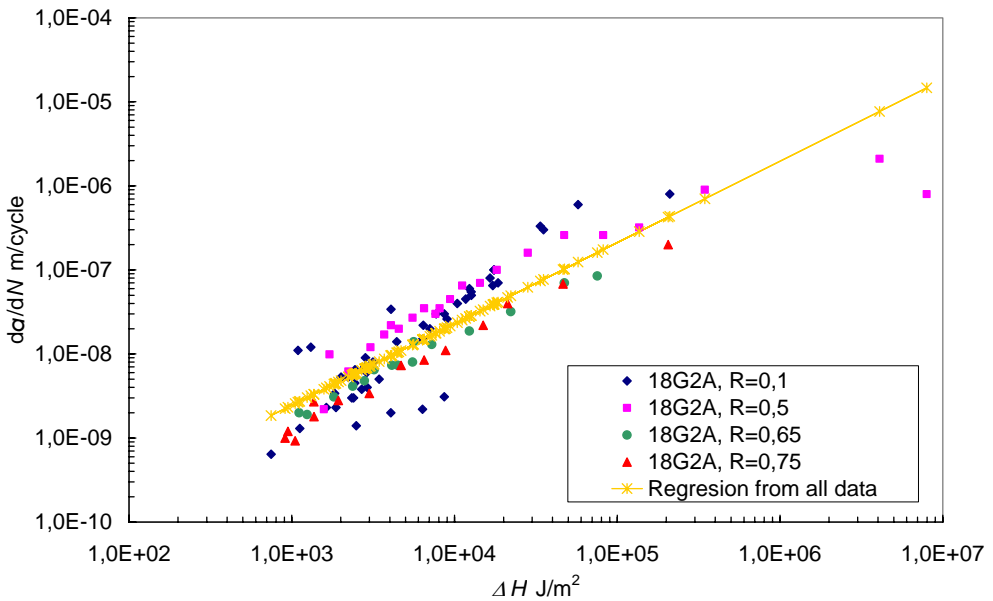


Fig. 8. Crack propagation rate da/dN versus parameter ΔH for different asymmetry R ; 18G2A steel

In the first diagram (classical), the stress intensity factor $K_{I\max}$ characterizing the intensity of deformation in the precracked zone before a crack tip was used for drawing the diagram. In the second and the third diagrams (the new ones), the energetic parameter ΔH corresponding to the searched energy dissipation of deformation $W_c^{(1)}$ was used.

The linear dependence of crack propagation rate da/dN on energy dissipation of plastic deformation before the crack tip for one loading cycle has been discussed with taking into consideration the consequences for fitting models in double logarithmic axes.

7. Conclusions

The energy criterion of fatigue crack propagation for the isotropic body has been presented. The analytical formula of a kinetic equation for fatigue crack propagation has been derived. The starting point is the energy balance resulting from the first principle of thermodynamics. A simplified method of solving the kinetic equation has been proposed. The results of this method have been confirmed in the case of an elliptic crack.

A new method of constructing kinetic fatigue fracture diagrams developed based on the measurement results of hysteresis loop area for the isotropic body with an internal flat crack under cyclic loading has been presented. For the experimental verification, the results of fatigue crack propagation studies for 18G2A and 40H steels have been utilized. The two kinds of kinetic fatigue fracture diagrams have been drawn based on the experimental data. The stress intensity factor $K_{I\max}$ characterizing the intensity of deformation in the precracked zone before a crack tip was used for constructing the first (classical) diagram. In the second and the third diagrams (the new ones), the energetic parameter ΔH corresponding to the searched energy dissipation of deformation $K_c^{(1)}$ was used.

In opposition to the $da/dN-K_{\max}$ diagrams, in the $da/dN-\Delta H$ diagrams obtained for a given range of the crack propagation rate, any difference in fracture kinetics has not been observed. This means that in contradistinction to the force factor K_{\max} , the energetic parameter ΔH describes synonymously the propagation rate of fatigue crack independently of a cycle asymmetry R . The linear dependence of the crack propagation rate da/dN on the energy dissipation of plastic deformation before the crack tip for one loading cycle has been discussed with taking into consideration the consequences for fitting models in double logarithmic axes.

References

- [1] Kocanda S., Kocanda D.: *Fatigue short cracks. Experimental analysis and analytical description*, German-Polish VI School on Fracture Mechanics, 2000, Publishing House of TU Dresden.

- [2] Neimitz A.: *Fracture Mechanics* (in Polish), WN PWN, Warsaw, 1998.
- [3] Rykaluk K.: *Pęknięcia w konstrukcjach stalowych* (in Polish), Dolnośląskie Wydawnictwo Edukacyjne, Wrocław, 2000.
- [4] Stosiak M., Szata M.: *Metodyka badań eksperymentalnych przy opisie pękania*, Górnictwo Odkrywkowe, 2003, Nr 2/3, s. 122–125.
- [5] Szata M., Frątczak R.: *Linearity and non-linearity effects in crack propagation model*, [in:] *Mechanika rujnuvannja materialiv i micnist' konstrukcij*, Pid red. V.V. Panasjuka. [L'viv, 22–26 cernvja, 2004]. L'viv: Nacjonal'naja akademija nauk Ukrainy, 2004, s. 57–63.
- [6] Szata M.: *Theoretical and experimental aspects of energy in mechanics of fatigue macro-crack propagation*, *Studia Geotechnica et Mechanica*, 1999, 3–4, 75–85.
- [7] Szata M.: *Modeling of fatigue crack growth using energy method* (in Polish), Publishing House of Wrocław University of Technology, Wrocław, 2002.
- [8] Szata M., Dąbrowska-Szata M.: *Fatigue fracture, crack initiation and description of propagation*, 20th Danubia-Adria Symposium on Experimental Methods in Solid Mechanics, 2003, Győr, Hungary, 228–229.
- [9] Szata M.: *Experimental data fitting in crack propagation model*, 22th Danubia-Adria Symposium on Experimental Methods in Solid Mechanics, 2005, Parma, Italy, 152–153.

Opis propagacji szczeliny zmęczeniowej – podejście teoretyczne i dokładność dopasowania do wyników pomiarów

Przedstawiono energetyczne kryterium propagacji szczeliny zmęczeniowej w ciele izotropowym. Wyprowadzono analityczną formułę równania kinetycznego rozwoju szczeliny zmęczeniowej. Aby uprościć rozwiązania, proponuje się zastosowanie metody powierzchni ekwiwalentnych. Podstawę tej metody stanowi hipoteza, że płaskie szczeliny z jednakowymi polami powierzchni, znajdujące się w jednorodnym polu naprężeń rozciągających, mają zbliżone wielkości obszarów ΔF przed frontem szczeliny (całej strefy plastycznej) oraz zbliżone wartości energii W_s i W_c . Z przedstawionych rozważań wynika, że otrzymane równanie kinetyczne wzrostu pola powierzchni szczeliny zmęczeniowej można rozwiązywać albo bezpośrednio, obliczając trwałość elementu N_g do chwili osiągnięcia przez rosnącą szczelinę krytycznej wielkości powierzchni S_* , albo z wykorzystaniem metody powierzchni ekwiwalentnych. Wyniki uzyskane dla szczeliny eliptycznej wskazują na przydatność metody powierzchni ekwiwalentnych.

Jednym z celów pracy było opracowanie metody eksperymentalnego budowania wykresów kinetycznych pękania zmęczeniowego. W metodzie tej wykorzystuje się pomiar wielkości pętli histerezy, energii odkształcenia próbki ze szczeliną w procesie cyklicznego obciążenia. Przedstawiono rozważania teoretyczne, w których wykorzystano podejście energetyczne, oparte na doświadczalnym wyznaczaniu pętli histerezy energii odkształcenia, odpowiadającej dyssypacji energii w jednym cyklu obciążenia. Wielkość wyznaczonej w ten sposób pochłoniętej energii jest bezpośrednio związana z intensywnością powrotnej plastycznej deformacji materiału przy wierzchołku szczeliny. Można więc oczekiwać jednoznacznej korelacji między dyssypacją energii a szybkością zmęczeniowego wzrostu szczeliny.

Przedstawiono również samo doświadczalne wyznaczanie pola pętli histerezy i wykorzystanie go zgodnie z rozważaniami teoretycznymi. Pokazano, że zastosowanie opisu energe-

tycznego, w którym wykorzystano uzyskaną eksperymentalnie pętlę histerezy energii odkształcenia materiału przy wierzchołku szczeliny, umożliwia jednoznaczny charakterystykę odporności na zmęczeniowy rozwój szczeliny niezależnie od asymetrii cyklu obciążania. W przeciwieństwie do wykresów $da/dN - \Delta K$, na wykresach $da/dN - \Delta S$, zbudowanych dla danego zakresu prędkości rozwoju pęknięcia szczeliny, nie zaobserwowano różnic w kinetyce pęknięcia. Oznacza to, że – w odróżnieniu od siłowego parametru ΔK – parametr energetyczny ΔS jednoznacznie opisuje prędkość zmęczeniowego rozwoju szczeliny niezależnie od współczynnika asymetrii cyklu R .

Effects of connection flexibility in steel-concrete composite beams due to live loads

CZ. MACHELSKI, R. TOCZKIEWICZ

Wrocław University of Technology, Wybrzeże Wyspiańskiego 27, 50-370 Wrocław

The paper describes the girders of bridges made of steel beams connected in a flexible way with a concrete deck slab. There are analyzed internal forces and displacements versus the changes in the connection degree that are due to variable cyclic loads occurring in bridges. The analysis of the problem is based on a classical parameter characterizing the connection flexibility C_z and supplied with the coefficients μ and β defined by authors. They allow the connection degree of a combined girder to be estimated. There are analyzed two solutions to the problem of partial interaction in composite steel and concrete girder: a linear one based on the solution of analytical form (differential equations) and a non-linear one based on mechanics of clearances. The latter solution accurately shows the work of connectors in bridge spans. The analysis is illustrated by numerical examples of a real composite bridge. The attention is focused on the diagrams showing various shapes of curves representing the coefficients μ and β .

Keywords: *composite beam, flexible connection, cyclic loads, clearances*

1. Introduction

A combined construction consists of elements made from various materials and of various physical properties cooperating with each other due to specially designed connectors. The elements of a composite construction were selected in such a way that their strength characteristics could be efficiently used, adequately to their position in the bridge construction [1]. A classical composite system, whose material properties are effectively used, is a girder made of a steel beam combined with a concrete (reinforced) slab in a single-span bridge. A girder made in this way has several advantages, e.g., structurally small height, economical use of steel, greater rigidity considering vertical and horizontal loads. Steel-concrete composite girders are also used in continuous multi-span bridges. In this case, the rigidity reduction associated with concrete cracking in the zone of negative moments [2] meaningfully influences the load carrying ability of the composite beams.

The joined elements made from the same materials, e.g., entirely made as concrete or timber ones but in various production cycles, form a composite girder, too. In this case, the different durability and physical properties of the elements being joined are important. Also in the case where the system is made of the same material but the elements are not joined in the way assuring accordance of deformations, we deal with a composite system, but the connection of the elements we treat as flexible one. In

Figure 1, there are given the examples of structures used in bridge engineering made from:

- a) steel and reinforced concrete;
- b) timber (glued) and reinforced concrete;
- c) prestressed concrete (or reinforced concrete) and reinforced concrete;
- d) steel I-bar profiles covered with concrete;
- e) concrete filled steel tubes (CFST).

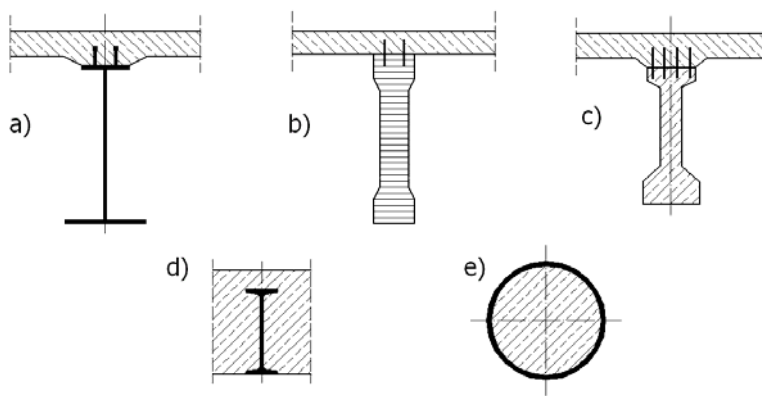


Fig. 1. The types of composite sections

The most often used in bridge structures are steel beams combined with concrete slab. Such girders have been used since the mid 1950's. Originally there had not been taken into account any kind of cooperation of both components of the section (the beam and the slab) as well as no elements assuring connection had been used either. Thus, a concrete deck slab had been used as a platform transferring the load to girders and the steel part was responsible for the load carrying ability. However, as the tests show [3], even if there are no special connectors joining both parts of the section, to a certain extent they worked with each other when bending. This occurs due to adhesive forces. After their destruction, the friction of the concrete against the steel favours mutual cooperation. Both effects may be treated as the ones which assure an additional margin of safety of the composite girder. However, they are not taken into account in bridge structures because of the difficulty in defining their values and random character of occurrence.

In the case of composite girders, the mechanical connectors are the elements being responsible for an effective cooperation of both parts (the steel beam and the concrete slab). They are characterized by a considerable deformability, especially meaningful in the case of welded stud shear connectors, at present commonly used in bridge constructions. A rather small flexural rigidity of the connectors and the lack of compatibility between the materials in the connection will cause clearances and will influence the beam and slab cooperation.

2. Flexibility of connection

◆ Parameters defining the flexibility of connection

The basic parameter defining flexibility of connection is the stiffness of a single connector c_z being defined as the ratio of the shear force T for the connector to the bridge plate displacement in relation to the steel beam flange δ (shear slip) caused by that force. It is expressed by the following equation

$$c_z = \frac{T}{\delta} \left[\frac{\text{kN}}{\text{mm}} \right]. \quad (1)$$

Stiffness of the connector c_z changes along with the load T . At the force up to 50–70% of the ultimate load breaking the connector, c_z can be treated as a constant (load-slip behaviour of stud shear connection is nearly linear). At increase in the load, yielding of the stud begins and the value of the slip grows. Thus, the temporary (tangential) stiffness of the connection c_z defined as the tangent of angle of inclination (at the considered moment) of the tangent to the curve $\delta(T)$ quickly decreases. Also the secant value of c_z decreases. This value is defined as a ratio of a force carried by the connector to the total plate displacement in relation to the beam. The displacement is measured at a given moment.

Because the total connection stiffness of the girder on length b results from n connectors of a stiffness c_z , we can use the following equation

$$C_z = \frac{n \cdot c_z}{b}. \quad (2)$$

In steel-concrete bridge girders the value of C_z usually changes along the beam, suitably to the value of vertical force. The shear force along the girder is described by

$$t = \frac{dT}{dx}, \quad (3)$$

thus, it is convenient to use the following equation

$$C_z = \frac{t}{\delta} \left[\frac{\text{kN}}{\text{m}} \frac{1}{\text{mm}} = \frac{\text{MN}}{\text{m}^2} \right]. \quad (4)$$

The value C_z is difficult to define accurately and, as it has been mentioned earlier, is influenced by several factors of a random character.

In analyses, a simplified bilinear model describing the function $\delta(t)$ is often considered (Figure 2). In this model it is assumed that the connectors work in a linear-elastic

range till the moment of a full yielding, and the value of the parameter C_z is constant, and the tangential stiffness is equal to the secant one. In the plastic range, the temporary stiffness equals zero (there is a slip increase at a constant load value) and the secant C_z changes. Below there is given an analysis in the linear-elastic range, i.e., if we assume a constant stiffness of the connection (force and shear slip change proportionally).

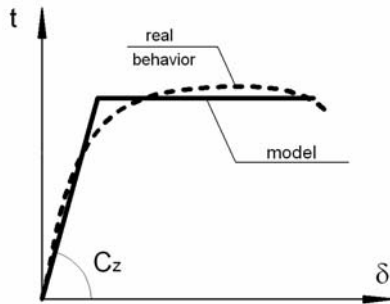


Fig. 2. Relation $\delta(t)$ for a flexible connection

The coefficient describing flexibility of the connection, which may be convenient in the analysis of the phenomenon considered, is expressed by

$$\beta = \frac{\varepsilon_{ca}}{\varepsilon_g} \quad (5)$$

and defined on the basis of the strain difference along the steel-concrete interface ε_{ca} related to the strain ε_g on the top flange of the steel girder [4]. In the case of a flexible connection, the principle of plane sections does not apply to the entire composite section and can be used only for the concrete and the steel parts separately. Along the interface there is a difference of strains ε_{ca} as an effect of the mutual shear slip of both parts of the girder.

The flexibility of connection essentially influences the distribution of internal forces in the beam as well as in the concrete slab. The coefficient defining the ratio of internal forces in a steel girder (axial force N_a and bending moment M_a) in the section can be defined as follows

$$\mu = \frac{aN_a}{M_a} \quad (6)$$

To receive an undimensional quantity of that parameter, the force N_a was multiplied by a constant value a , which is the distance between the centroids of both components of the composite section.

◆ Linear model

For the calculation of internal forces in the girder, the following general assumptions are accepted:

- the Bernoulli's plane sections principle is valid;
- there occurs a partial interaction resulting in a shear slip along the steel-concrete interface;
- there is no cracking of concrete bridge deck.

Strains, stresses and internal forces (bending moments and longitudinal forces) are identified according to the time at which the construction is subjected to a constant load. They can be:

- temporary at the moment of the load occurrence ($\tau = 0$);
- long term (final), when the rheological processes became stabilized.

Stresses and deformations due to those loads are considered to be independent and their effects sum up.

Geometrical characteristics of a cross-section. The geometry of the cross-section of the girder: section area (A_c and A_a), moments of inertia (I_c and I_a) are referred to the centroids of both components (the steel beam and the concrete slab) (Figure 3). In the values of section area A_c and the moment of inertia I_c , longitudinal reinforcement of the deck slab can be taken into account.

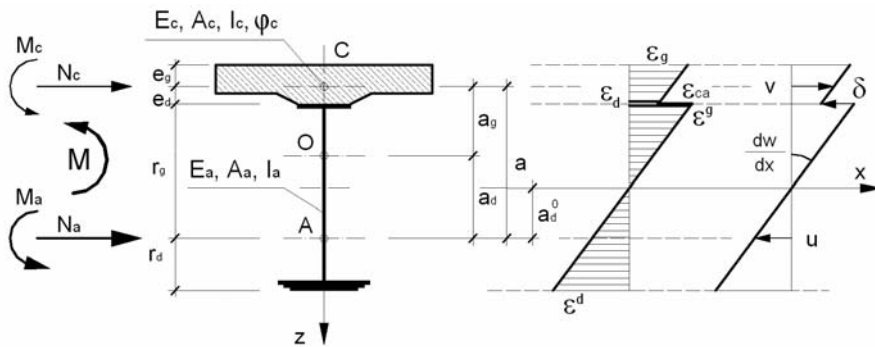


Fig. 3. Notations of the internal forces, geometrical and material characteristics in the composite cross-section. Unit strains and displacements in the cross-section of the girder

Location of centroids of those elements is defined by the vertical dimensions: r_g and r_d for the beam and e_g and e_d for the slab. The distance between the centroids

$$a = r_g + e_d \quad (7)$$

is a constant value, unchangeable with time and independent of the connection flexibility and the external forces. Geometrical characteristics of the composite section are usually related to the beam parameters (in steel bridges it is a rule) by using a coefficient

$$n = \frac{E_a}{E_c}. \quad (8)$$

In the case of short-term loads, the value of n is constant.

The variable parameter of the composite beam that changes with time is the creep coefficient of concrete of the slab φ_c . In the case of long-term loads, the geometrical characteristics of the cross-section are changeable with time (in the function of the load time and the moment of observation). For the long-term loads, in terms of the modified theory of ageing of the concrete according to Trost [5], the value of the modulus of elasticity is reduced according to the principle given by the equation

$$E_{c\varphi} = \frac{E_c}{1 + \rho \cdot \varphi_c}. \quad (9)$$

The coefficient n_φ that reduces characteristics of both materials of the structure to one material (steel) is expressed by

$$n_\varphi = \frac{E_a}{E_c}(1 + \rho\varphi_c), \quad (10)$$

where ρ is Trost's coefficient [5].

The position of the centroid of the reduced cross-section (Figure 3) can be calculated from the equations

$$a_d = \frac{A_{c\varphi}}{A_a + A_{c\varphi}} a, \quad (11)$$

$$a_g = \frac{A_a}{A_{c\varphi}} a_d = \frac{A_a}{A_a + A_{c\varphi}} a, \quad (12)$$

where

$$A_{c\varphi} = \frac{A_c}{n_\varphi}. \quad (13)$$

The process of changing the centroid position is a function of time, or strictly speaking, it results from the creeping process. The influence of the creeping on the centroid position of the composite girder is significant [6].

Internal forces and strain relations. In the case analyzed, it is convenient to separate the section force resultants into two systems, i.e., the slab and the beam. Such a division is justified by a time-invariable position of the centroids of the subsystems of a composite section. Internal forces related to the components of the cross-section shown in Figure 3 are statically equivalent to the moment M , since they satisfy the conditions of the statical balance of:

- the sum of the force projections on a horizontal axis

$$N_a + N_c = 0, \quad (14)$$

- the sum of the moments in relation to the centroid of the composite cross-section O

$$M_c - N_c \cdot a_g + M_a + N_a \cdot a_d = M. \quad (15)$$

The internal forces in the slab and the beam cause unit strains along the steel-concrete interface (for short-term loads or at an initial moment) on the top flange of the beam

$$\varepsilon^g = \frac{N_a}{E_a A_a} - \frac{M_a r_g}{E_a I_a} \quad (16)$$

and on the bottom edge of the slab

$$\varepsilon_d = \frac{N_c}{E_c A_c} + \frac{M_c e_d}{E_c I_c}. \quad (17)$$

The strain difference along the steel-concrete interface (described as in Figure 3) combines the change of the shear forces in the connectors t along the beam length with the stiffness of the connection by the equation

$$\varepsilon_{ca} = \varepsilon^g - \varepsilon_d = \frac{1}{C_z} \frac{dt}{dx}. \quad (18)$$

The consistency condition of the curvatures of the girder elements (for a long-term load) is given by

$$\frac{M}{E_a I_x} = \frac{M_a}{E_a I_a} = \frac{M_c}{E_c I_c} (1 + \rho \varphi_c) \quad (19)$$

and after the elasticity modulus of the concrete has been corrected according to (10) we have

$$\frac{M}{I_x} = \frac{M_a}{I_a} = \frac{M_c}{I_{c\varphi}}, \quad (20)$$

where the moment of inertia of the slab is expressed by

$$I_{c\varphi} = \frac{I_c}{n_\varphi}. \quad (21)$$

The moment of inertia of the girder, considering the connection coefficients, can be expressed by

$$I_x = I_a + I_{c\varphi} + aa_d A_a \frac{a - \beta \cdot r_g}{a - \beta \cdot a_d} \quad (22)$$

or

$$I_x = (1 + \mu)I_a + I_{c\varphi}. \quad (23)$$

The relationship between C_z and β is defined by the following equation used for calculating the strain discontinuity along the steel–concrete interface

$$\varepsilon_{ca} = \beta \varepsilon^g = \beta \left(\frac{N_a}{E_a A_a} - \frac{M_a r_g}{E_a I_a} \right) = \frac{1}{C_z} \frac{dt}{dx}. \quad (24)$$

The relationships between β and μ depend exclusively on the geometrical parameters of the combined elements

$$\mu = \frac{a_d(a - \beta \cdot r_g)a \cdot A_a}{(a - \beta \cdot a_d)I_a}. \quad (25)$$

The relationships between C_z and the connection coefficients β and μ are unclear [4].

Equations of equilibrium of internal forces. The shear force t generated due to the changes of an axial force in the beam N_a (and in the slab N_c) is expressed by

$$t = \frac{dN_a}{dx}. \quad (26)$$

When the stiffness of the connection $C_z(x)$ changes along the beam, we have

$$\frac{dt}{dx} = \frac{d^2 N_a}{dx^2} - \frac{1}{C_z} \frac{dN_a}{dx} \frac{dC_z}{dx}. \quad (27)$$

Thus the relationship between the axial force N_a and the bending moment M [4]

$$\frac{E_a I_a + I_{c\phi}}{C_z} \frac{1}{a^2} \left(\frac{d^2 N_a}{dx^2} - \frac{1}{C_z} \frac{dN_a}{dx} \frac{dC_z}{dx} \right) - \frac{I_x}{a \cdot a_d A_a} N_a + M = 0. \quad (28)$$

Equation (28) is the basis of the solution of the composite girder with flexible connectors that is subjected to the bending moment $M(x)$. Based on N_a we can calculate M_a using (15) and then the forces applied to the slab (given in Figure 4) using Equations (20) and (14).

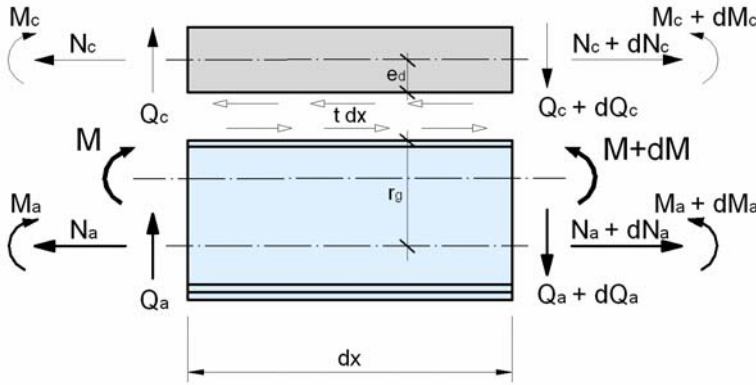


Fig. 4. Internal forces in a differential element of a composite girder

The division of the vertical force Q into the forces Q_c and Q_a is proportional to the division of M into M_c and M_a , which results from relation (20) and the differential equation

$$Q_i = \frac{dM_i}{dx}. \quad (29)$$

Displacements. The internal forces calculated above can be used to define the displacements u , v and w of the beam and slab given in Figure 3. Taking into consideration unit strains being a result of the axial forces, we obtain

$$\frac{du}{dx} = \frac{N_a}{E_a A_a} \quad (30)$$

and

$$\frac{dv}{dx} = \frac{N_c}{E_a A_{c\varphi}} \quad (31)$$

and from the equation of curvature (20) we have

$$\frac{d^2w}{dx^2} = -\frac{M_a}{E_a I_a}. \quad (32)$$

The shear force along the steel–concrete interface t (Figure 4) combines all the displacement constituents and the connection stiffness

$$t = C_z \delta = C_z \left(u - v - a \frac{dw}{dx} \right) \quad (33)$$

and can be used for defining the boundary conditions of displacements.

3. Multiple loads

◆ Shear slip changes

The behaviour of the connection depends on the kind of load imposed on the construction. In bridges, it often happens that variable loads of a cyclic character are predominant loads carried by connectors. That is why their action seems to be especially important and essential in the analysis of the rigidity and fatigue life of a connection.

Some of the first fatigue tests on stud shear connectors were done in the 1960's in the USA [7]. The attention had been focused on the shear strength of the connectors, and relations between the number of the load cycles and the values of the slip increments in connection were not properly considered. First relationships between the number of load cycles, the slip growth and the range of the force were established in the 1970's [8] and since then an intense development of researches focused on that problem [9, 10, 11] has taken place. Parallely fatigue tests have been carried out on composite girders made in natural size [12]. The most essential conclusions, from the point of view of the analysis of the partial interaction of girders, based on the researches, are as follows:

- load carrying capacity of the connection subjected to cyclic loads is smaller than the load carrying capacity under static load;
- the stiffness of the connection reduces with succeeding cycles of the load;
- the range of the force changes influences the stiffness decrease;
- along with the succeeding load cycles the slip increases;

- a decrease in the stiffness of the connection occurs even at relatively small loads which do not exceed 40% of the load carrying capacity of connectors.

In the case of steel-concrete composite beams, the attention should be paid to the slackening in the connection caused by the cyclic loads. For the long-span bridge girders, the values of slip along the interface of both components forming a composite section may be considerable and may lead to local inelastic deformations and stiffness reduction of the connection. When in the succeeding cycles of loading the slip increments are reduced, the slip is stabilized and the beam can be considered to shaken down to a stable condition. But if the slip increments are constant or increase with each cycle of loading, the beam rigidity reduces and the deflection increases which may lead to the construction failure.

The phenomenon of a cyclic slip increment in the connection of steel-concrete composite girders was the subject of many works [8, 13, 14, 15]. Often the phenomenon occurred under relatively small loads [16], not exceeding the exploitation values. The experiments were carried out both for unidirectional loads and for alternating loads, the latter being much more disadvantageous for the connection durability [17]. Under typical loads the connectors are not affected in this way. Alternating loads occur during earthquake excitations. In the case of long girders, the most efforted connectors (in the vicinity of the supports) may be subjected to plastic deformations. After the load removal, the structure working elastically will tend to the initial geometrical configuration with no slip along the steel-concrete interface. Due to this effect the shear forces of the opposite sign to that normally occurring will be generated in those connectors [17].

The influence of cyclic loads on the interface shear slip value is established on the basis of the empirical dependencies obtained from experimental research. Most often they describe the slip growth δ per cycle as a function of the range of the load, which is defined as a ratio of the cyclic force T acting on the connector to its static shear strength T_u . The relation obtained based on the research described in [15] is in the example presented below

$$\delta = 10^{(3.91 \cdot \frac{T}{T_u} - 4.71)} \text{ [mm/cycle]}. \quad (34)$$

Another relation takes into account the influence of the connector's diameter d expressed in equation [14]

$$\frac{\delta}{d} = 1.7 \cdot 10^{-5} \left(\frac{T}{T_u} \right)^{4.55} \text{ [mm/cycle]}. \quad (35)$$

In Figure 5, there are presented the results of research reported in [18] as well as the diagrams of empirical relationships characterizing analyzed phenomenon. It can be

seen that in most cases the slopes of the curves describing the relationship between the slip increment and the effort of the stud are similar. Also the values of the slip growth per cycle are similar. Considerably different results given in [15] are described by relation (34). The cause is that the results have been obtained from the tests on the connectors of various geometrical parameters (length, diameter) for various classes of concrete and ranges of load change in cycles. Therefore it is difficult to compare them directly. Till now there have not been given unique relationships describing the phenomenon discussed.

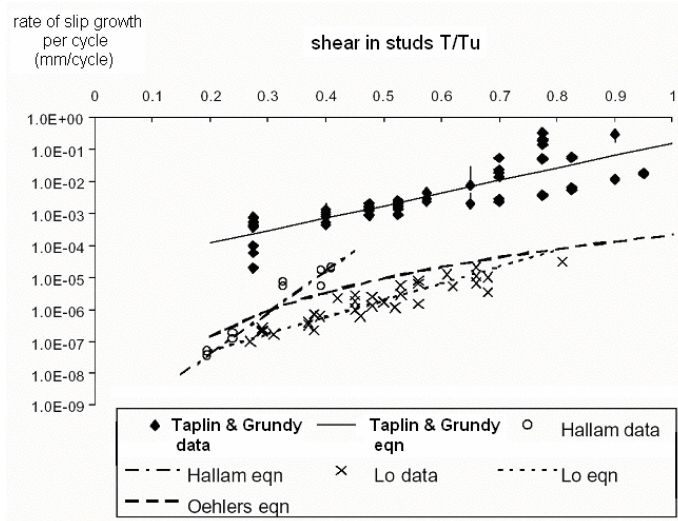


Fig. 5. Relationships between the range of the forces in the connector and rate of slip growth per load cycle [18]

◆ Nonlinear models of elastic connection with the clearance

The phenomenon of the connection slackening in a composite bridge girder caused by the changes in the slip value can be described by mechanics of the systems with clearances. Clearances appear in the connection of construction elements most often as a result of cyclic exploitation loads. This process may considerably influence the mechanics of bridge construction. Another type of clearances are inaccuracies in element connections (among others seen in bolt connections). They may occur in new bridges and often with time they may get filled because of the influence of loads. This is caused by the adjustment of a new construction to working conditions. Such a phenomenon can be clearly observed in soil-steel bridges [19].

The clearance formation means the displacement increase and simultaneously no force is overtaken by the connection or this force value is small compared to its maximum value. Only when the clearance was filled, did it begin to work effectively

and in a linear-elastic range. The displacement increment is proportional to the force increment. In a bilinear model of the system with the clearance of one degree of freedom, it is assumed that the force has a zero value in the connection P_0 until the filling of the clearance (at the displacement equal to δ_0) (Figure 6a). Then the system works as a linear-elastic one (the displacement δ_k complies with the force P_k). This model is to some extent a simplification of the problem, because in real conditions such a situation may not appear because of the friction occurring in the connection. Then when describing the phenomenon, we can use a model where there is a considerable displacement increase with an initially small increase of the force (Figure 6b). Only when the boundary value δ_0 of the displacement was exceeded (at the load P_0) did the connection fully overtake the force. In Figure 6c, there is shown a clearance model considering rheological effects. In such a case, after the load P_k is achieved, the delayed deformation δ_r succeeds [20].

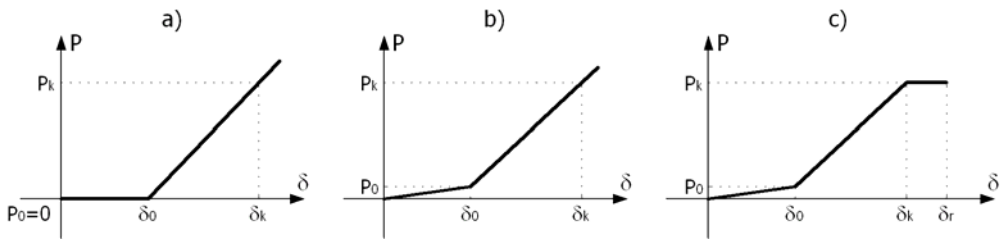


Fig. 6. The models of structures with clearances

These models describe the behaviour of the construction of one degree of freedom, while real structures are discrete systems (with several clearances). Therefore filling of each of them causes a gradual change in the way of working of the whole construction. The load level is also important as it decides which of the clearances may be filled or stay unfilled.

◆ Clearances in composite girders

The connectors in bridge composite construction are repeatedly subjected to cyclic forces during exploitation (the vehicle traffic or railway stock loads). Each succeeding cycle of loading may cause the appearance of the zones with damages in the connection (local reaction between the connector and the concrete becomes the source of the connection degradation). Thereby some clearances appear, so there occurs a local development of the zones of reduced stiffness C_z which decrease a total rigidity of the composite system. There takes place a redistribution of forces from the connectors of a greater degree of degradation to the studs of greater stiffness. The process evolves with each subsequent cycle of loading changing the strain distribution, internal forces and displacements along the girder.

In a new connection loaded for the first time (the number of cycles $N = 0$), the initial value c_z^0 is constant (Figure 7). There occur proportional increments of the shear slip δ^0 and the force T^0 in each of the considered levels of the connection effort. This can be described by the equation

$$c_z^0 = \frac{T_A^0}{\delta_A^0} = \frac{T_B^0}{\delta_B^0} = \text{const.} \quad (36)$$

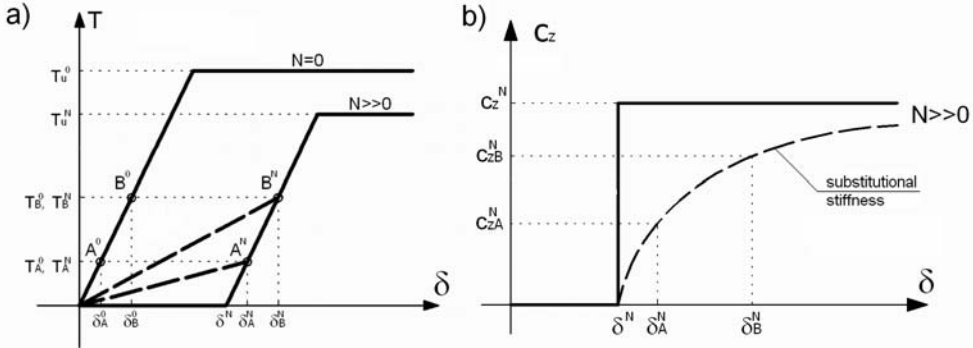


Fig. 7. Work model and the stiffness of a connector with clearance

In the connector subjected to the cyclic loads, there is formed a clearance δ^N increasing along with the succeeding load cycles ($N \gg 0$). The shear force is transferred between both parts of the composite section if the boundary value of the slip δ^N is exceeded (it depends on the number of cycles). At that value the stud is involved in work. The stiffness of the connector is a non-linear quantity which changes from the zero value c_z^0 to the final value $c_z^N = \text{const}$ (defined from the curve $\delta = f(T)$ inclination like in Figure 7). It can be assumed [18] that the rigidity after the clearance has been filled is equal to the initial stiffness of the system subjected to the first loading.

In order to determine the changed (reduced) value of c_z^N , we can make use of a substitutional stiffness defined as a tangent of an angle of inclination of the straight line connecting the initial point of loading with a point on the load path (Figure 7) equivalent to a given value of the force. The stiffness defined in this way depends on the connector's effort in the loading cycle considered (T_A^N , T_B^N) as well as on the variable (dependent on the number of loading cycles N) displacement value (clearance in the connection) δ^N :

$$c_{zA}^N = \frac{T_A^N}{\delta_A^N}, \quad (37)$$

$$c_{zB}^N = \frac{T_B^N}{\delta_B^N}, \quad (38)$$

thus $c_{zA}^N \neq c_{zB}^N$.

The above remarks apply to the systems with one degree of freedom (single connector). In real bridge construction, the beam and the slab are connected by several elements. Each of them is characterized by a different degree of effort associated with the range of shear force. It should be expected that the reduction of the total stiffness of the connection C_z , resulting from the clearances formation, will take place in various degrees along the length of the beam. The analysis of the complex systems may be difficult. Therefore, the most often used are those numerical applications based on iterative procedures.

4. Comparative analysis

◆ Linear model

The analysis concerns a single-span road composite bridge girder of the theoretical span length $L = 28.0$ m, made of a steel beam of a variable stiffness along its length (a thicker bottom flange in the central part), combined with the slab made of concrete B30. The geometrical parameters and physical properties of materials of the girder are given in Table 1. The girder of the bridge was designed for live loads of class A [21].

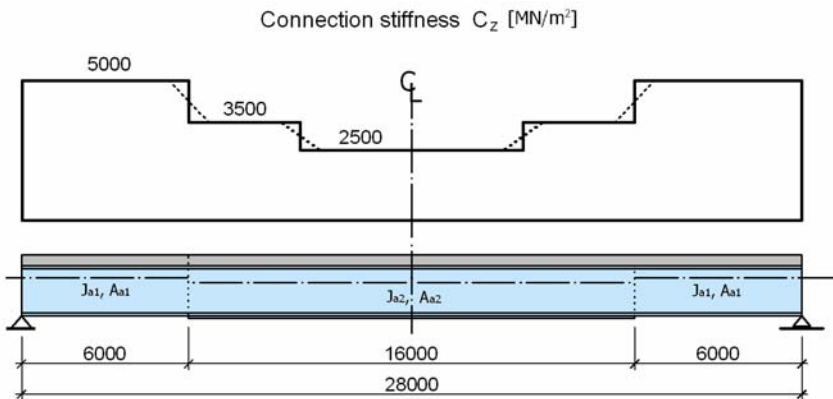


Fig. 8. Distribution of the connection stiffness $C_z(x)$ along the length of the girder

For the calculated shear force there were designed the stud connectors of a diameter $d = 12$ mm and height $h = 10d$. The characteristic shear strength of each of them [22] is $P^{ch} = 35.4$ kN, and the shear stiffness, taken according to [23], is equal to $c_z = 200$ MN/m. The number of connectors (the degree of stiffness of connection C_z) was

adjusted to the value of the shear force that changed along the girder (Figure 8). This force was symmetrical to the center of the span (Table 2). The loads in the composite beam cause a maximum bending moment $M = 5.05$ MNm in the center of the girder's span.

Table 1. Geometrical parameters of the analyzed girder

Girder's elements	A_c, A_a [m ²]	I_c, I_a [m ⁴]	e_g, r_g [m]	e_d, r_d [m]	E_c, E_a [MN/m ²]
Deck slab	0.5826	0.0020	0.095	0.145	32600
Beam with thinner bottom flange (1)	0.0448	0.0191	0.990	0.640	205000
Beam with thicker bottom flange (2)	0.0550	0.0227	1.108	0.542	

Table 2. Stiffness of the connection

Range [m]	C_z [MN/m ²]	Number of connectors / m
$0 < x < 6$	5000	24
$6 < x < 10$	3500	16
$10 < x < 14$	2500	12

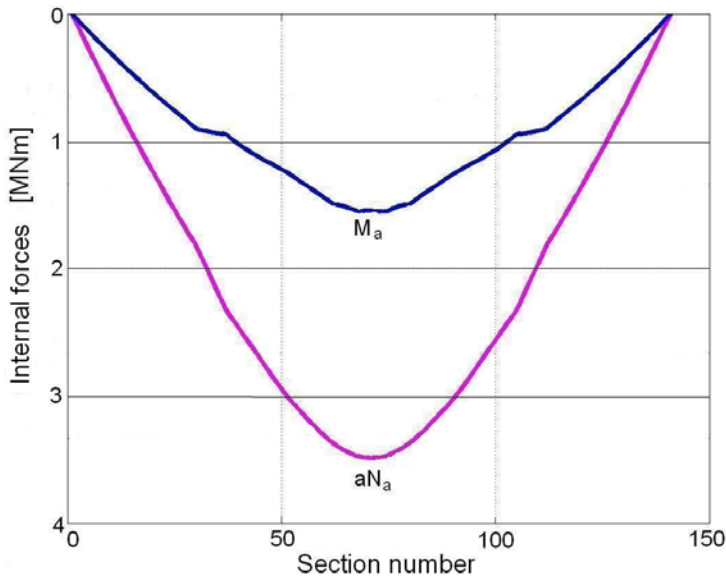


Fig. 9. Internal forces $M_a(x)$ and $aN_a(x)$ in a steel beam

The beam was divided into 140 elements, taking into account transitory segments of the connection stiffness change C_z as well as the flexural and axial stiffness of the steel beam. On the x -axis there are given the numbers of sections (0 and 141 are the

supportive sections). In Figures 9–12, there is presented a variation in both internal forces and connection coefficients along the girder, obtained on the basis of (28) and the authors' own numerical application [4].

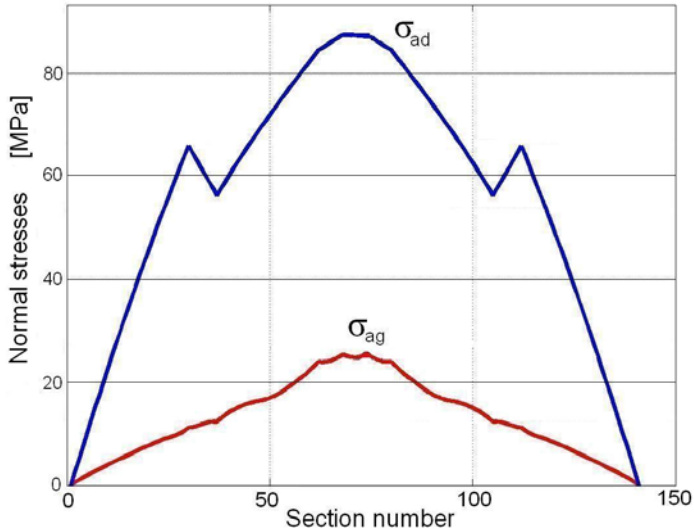


Fig. 10. Normal stresses $\sigma_{ag}(x)$, $\sigma_{ad}(x)$ on the flanges of a steel beam

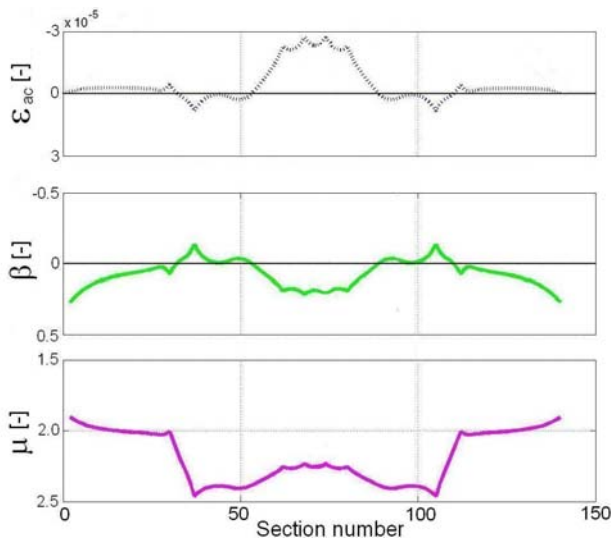


Fig. 11. Strain difference along the steel–concrete interface $\varepsilon_{ac}(x)$ and the values of the coefficients $\mu(x)$ and $\beta(x)$

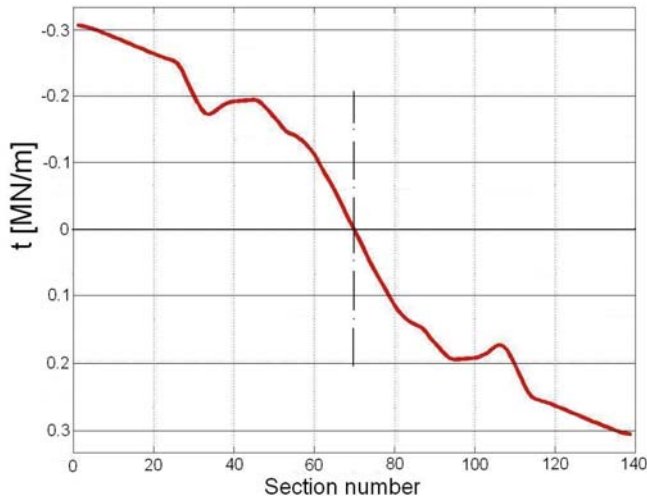


Fig. 12. Shear force $t(x)$

The analysis presented becomes more complicated in the case of multi-span continuous bridges. In such a case, we deal with cracking of concrete in the negative moment regions, in the vicinity of supports. In the case of long-term loads, not only the stress redistribution in cross-sections, but also the redistribution of internal forces along the girder should be taken into account. The effect of connection flexibility also becomes more complex. The slip along the steel–concrete interface may appear either in positive and negative moment regions. Behaviour of continuous composite beams with flexible connection was described in [24, 25, 26]. This problem will be the subject of authors' further researches and numerical analyses.

◆ Effects of multiple loads

The analysis concerns the steel-concrete composite girder of the geometric and material characteristics as these in Table 1. A tractor of K800 class [21] is the load of the bridge. It generates a bending moment $M = 2.87$ MNm in the middle of the girder. We assume that the load is of a cyclic character. The connection is assured by stud connectors taken earlier. For the sake of simplicity we assume a uniform spacing of studs along the length of the girder (24 connectors per meter), which means a constant stiffness of the connection $C_z = 5000$ MN/m².

The beam divided into 24 elements was subjected to a multiple load resulting in the shear slip increment in succeeding cycles according to Equation (35). Thus a total stiffness of the connection $C_z(x)$ was reduced. Figures 13–16 present the stiffness reduction C_z and the resulting changes of the internal forces and the connection coefficients in the chosen section of the girder, depending on of the number of loading cycles. The results were obtained using a numerical iterative procedure.

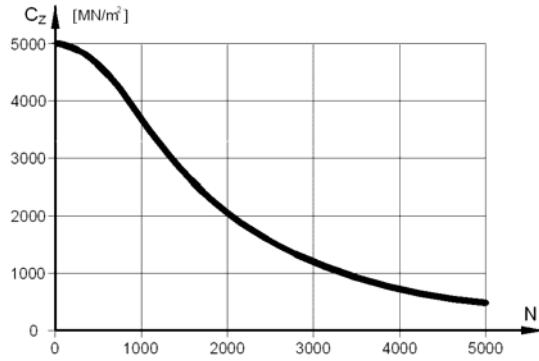


Fig. 13. Change of connection stiffness $C_z(N)$ in the beam section $x = L/3$

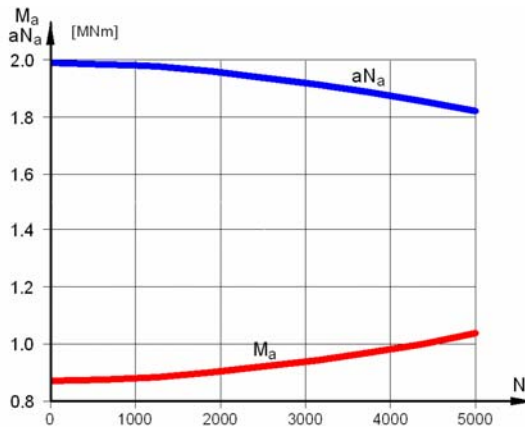


Fig. 14. Changes of internal forces $M_a(N)$ and $aN_a(N)$ in the middle of beam

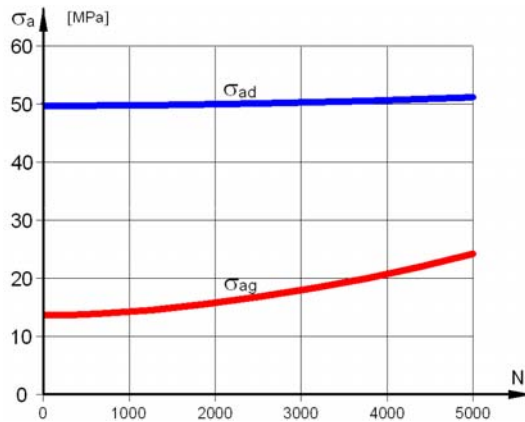


Fig. 15. Changes of normal stresses $\sigma_{ag}(N)$, $\sigma_{ad}(N)$ in the middle of beam

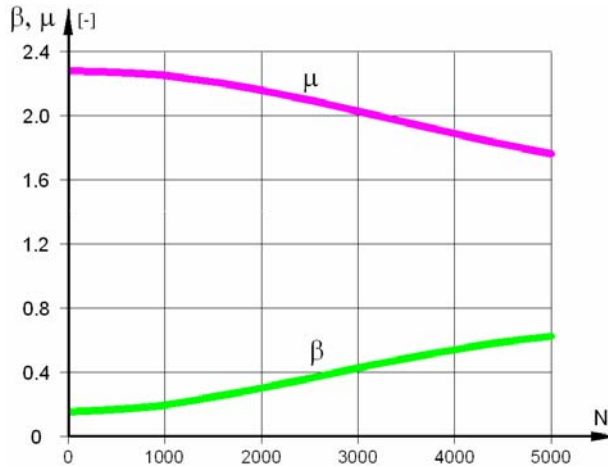


Fig. 16. Changes of the coefficients $\mu(N)$ and $\beta(N)$ in the middle of beam

5. Summary

In the paper, the problem of a partial interaction in steel-concrete composite beams connected by flexible stud shear connectors is discussed. The analysis of the problem is presented with use of a classical parameter characterising flexibility of the connection C_z and the authors' own coefficients μ and β . They allow the estimation of the interaction degree in relation to the composite girder of a full connection. There are proposed two kinds of solutions to the problem of the composite girder's elements interaction: a linear one based on the analytical solution in the form of differential equations and a non-linear one presented in terms of the mechanics of clearances. Special attention is focused on the cyclic loads predominating in bridge construction and their influence on the change in a connection stiffness of the girder. The analysis of the influence of the connection parameter function $C_z(x)$ on the distributions of internal forces and strains in a cross-section of the girder is presented. The results obtained using the coefficients μ and β allows us to formulate the following conclusions:

- The functions of the connection parameter $C_z(x)$ and the moment $M(x)$ affect considerably the distributions of internal forces in the beam and the slab. They also have

a decisive influence on a characteristic curve of the stress in the cross-section of the girder.

- The connection coefficients μ and β give exclusively information about the characteristics of the strains at the height of the girder.

- In general, establishing the relationships between $C_z(x)$ and $M(x)$, and $\mu(x)$ and $\beta(x)$ is impossible. Thus, the classical (design) analysis of the distribution of internal forces in the cross-section of a flexibly connected girder, selected from the structure, does not show the strain of a steel beam flexibly connected with a concrete bridge deck.

The results of the analysis in which cyclic exploitation loads are taken into account allow us to define the changes in the connection stiffness of the girder in the function of the load cycle number. The reduction of the parameter C_z occurring in this process influences significantly the distribution of internal forces as well as the girder's strain. The values of the coefficients μ and β change as well. The relationships describing this phenomenon affect the results obtained. So far the phenomenon has not been clearly formulated and described in terms of multiple and long-term loads.

The analysis of rheological effects of the steel and concrete composite beam with partial interaction [27] is a different problem. In this paper, the problem was formulated according to the modified Trost's theory [5] of concrete ageing.

References

- [1] Furtak K.: *Mosty zespolone*, Wydawnictwo Naukowe PWN, Warszawa–Kraków, 1999.
- [2] Madaj A.: *Doraźna nośność i sztywność na zginanie zespolonych belek stalowo-betonowych*, Wydawnictwo Politechniki Poznańskiej, Poznań, 2005.
- [3] Karlikowski J., Wołowicki W.: *The experimental-analytical assessment of the carrying capacity of the quasi composite multibeam bridge*, Proceedings of the 4th International Conference on Safety of Bridge Structures, Wrocław, 1992, pp. 435–442.
- [4] Machelski Cz., Toczkiwicz R.: *Podatność połączenia stalowego dźwigara z płytą betonową w mostach zespolonych*, Drogi i Mosty, 2005, nr 3, s. 37–76.
- [5] Trost H.: *Zur Berechnung von Stahlverbundträgern in Gebrauchszustand auf Grund neuerer Erkenntnisse des viskoelastischen Verhaltens des Betons*, Der Stahlbau, 1968, 11.
- [6] Machelski Cz.: *Probability of cracking of composite prestressed concrete bridges*, Archives of Civil and Mechanical Engineering, 2003, Vol. III, No. 1, pp. 77–93.
- [7] Slutter R. G., Fisher J. W.: *Fatigue strength of shear connectors*, Hwy. Res. Rec. 147, Transp. Res. Board, Washington, D.C., 1966.
- [8] Hallam M. W.: *The behavior of stud shear connectors under repeated loading*, University of Sydney School of Civil Engineering, Research Report R 281, August 1976.
- [9] Gattesco N., Giuriani E.: *Experimental study on stud shear connectors subjected to cyclic loading*, Journal of Constructional Steel Research, 1996, Vol. 38, No. 1, pp. 1–21.
- [10] Nakajima A., Saiki I., Kokai M., Doi K., Takabayashi Y., Ooe H.: *Cyclic shear force–slip behavior of studs under alternating and pulsating load condition*, Engineering Structures, 2003, Vol. 25, pp. 537–545.
- [11] Civjan S. A., Singh P.: *Behavior of shear studs subjected to fully reversed cyclic loading*, Journal of Structural Engineering, 2003, Vol. 129, No. 11, pp. 1466–1474.
- [12] Yen J. Y. R., Lin Y., Lai M. T.: *Composite beams subjected to static and fatigue loads*, Journal of Structural Engineering, 1997, Vol. 123, No. 6, pp. 765–771.
- [13] Hawkins N.M., Mitchell D.: *Seismic response of composite shear connections*, Journal of Structural Engineering ASCE, September 1984, Vol. 110, No. 9, pp. 2120–2136.
- [14] Oehlers D.J., Coughlan C.G.: *The shear stiffness of stud shear connections in composite beams*, Journal of Constructional Steel Research, 1986, 6, pp. 273–284.

- [15] Taplin G., Grundy P.: *Incremental slip of stud shear connectors under repeated loading*, Proceedings of the International Conference on Composite Construction – Conventional and Innovative, Innsbruck, 1997, pp. 145–150.
- [16] An L., Cederwall K.: *Push out tests on studs in high strength and normal strength concrete*, Journal of Constructional Steel Research, 1996, Vol. 36, pp. 15–29.
- [17] Gattesco N., Giuriani E., Gubana A.: *Low-cycle fatigue test on stud shear connectors*, Journal of Structural Engineering, 1997, Vol. 123, No. 2, pp. 145–150.
- [18] Taplin G., Grundy P.: *Steel-concrete composite beams under repeated load*, Department of Civil Engineering, Monash University, Australia.
- [19] Machelski Cz., Antoniszyn G.: *Influence of live loads on the soil-steel bridges*, Studia Geotechnica et Mechanica, 2004, No. 3–4, pp. 91–110.
- [20] Machelski Cz.: *Effort of Bridge Structures with Clearances of Joints*, International Bridge Conference Warsaw '94, 20–22 June, 1994, pp. 69–75.
- [21] PN-85/S-10030. *Obiekty mostowe. Obciążenia*.
- [22] Eurocode No. 4: *Design of Composite Steel and Concrete Structures*. Part 2: *Bridges*.
- [23] Łagoda M.: *Stany graniczne podatności łączników w mostowych konstrukcjach zespolonych*, Raport PRE-52/81 Instytutu Inżynierii Lądowej Politechniki Wrocławskiej. Praca doktorska.
- [24] Nie J., Fan J., Cai C.S.: *Stiffness and deflection of steel-concrete composite beams under negative bending*, Journal of Structural Engineering, 2004, Vol. 130, No. 11, pp. 1842–1851.
- [25] Fabbrocino G., Manfredi G., Cosenza E.: *Analysis of continuous beams including partial interaction and bond*, Journal of Structural Engineering, 2000, Vol. 126, No. 11, pp. 1288–1294.
- [26] Virtuoso F., Vieira R.: *Time dependent behaviour of continuous composite beams with flexible connection*, Journal of Constructional Steel Research, 2004, Vol. 60, pp. 451–463.
- [27] Ryż K.: *Wpływ stopnia współpracy płyty z dźwigarem na efekty reologiczne w zespolonych przęsłach mostowych typu beton-stal*, Konferencja Naukowo-Techniczna *Trwałość i Przydatność Użytkowa Konstrukcji Mostowych*, Poznań, 1989, s. 307–315.

Efekty podatności zespolenia w belkach stalowych z płytą betonową pod obciążeniem zmiennym

Praca dotyczy dźwigarów głównych mostów wykonanych z belek stalowych zespolonych w sposób podatny z betonową płytą pomostową. Analizie poddano siły wewnętrzne i przemieszczenia w funkcji zmian podatności zespolenia wynikających z działania obciążeń zmiennych, cyklicznych, jakie występują w mostach. Problem analizowano, korzystając z klasycznego parametru, który charakteryzuje podatność zespolenia C_z , oraz uzupełniono własnymi wskaźnikami μ oraz β . Wskaźniki te pozwalają ocenić stopień zespolenia w odniesieniu do dźwigara złożonego (o zespoleniu pełnym). Analizowano dwa ujęcia rozwiązania zagadnienia współdziałania elementów dźwigara zespolonego: liniowe oparte na rozwiązaniu w postaci analitycznej (równania różniczkowe) oraz nieliniowe w ujęciu mechaniki luzów. Ujęcie to dobrze oddaje zasadę pracy dźwigara poddanego obciążeniom połączeń płyty betonowej z belkami stalowymi, występującymi w przęsłach mostowych. Analizę zilustrowano przykładami liczbowymi rzeczywistego mostu zespolonego. Główną uwagę zwrócono na zmiany kształtu wykresów zaproponowanych wskaźników μ i β .

An investigation of the grinding wheel wear with the use of root-mean-square value of acoustic emission

P. SUTOWSKI

Technical University of Koszalin, 75-620 Koszalin, Poland, e-mail: pawelsutowski@poczta.onet.pl

S. PLICHTA

Technical University of Koszalin, 75-620 Koszalin, Poland, e-mail: stanislawaplichta@poczta.onet.pl

This paper presents the results of an investigation of the grinding wheel wear in a peripheral surface grinding process. During this investigation varying geometrical parameters of an active grinding wheel surface have been measured and the components of the grinding force and acoustic emission signal have been recorded. On the basis of these output quantities an analysis has been conducted of an acoustic emission descriptor's practicability, i.e. a root-mean-square (RMS) value, to characterize the cutting abilities of a grinding wheel in the time progress of its work. This article also presents a new energy coefficient, which determines the rate of grinding wheel wear in the form of a RMS value of acoustic emission signal falling on a contact surface of a grinding wheel. Moreover, the article presents some examples of a correlation between the root-mean-square value of acoustic emission signal and the surface roughness of a workpiece, which shows that the parameters of acoustic emission signal can be a useful tool to monitor the surface roughness during the grinding process.

Keywords: grinding process, grinding wheel wear, tool life, acoustic emission, root-mean-square

1. Introduction

The results of an abrasive machining process, which ensures the expected quality of the workpiece, depend on three elements: the kind of stock (material), grinding conditions and the geometrical state of the active flank of the grinding wheel (AFGW). On the assumption that in the manufacturing cycle only one material is being processed and that the parameters are constant, the only variable in the whole process is the geometry of grinding wheel surface, which is determined by the wear and glazing of the grinding wheel in the function of time.

Among the methods allowing wear evaluation, there are direct and indirect methods which describe the changes on the wheel surface in the grinding process. In industrial applications, where a great capacity and efficiency of manufacturing processes are required, the most widely applied are non-destructive methods, which additionally do not need to hold up the machining. That group includes indirect methods, which are based on an observation and analysis of effects which accompany the grinding process and which are greatly dependent on the properties of the grinding wheel tested.

Recently, an acoustic emission (AE) has been the method most commonly applied, but still in the phase of research. We are hopeful that this method will be useful for monitoring the adaptation grinding machining methods. Of the methods applied so far, this is the one which gives the most essential information about the phenomena occurring in the grinding zone. An AE contains in a global manner the phenomena occurring both in the tool and the workpiece. Especially, an AE signal provides information about the size and nature of deformations being the result of machining conditions and the grinding wheel wear.

The main purpose of this paper is to evaluate the grinding wheel wear and to determine the tool life based on the changes of geometric parameters, which describe the state of AFGW, and the output quantities of the grinding process: F_c (tangent force), F_n (normal force) and U_{RMS} (root-mean-square value).

2. Research methods

Experiments were carried out with a universal surface grinder OC3, model 3711. An aloxite grinding wheel designated by producer as T1 250×32×98 99A60J7V was used. The grinding process took place at a constant flow rate of cooling-lubrication fluid $Q_c = 3$ [dm³/min]. The samples were made from tool steel (NC10 60±2HRC) and machined at the following parameters:

- grinding wheel peripheral speed $v_s = 27.5$ [m/sec];
- tangential table feed speed $v_{ft} = \{4; 14; 24\}$ [m/min];
- axial table feed $f_a = 0.3$ [mm/stroke];
- working engagement $a_e = 0.03$ [mm].

The grinding wheel was dressed with the use of M1010 single point dresser with a 1.23 carat diamond tip and a vertical angle of 93–110° under constant conditions in 3 passes:

- grinding wheel peripheral speed $v_s = 18$ [m/sec];
- axial dresser feed speed $v_{fd} = 230$ [mm/min];
- dresser engagement $a_d = 0.05$ [mm].

Output parameters of the process were recorded with the use of the Kistler equipment. Grinding forces were measured with a 9251A dynamometer, and the acoustic emission signal, with a 8152A2 sensor. Signals 1 or 2 seconds long of the frequency of 25 kHz per channel were recorded in files for statistical data handling.

The surface roughness of workpieces was described by an arithmetic mean roughness value (R_a) of a profile with the use of a ME 10 surface analyzer.

The measurement of the edge wear of the grinding wheel was carried out by means of an axial profile mapping on a razor blade, which was placed along the grinding wheel axis and fixed in a holder on the magnetic chuck of the grinding machine. The edge wear of the grinding wheel was determined by means of the active grinding wheel length (B_{kr}), with the use of Measuring Processor MZ-3541 (a distance measuring computer system).

3. Analysis of results

The most synthetic measure allowing the grinding wheel cutting abilities to be evaluated is the ratio of cutting abilities of an active grinding wheel surface (K_{AFGW}) related to the geometric features of AFGW. In the numerator of the expression representing K_{AFGW} , there are the values directly related to the area of the machined layer cut, and in the denominator, the values connected with the characteristics of the AFGW wear:

$$K_{AFGW} = \frac{w_i \cdot a_{zsr} \cdot l_w}{l_s \cdot B_{kr}}, \quad (1)$$

where:

l_s – mean abraded length of abrasive grain vertex profile,

w_i – mean amount of abrasive grain vertices,

l_w – mean distance between abrasive grain vertices,

a_{zsr} – elementary cutting depth per one abrasive grain (i.e., an abrasive grain load in the grinding zone).

The changes of this ratio, determined on the basis of measurements in the function of the grinding wheel working time, are presented in Figure 1.

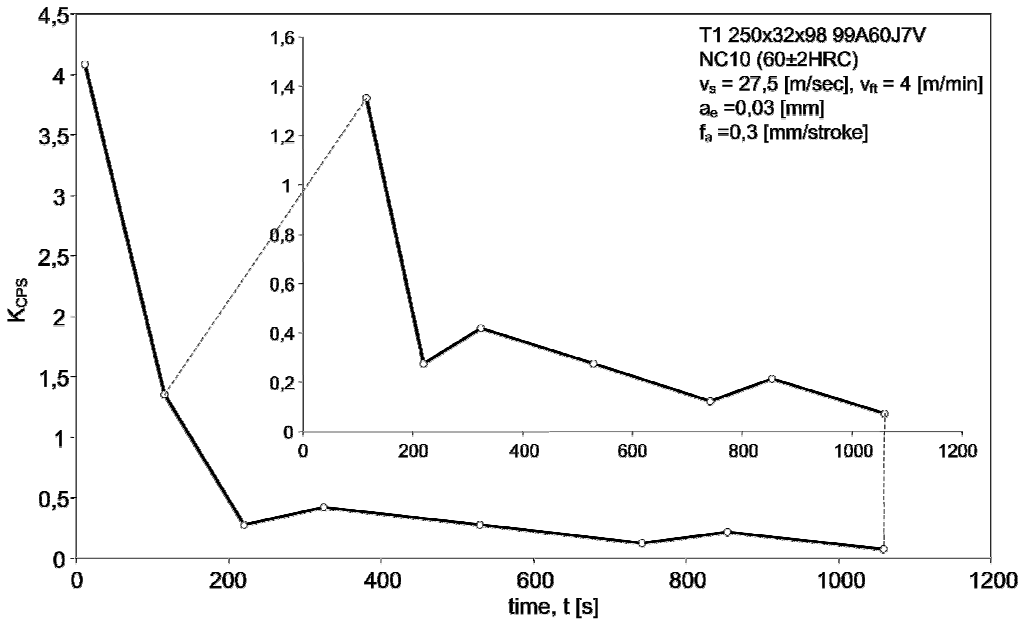


Fig. 1. The changes of the ratio of cutting abilities (K_{AFGW}) depending on the working time of the grinding wheel

Under given machining conditions, K_{AFGW} ratio represents a visible loss of cutting abilities of the grinding wheel after 1058 [sec] (about 17 [min]) of working time.

The analysis of the relationship between geometric parameters of AFGW, included in K_{AFGW} ratio, and the output quantities of the process in each case showed that the acoustic emission was characterized by a better correlation coefficient than any force component.

Figure 2 depicts the relationships between the output quantities (F_c , F_n , U_{RMS}) and the active grinding wheel length (B_{kr}) for one example of machining parameters.

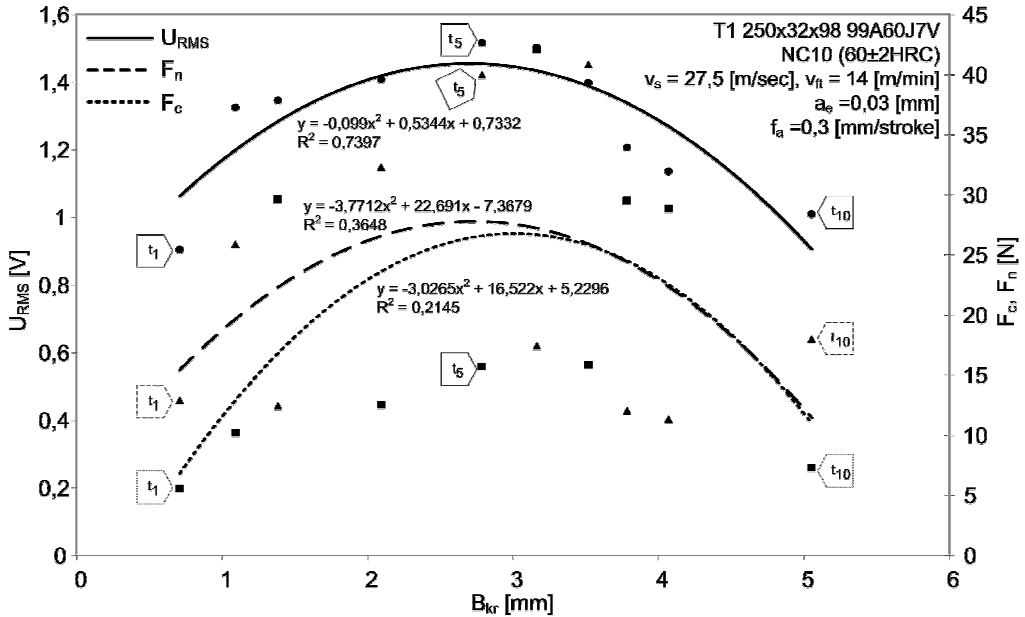


Fig. 2. The changes of the output process signals (F_c , F_n and U_{RMS}) depending on the active grinding wheel length (B_{kr})

In this case, the function $U_{RMS} = f(B_{kr})$, expressed in the form of quadratic polynomial below, has been distinguished from two other by the highest correlation coefficient: $R^2 = 0.74$ (the correlation coefficient has been determined in MS Excel program and presents the concentration ratio of the experimental data to the assigned curve):

$$U_{RMS} = -0.099 \cdot (B_{kr})^2 + 0.5344 \cdot (B_{kr}) + 0.7332. \quad (2)$$

The correlation between the components of the grinding force (F_c , F_n) and the changes of the analyzed geometrical parameters of an active grinding wheel surface is low.

Similar results have been obtained for the remaining parameters, which describe the geometry of the active grinding wheel surface, and are given in K_{AFGW} ratio. But for an increase of tangential table feed speed (v_f), due to an escalation of the changes in the grinding zone, the correlations described become lower.

The relationships obtained between the tangential force (F_c), normal force (F_n), root-mean-square value (U_{RMS}) and the ratio of the cutting abilities of active grinding wheel surface (K_{AFGW}) are presented in Figure 3.

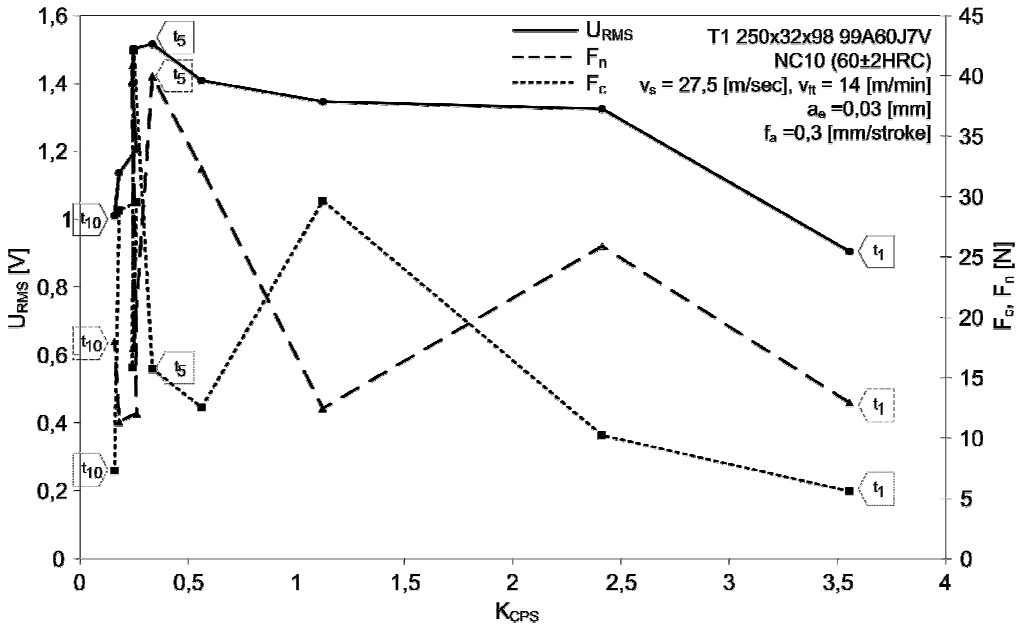


Fig. 3. The relationships between the output process values (F_c , F_n , U_{RMS}) and the ratio of the cutting abilities of active grinding wheel surface (K_{AFGW})

Along with the time of the grinding wheel work, its cutting ability diminishes to a certain value of the coefficient K_{AFGW} ($K_{AFGW} = 0.3355$; $t_5 = 190.97$ [sec]). In the period of the grinding wheel work (in the example analyzed), both components of the grinding force and the RMS increase. This increase in the values of the components of the grinding force and RMS was caused by an increasing quantity of grains in the grinding zone (as a result of B_{kr} increase – the contact length).

After the boundary value of the coefficient K_{AFGW} has been exceeded, the values of U_{RMS} , F_n and F_c signals are reduced considerably, since in this period of grinding wheel work ($t > t_5 = 190.97$ [sec]), the grain vertices begin to show an abrasive wear of the larger part, and the elementary cutting depth for one abrasive grain (a_{zsr}) becomes shallower. For this reason, the coefficient K_{AFGW} has a small value and changes in a very narrow range (0.3355–0.1611) with a tendency to decrease.

The consequence of this is a significant decrease in the AE signal and in the values of the grinding force components. The changes of the AFGW geometry, caused by its wear, have a direct influence on the size of the mechanical and thermal loads of workpieces in the grinding zone.

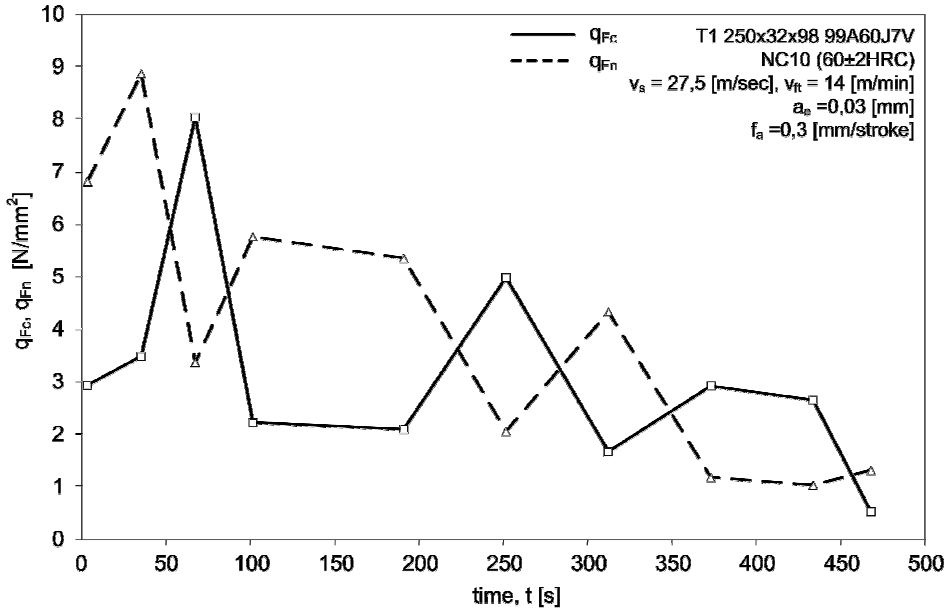


Fig. 4. The changes of grinding force components for the elementary surface in the grinding zone, depending on the working time of the grinding wheel

The loss of the cutting ability of the grinding wheel in the case analyzed occurred as a consequence of a considerable reduction of the elementary cutting depth for one abrasive grain in the grinding zone, due to the width enlargement of the contact zone (B_{kr}) and an increase in the quantity of active grains. The relationships between the values of the components of the grinding force per an elementary surface of the grinding zone (Figure 4) have a visibly diminishing tendency. These quantities are given below as the coefficients of an elementary loading of the grinding zone with the contiguous and normal grinding force.

Besides, a new energetic coefficient has been proposed. It describes the cutting ability of the grinding wheel by the root-mean-square value of the acoustic emission signal (U_{RMS}) per an elementary surface of the grinding wheel contact with the workpiece ($B_{kr} \cdot L_{\psi}$):

$$q_{Fc} = \frac{F_c}{B_{kr} \cdot L_{\psi}}, \quad (3)$$

$$q_{Fn} = \frac{F_n}{B_{kr} \cdot L_{\psi}}, \quad (4)$$

$$q_{RMS} = \frac{U_{RMS}}{B_{kr} \cdot L_{\psi}}, \quad (5)$$

$$L_{\psi} = \sqrt{d_s \cdot a_e}, \quad (6)$$

where:

L_{ψ} – the length of grinding zone contact with workpiece,

d_s – the external diameter of grinding wheel,

a_e – working engagement of grinding wheel.

The nature of the changes of the coefficient q_{RMS} in the function of working time of the grinding wheel in the case selected is presented in Figure 5.

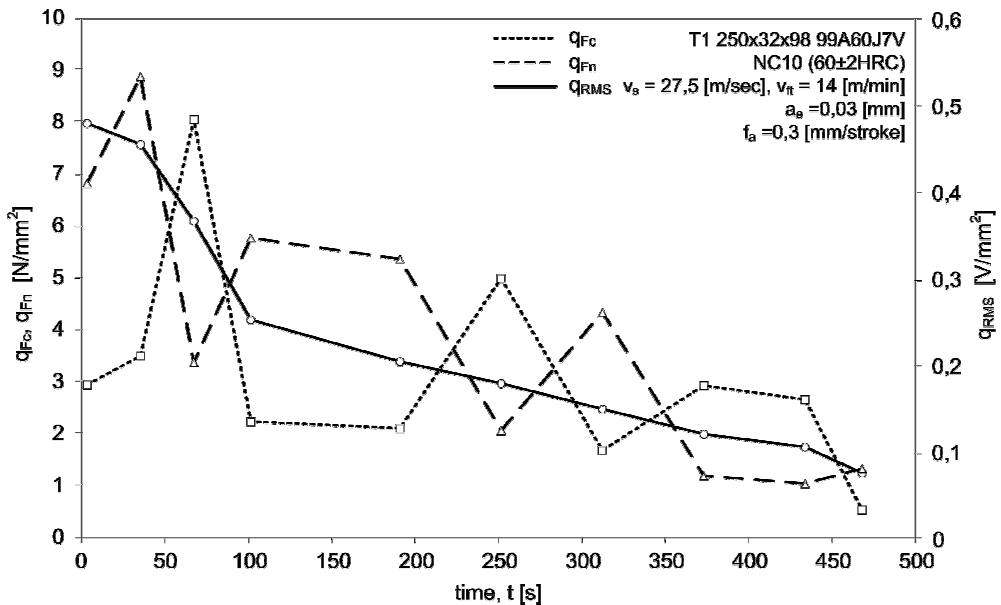


Fig. 5. Changes of q_{RMS} values depending on the grinding wheel working time

The lowest values of the coefficients q_{Fc} and q_{RMS} were measured after the time t of the grinding wheel work equal to 468 [sec] (ca. 8 [min]). In this case, the working conditions of the abrasive grain in the grinding zone were not suitable for initiating a self-sharpening process and for appearing new microvertices on active grinding wheel surface.

There was only an abrasive wear of grain vertices, and the final effect of this was grinding burn on the machined surface and the changes in the surface microhardness. The grinding wheel lost its cutting ability.

Based on the above, the changes of q_{Fc} and q_{RMS} coefficient allow the cutting ability of the grinding wheel to be unambiguously determined; besides, they can be more useful parameters than other parameters. These coefficients can be used as the criterion of the grinding wheel durability.

The correlations between the changes of q_{Fn} , q_{Fc} and q_{RMS} coefficients and the ratio of cutting ability of active grinding wheel surface (K_{AFGW}) are presented in Figure 6.

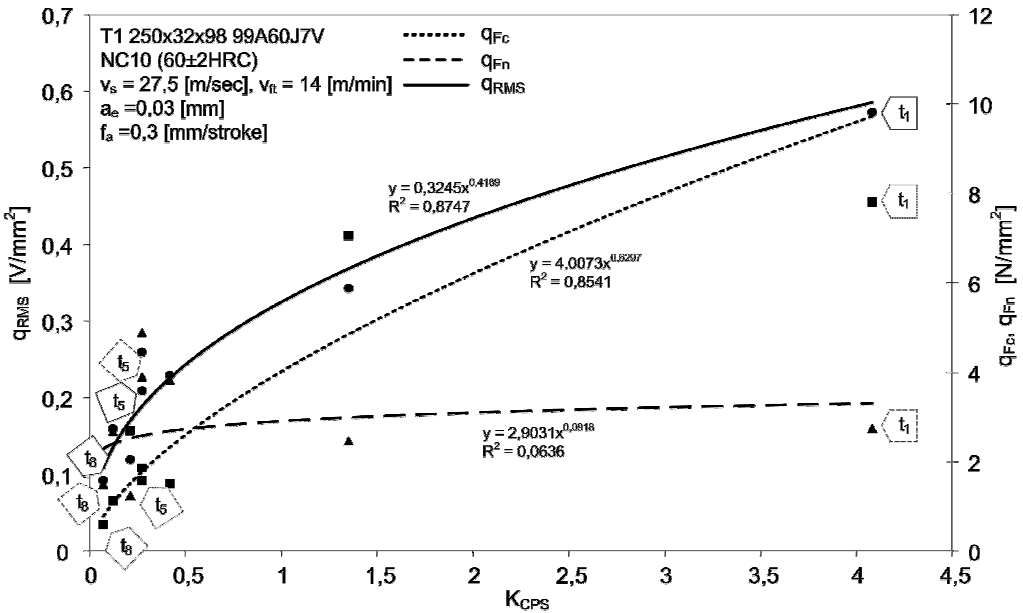


Fig. 6. The correlations between the changes of q_{Fn} , q_{Fc} and q_{RMS} coefficients and the ratio of the cutting ability of active grinding wheel surface (K_{AFGW})

Under conditions of our investigations the dependence q_{RMS} had the highest correlation ($R^2 = 0.8747$). It was approximated by the following function:

$$q_{RMS} = 0.3245 \cdot (K_{AFGW})^{0.4189}. \quad (7)$$

Based on the wear evaluation, as Kannatey-Asibu and Domfeld [2] proposed, in the present investigations the parameters of beta distribution were used to analyze the root-mean-square values of acoustic emission, on the assumption that this signal shows a beta distribution.

$$r = \frac{\bar{U}_{\text{RMS}}}{W_{\text{RMS}}} (\bar{U}_{\text{RMS}} - (\bar{U}_{\text{RMS}})^2 - W_{\text{RMS}}), \quad (8)$$

$$s = \frac{1 - \bar{U}_{\text{RMS}}}{W_{\text{RMS}}} (\bar{U}_{\text{RMS}} - (\bar{U}_{\text{RMS}})^2 - W_{\text{RMS}}), \quad (9)$$

$$\text{kurtosis} = 6 \cdot \frac{(r-s)^2 \cdot (r+s+1) - r \cdot s \cdot (r+s+2)}{r \cdot s \cdot (r+s+2) \cdot (r+s+3)}, \quad (10)$$

where:

W_{RMS} is a variance of the signal U_{RMS} ,

r, s are the beta-distribution parameters.

The kurtosis is a normalized fourth-order centre moment, which appears to be a useful measure.

It became evident that the changes of kurtosis for the RMS value of acoustic emission (U_{RMS}) are dependent on the grinding wheel wear, and this relation increases together with wear stages (Figure 7).

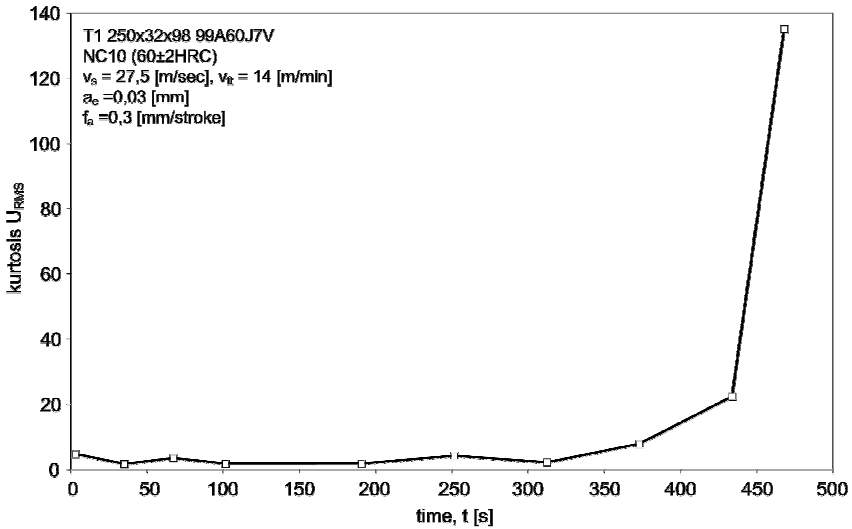


Fig. 7. Loss of the cutting abilities expressed by the kurtosis of U_{RMS}

The nature of the kurtosis changes of the signal U_{RMS} shows an abrupt increase of its value when the process is stopped because of the grinding burns appearing on the machined surface. This testifies to substantial changes in the CPS geometry, a loss of its cutting ability and a considerable thermal influence of the grinding wheel on the machined surface, which results in grinding burns.

So, the kurtosis parameter can play a major role in revealing the changes in the process producing the surface (e.g., tool wear).

The changes in the AFGW geometry, caused by its waste, have a decisive effect upon the results of the grinding process estimated in this article based on the measurements of the roughness of the grinding surface (R_a).

The reduction of an average height of abrasive grain vertices, the appearance of microvertices on grains and the reduction of an average elementary cutting depth for one abrasive grain (a_{zsr}), and indirectly the smaller cutting abilities of the grinding wheel, are due to a decrease in the grinding surface roughness.

The changes in the surface roughness of grinding workpiece in the function of grinding force components and in the function of root-mean-square are presented in Figure 8.

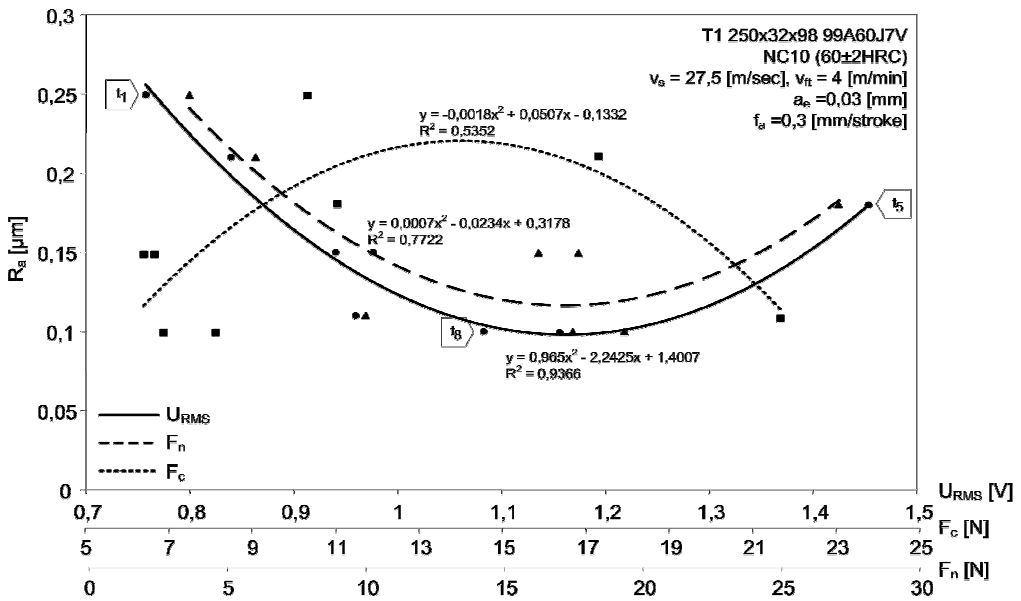


Fig. 8. The correlation between the roughness of the machined surface (R_a) and the registered output quantities (F_c , F_n , U_{RMS})

The highest correlation, under the working conditions studied, was for $R_a = f(U_{RMS})$ expressed by the function with the correlation coefficient $R^2 = 0.9366$:

$$R_a = 0.965 \cdot (U_{RMS})^2 - 2.2425 \cdot (U_{RMS}) + 1.4007. \quad (11)$$

Together with the tangential table feed speed increase (v_{ft}), the correlation coefficient of function $R_a = f(U_{RMS})$ became smaller, which was the result of more significant dynamic changes in the grinding zone along with a load increase of grinding grains.

4. Summary

The investigations into the changes of geometrical parameters of the active grinding wheel surface (AFGW) and the output quantities of the grinding process (F_c , F_n and U_{RMS}) show clearly that due to the complexity of the grinding wheel wear process, in evaluation of the grinding wheel durability, the most useful are geometrical parameters of AFGW defined by the coefficient of cutting ability (K_{AFGW}) and energetic quantities defined by the coefficients q_{RMS} , q_{Fc} representing an elementary load of the grinding zone.

The best correlation shows the RMS value of the acoustic emission, which is the measure of the energy emitted by the material as a result of deformations occurring in it. Apart from this, the signal received from the whole machined material volume captures the total influence of the results of the wear of abrasive grains and AFGW, which have a direct influence upon the size of deformations in the workpiece.

That is why the coefficient q_{RMS} shows a very high correlation with the ratio of the cutting abilities of active grinding wheel surface (K_{AFGW}) related to geometric results of AFGW wear and a kinematic nature of grain working conditions.

Therefore, the root-mean-square of the acoustic emission may be sufficient to evaluate the cutting ability of the grinding wheel without measurements of geometrical changes of the AFGW and without breaks in the process. The results of the investigations show that the kurtosis of U_{RMS} allows us to evaluate the wear progress, or to notice the destructive wear, or to detect grinding burns on the machined surface.

References

- [1] Adamczyk E., Ranachowski Z.: *Pomiary emisji akustycznej*, [w:] Malecki I., Ranachowski J.: *Emisja akustyczna – źródła, metody, zastosowania*, Komitet Badań Naukowych, Warszawa, 1994, str. 457–466.
- [2] Kannety-Asibu E., Dornfeld D.A.: *A study of tool wear using statistical analysis of metal-cutting acoustic emission*, *Wear*, 1982, Vol. 76, No. 2, pp. 247–261.
- [3] Koziański A., Gołąbczak A., Urbaniak M.: *Metoda oceny roboczej powierzchni ściernicy*, Materiały V Międzynarodowej Konferencji *Postępy w teorii i technice obróbki materiałów*, Kraków, 1978, str. 177–184.
- [4] Oczóś K., Porzycki J.: *Szlifowanie. Podstawy i technika*, Wydawnictwo Naukowo-Techniczne, Warszawa, 1986.
- [5] Plichta J.: *Próba kompleksowej oceny zmian stanu roboczej powierzchni ściernicy podczas szlifowania*, *Zeszyty Naukowe Wydziału Mechanicznego nr 12, WSInż. w Koszalinie*, Koszalin, 1988, str. 245–252.
- [6] Plichta S.: *Wpływ geometrycznych skutków zużycia ściernicy na naprężenia własne w warstwie wierzchniej szlifowanego przedmiotu*, XI Naukowa Szkoła Obróbki Ściernej, Łódź, 1988, str. 117–124.
- [7] Plichta S.: *Możliwości wykorzystania emisji akustycznej w badaniach właściwości skrawnych ziaren ściernych*, *Postępy Technologii Maszyn i Urządzeń*, 1999, t. 23, nr 1, str. 97–111.

- [8] Plichta S., Plichta J.: *Prognozowanie naprężeń w warstwie wierzchniej szlifowanego przedmiotu na podstawie czynnego pomiaru stanu roboczej powierzchni ściernicy*, Ogólnopolska VI Konferencja *Tendencje rozwojowe w technologii maszyn*, WSI, Zielona Góra, 1990, Sekcja I Obróbka Skrawaniem, str. 141–147.
- [9] Plichta S.: *Ocena procesu szlifowania z wykorzystaniem metod pomiaru emisji akustycznej*. XXV Naukowa Szkoła Obróbki Ściernej, Wrocław–Duszniki Zdrój, 11–14 wrzesień 2002, str. 279–285.
- [10] Plichta S., Drzycimski M.: *Możliwości monitorowania procesu szlifowania z wykorzystaniem sygnału emisji akustycznej*, XXII Naukowa Szkoła Obróbki Ściernej, Gdańsk–Jurata, 8–10 wrzesień 1999, str. 223–238.

Badanie zużycia ściernicy z wykorzystaniem wartości skutecznej sygnału emisji akustycznej

Prezentowano wyniki badań nad zużyciem ściernicy elektrokorundowej w procesie obwodowego szlifowania płaszczyzn. Mierzono zmieniające się parametry geometryczne czynnej powierzchni ściernicy (CPS), rejestrowano wartości składowych siły szlifowania oraz sygnał emisji akustycznej. Na podstawie tych wielkości wyjściowych procesu przeanalizowano przydatność deskryptora emisji akustycznej (EA), jakim jest wartość skuteczna (RMS), w scharakteryzowaniu zdolności skrawnych ściernicy w miarę czasu jej pracy. Zaprezentowano także nowy współczynnik energetyczny, określający stopień zużycia ściernicy, w postaci wartości skutecznej sygnału emisji akustycznej przypadającej na powierzchnię kontaktu ściernicy. Ponadto przedstawiono przykłady korelacji wartości skutecznej sygnału emisji akustycznej z chropowatością powierzchni szlifowanego przedmiotu, które wskazują na możliwość wykorzystania sygnału EA i jej wartości skutecznej (RMS) do monitorowania chropowatości powierzchni szlifowanej.

Information for Authors

Send to: *Archives of Civil and Mechanical Engineering*
Polish Academy of Sciences, Wrocław Branch
Podwale 75, 50-449 Wrocław, Poland

Archives of Civil and Mechanical Engineering (ACME) publishes both theoretical and experimental papers which explore or exploit new ideas and techniques in the following areas: structural engineering (structures, machines and mechanical systems), mechanics of materials (elasticity, plasticity, rheology, fatigue, fracture mechanics), materials science (metals, composites, ceramics, plastics, wood, concrete, etc., their structures and properties, methods of evaluation), manufacturing engineering (process design, simulation, diagnostics, maintenance, durability, reliability). In addition to research papers, the Editorial Board welcome: state-of-the-art reviews of specialized topics, letters to the Editor for quick publication, brief work-in-progress reports, brief accounts of completed doctoral thesis (one page is maximum), and bibliographical note on habilitation theses (maximum 250 words). All papers are subject to a referee procedure, except for letters, work-in-progress reports and doctoral and habilitation theses, which are briefly reviewed by the Editorial Board.

The papers submitted have to be unpublished works and should not be considered for publication elsewhere.

The Editorial Board would be grateful for all comments on the idea of the journal.

Submit three copies, each complete with abstract, tables, and figures.

Detailed information about the Journal on web:

<http://www.pan.wroc.pl>

www.ib.pwr.wroc.pl/wydzial/czasopismoACME.html

<http://www.wmech.pwr.wroc.pl>

Price 15 zł
(0% VAT)

Subscription orders should be addressed to:
Oficina Wydawnicza Politechniki Wrocławskiej
Wybrzeże Wyspiańskiego 27
50-370 Wrocław